Universita' degli studi di Parma

Science and Technology of Innovative Materials

Advanced analytical transmission electron microscopy methodologies for the study of the chemical and physical properties of semiconducting nanostructures

Enzo Rotunno

Supervisor:
Dr. Laura Lazzarini

Tutor:
Dr. Giancarlo Salviati

Dottorato di ricerca XXVI ciclo

Marzo 2014

Summary

Chapter 1: PREFACE

The name nanostructure refers to every structure with at least one dimension in the range of 1-100nm. In the recent years they have attracted steadily growing interest due to their peculiar, fascinating properties as well as their unique applications complementary to the bulk materials.

As an example, semiconductor nanostructures exhibit novel electronic and optical properties owing to their dimensionality and possible quantum confinement effects. Thanks to the broad selection of compositions and band structures, nanostructures are considered to be the critical components in a wide range of potential device applications.

The ability to generate such small structures is central to the advance of many areas in modern science and technology. There are a large number of opportunities that could be realized by simply making new types of nanostructures, or by down-sizing currently existing structures into the nanoscale regime.

Among them, 1D nanostructures (including wires, rods, belts, and tubes) provide a better model system for investigating the dependence of electronic transport, optical, and mechanical properties on size confinement and dimensionality. Nanowires (NWs), in particular, should play an important role as both interconnections and active components in fabricating nanoscale electronic and photonic devices. [1]

Scientists involved in the nanowire field are constantly trying to develop new fundamental science as well as potential applications. Several important subfields have emerged and each represents

an exciting research direction. These subfields include NW electronics, NW photonics, NWs for energy conversion and storage, and interfacing NWs with living cells.

The interest in the NWs field is still mounting [2] as can be seen from the vast number of papers (Figure 1) published over the past two decades, which has increased exponentially, with most of the activity and development happening in the last ten years.

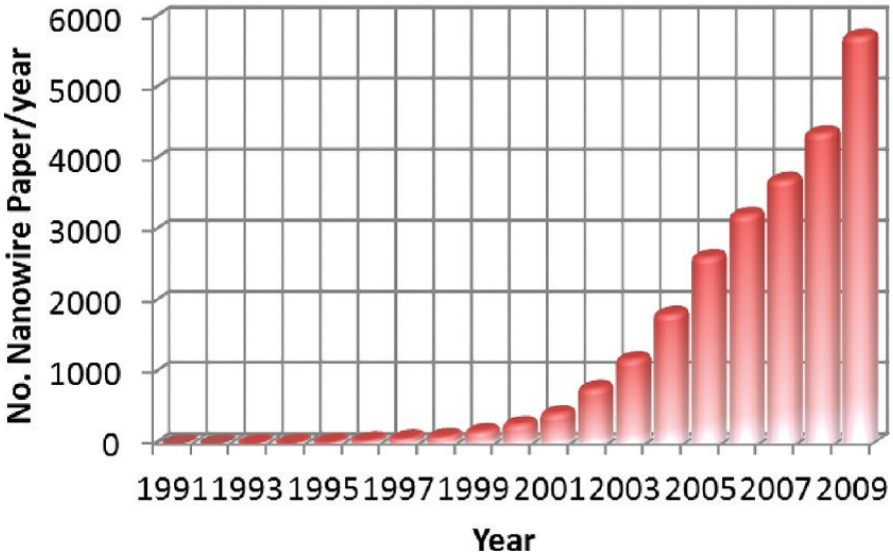

Figure 1: Increase in the number of publications on nanowire related topics from year 1991-2009

Current research has focused on rational synthetic control of one-dimensional nanoscale building blocks, novel properties characterization and device fabrication based on NW building blocks, and integration of NWs into complex functional architectures.

Therefore, the fundamental study of size, surface structure, and interface effects on material properties in semiconductor nanowires is of paramount importance for current nanotechnology applications in electronic, optoelectronic, thermoelectric, photonic, mechanical systems, and life science.

As nanotechnology and related areas monopolize both the scientific community's interest, the TEM is becoming the central tool for the complete characterization of nanoscale materials and devices, because no other scientific instrument exists which can offer such a broad range of characterization techniques with such high spatial and analytical resolution, coupled with a completely quantitative understanding of the various techniques.

TEM becomes an even more powerful tool when it is combined with image simulations that assist in interpreting experimental images and are an essential requirement for quantitative imaging.

This thesis deals with the employment and development of TEM methodologies useful in the study of semiconducting NWs. The first chapter of this dissertation aims to provide the physical and mathematical basis for the correct interpretation and analysis of the TEM micrographs. A substantial part of the first chapter is devoted to the algorithm currently used for the simulation of TEM images which are employed several times in these pages.

The TEM techniques are successfully employed in studying NWs of two different kinds of semiconducting materials and the results are exposed in the second part of this work: the chalcogenide (Ge)-Sb-Te NWs, in the main stable stoichiometries, are the main topic of chapter 4 while the structural analysis of a hexagonal polymorph of Si occupies chapter 5.

Chapter 2: TRANSMISSION ELECTRON MICROSCOPY

2.1 Introduction

In analogy with an optical microscope, an electron microscope exploits the interaction of a radiation with the sample. The radiation used in TEM is an electron beam suitably accelerated, which allows to obtain a very small wavelength and to largely exceed the resolution limit of conventional optical microscopes.

The elastically scattered electrons, together with the direct beam, are the signals used for the conventional TEM mode, namely imaging and electron diffraction techniques. Nowadays, thanks to the new generation of aberration corrected microscopes, electron diffraction and high resolution imaging are an indispensable part of TEM work and are one of the most useful aspect for the materials scientists and nanotechnologists who are mainly interested in knowing the crystal structure (and particularly crystal defects) of their samples.

The advantage of using an ionizing radiation, such as electrons, is the large number of secondary signals that it generates while interacting with the sample.

Some of these "*by-product*" signals are summarized in Figure 2. Many of these can be detected in different types of TEM, and are used in the different analytical TEM techniques, giving chemical information and a lot of other details about the specimens.

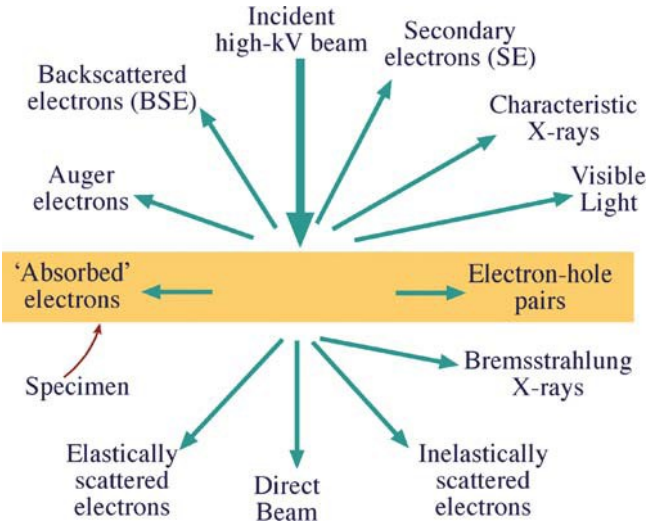

Figure 2: A summary of the interaction products of the primary beam with the sample. The direction of the arrows is not related to the scattering direction.

As an example, Energy Dispersive X-ray spectrometry, commonly abbreviated in EDX, uses the characteristic X-ray emitted by the relaxation of the atoms excited by the incident beam and allows chemical mapping also on the atomic level. EDX is very helpful to study devices, such as transistors, made out of several layers with different chemistry, where the interdiffusion between the layers can affect the properties of the device, or complex alloys that can suffer phase segregations.

Therefore, a TEM is fundamentally a signal-generating and detecting instrument rather than simply a microscope for high-resolution images and diffraction patterns, as it operated for many decades.

I will report in this chapter the basic principles of the TEM and of the main analytical microscopy techniques useful for the result interpretation. A complete and rigorous description can be found in many fundamental microscopy books. [3][4][5]

2.2 The microscope

As mentioned above, several techniques are usually referred to under the general name “TEM”, requiring many different tools to be attached to the microscope. As a result, many kinds of electron microscopes can be identified, mainly differing for the acceleration voltage and the analytical capabilities. Even if it is difficult to give a general description of the microscope, some basic components are the same in every microscope and are schematically illustrated in Figure 3.

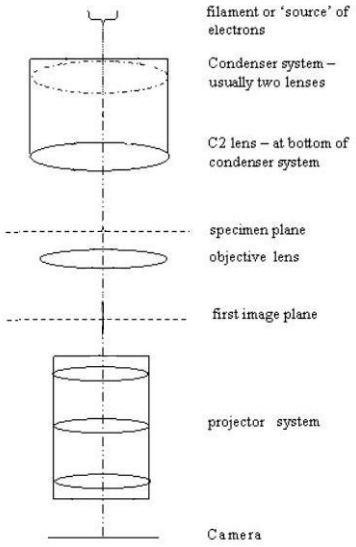

Figure 3: a simplified scheme of the lens system inside the microscope. The name of each lens or set of lenses is reported.

A stable, bright and coherent source of electrons, namely the electron gun, is always present in the microscope. Because the quality of the measurement is strongly dependent on the performances of the gun, it is one of the most important parts of a TEM.

These stringent requirements are best met by only two types of source: thermionic and field-emission guns.

In a typical thermionic source, a tungsten filament or a lanthanum hexaboride (LaB_6) crystal is heated to a sufficiently high temperature to give the electrons the energy they need to overcome the work function of the material and escape from the surface.

In a field emission gun (FEG) a fine tungsten needle (Figure 4a) is highly biased, typically 3-5 kV. The strength of the electric field is considerably increased thanks to the tip geometry effects and is able to extract electrons from the tip.

In order to efficiently extract electrons from a FEG, the tip has to be as clean as possible and also the smallest trace of oxide on it can hamper the extraction. For this reason FEGs can only work in ultra high vacuum condition ($<10^{-9}$ Pa) and so they are more expensive than thermionic guns.

Alternatively, the surface can be kept clean a poorer vacuum ($<10^{-6}$ Pa) by heating the tip. The thermal energy assists the electron emission by thermionic effect. In this case the tip is covered by a thin layer of ZrO_2 to improve the emission characteristics. This second kind of field emitters is named Schottky FEG to distinguish them from the "cold" FEG.

Despite the higher price, FEGs offer several advantages on the thermionic sources having higher brightness, coherence, stability and lifetime, and are used in almost every new generation microscope.

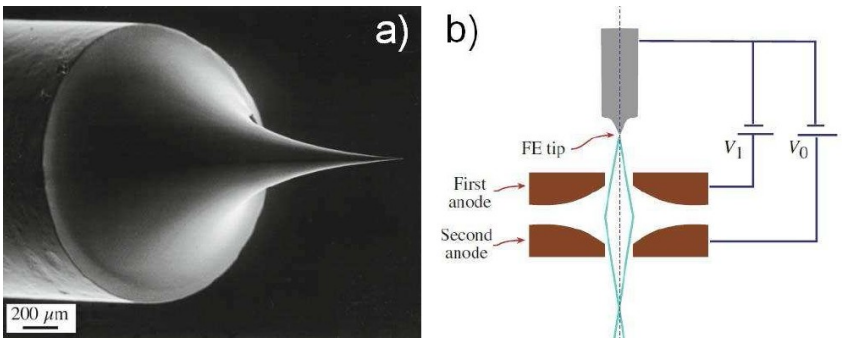

Figure 4: a) SEM image of a tip for the field effect source and **b)** a diagram of the electron gun.

A schematic of a typical FEG is reported in Figure 4b: after the electrons are extracted from the tip by the voltage V1 applied to the first anode they are accelerated to the working voltage by the second anode. The working voltage, depending on the microscope, may vary between 60 and 300 kV.

Due to the particle-wave dualism, the electron are characterized by the relativistic wavelength

$$\lambda = \frac{h}{\left[2meV\left(1+\frac{eV}{2mc^2}\right)\right]^{1/2}} \qquad (2.1)$$

Where *m* is the rest mass of the electrons, *e* is fundamental charge, V the acceleration voltage and *c* the speed of light.

The relativistic wavelength, according equation 2.1, for different common acceleration voltages is reported in Table 1.

80 kV	100 kV	200 kV	300 kV
0.0418 Å	0.0370 Å	0.0251 Å	0.0197 Å

Table 1: relativistic wavelength for different common acceleration voltages.

Independently from the particular source, after the electron has been emitted, they pass through a set of magnetic lenses called condenser lenses.

The condenser lenses have the task to tailor the illumination on the sample: they select the area of illumination and adjust the brightness.

In the conventional TEM mode, the condenser system realizes a parallel electron beam along the optic axis of the column. The parallel illumination is essential to get the sharpest diffraction patterns as well as the best image contrast.

The condenser system can also be adjusted in order to illuminate a very small area with a highly convergent beam. In this case, the beam acts as an electron probe that can be rastered on the sample. The working mode using this illumination is called Scanning Transmission Electron Microscopy (STEM) and will be discussed later in this chapter.

The specimen is placed in a sample holder right below the condenser system. The holder can usually be tilted along two directions orthogonal to each other belonging to the plane perpendicular to the column axis. After the sample, a system of electromagnetic lenses (objective, intermediate and projector) act to produce an image or the diffraction pattern (DP), from the electrons transmitted and diffracted by the sample. The electrons path, drawn as rays, after the specimen and the two basic operations (DP and imaging) of the microscope can be schematically represented as in Figure 5.

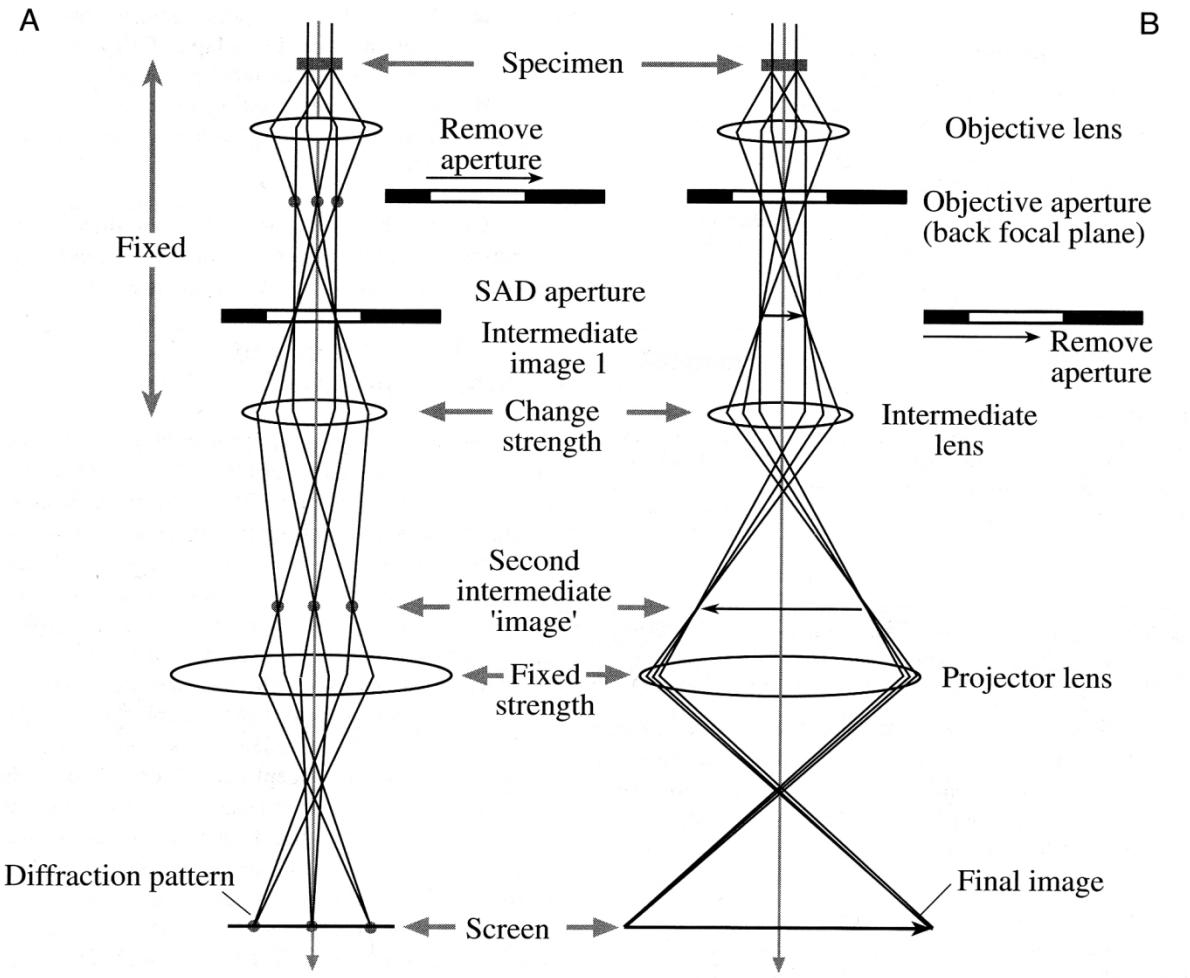

Figure 5: diagram illustrating the two main working mode of the TEM imaging system, **a)** formation of the diffraction pattern and **b)** formation of the sample image.

The objective lens takes the electrons emerging from the exit surface of the specimen, disperses them to create a diffraction pattern in the back focal plane, and recombines them to form an image in the image plane. In the back focal plane, the rays parallel to each other coming out from different sample regions are brought to a focus converging in a given point. In this way, any given direction of rays, corresponding to a specific diffraction, locates a specific point, so that the resulting characteristic pattern of active points is exactly the DP. The DP can be imaged by adjusting the imaging system lenses so that the back focal plane of the objective lens acts as the object plane for the intermediate lens (Figure 5a). Vice versa, to see the sample image the intermediate lens must be adjusted so that its object plane is the image plane of the objective lens (Figure 5b). The so called selected-area-diffraction (SAD) aperture can be inserted into the image plane of the objective lens in order to exclude the contribution to the DP of all the electrons that hit the sample outside the area defined by the aperture itself. An aperture inserted in the back

focal plane of the objective lens, called the objective aperture, selects the DP beams contributing to the image formation, producing bright field or dark field images if the direct beam or any scattered beam is selected respectively. The projector lens takes whatever it is in its image plane and produces the final image on the detector plane.

In order to have high magnification, it is essential to keep the objective lens focal length as short as possible and this means a very strong lens is needed. This is traditionally accomplished by inserting the specimen directly inside the lens, close to its center.

The objective lens is the most important lens in the whole microscope and its aberrations are the main factor limiting the microscope resolution.

2.3 Aberrations

The main limitation to the resolution of the microscope is due to the defects of the lenses. In particular, the aberrations of the objective lens are the most important. The three main aberrations are: the spherical and chromatic aberrations, and the astigmatism.

2.3.1 Spherical aberration

The spherical aberration is crucial because it is the only one that can not be simply corrected in conventional microscope but only through sophisticated (and expensive) aberration correctors, composed by a set of multipoles mounted inside the column, which produce magnetic fields able to correct the aberrations. This defect occurs when the field of the lens acts differently on the rays passing next to the optical axis and on the most peripheral ones, as illustrated in Figure 6.

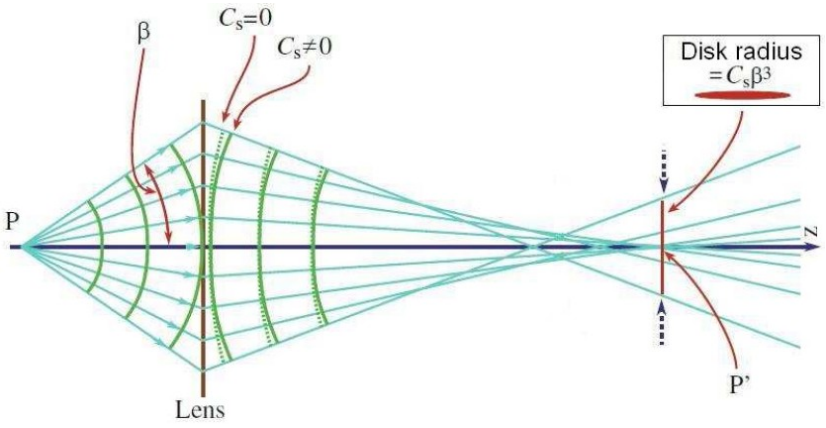

Figure 6: effect of the spherical aberration of the objective lens on the incident wavefront.

Off-axis and on-axis rays are focused in different points of the optical axis. This causes any point object P to be displayed in the image plane (point P') as a disk, called disk of confusion, with a radius $r \propto C_s \beta_3$ where β is the angular aperture of the lens and C_s is the spherical aberration coefficient.

C_s is a constructive parameter of the lens, it has the dimensions of a length and typically ranges between 0.5 and 3 mm and it cannot be changed. On the other hand, β has a lower limit fixed by the Rayleigh criterion: diffraction effects, resulting from the finite size of the lens, further blur the point object in an Airy disk of radius 0.61 λ/β.

Combining the two effects, an optimal value of $\beta_{opt} \propto \left(\lambda / C_S\right)^{1/4}$ is found as the optimum compromise between spherical aberration and diffraction limit. This value sets the radius of the disk of confusion, and so the achievable resolution, to

$$r_{sph} \propto C_S^{\,1/4} \lambda^{3/4} \tag{2.2}$$

2.3.2 Chromatic aberration

The chromatic aberration is due to the variation of the focal distance as function of the wavelength λ, and therefore the energy, of the electrons passing through the lens as reported in Figure 7.

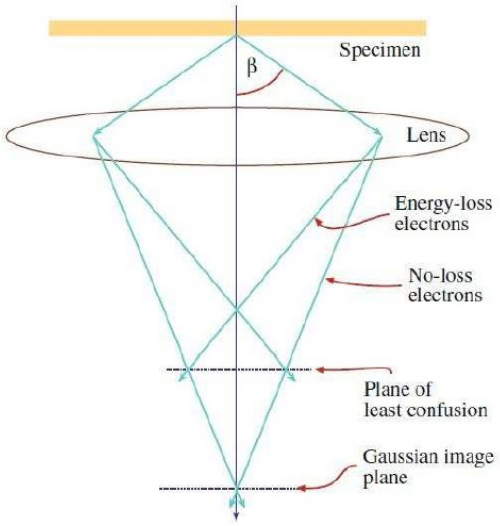

Figure 7: rays diagram showing the effect of the chromatic aberration on the image formation.

Although the incident beam is almost monochromatic, the electrons lose energy while interacting with the sample and the transmitted beam is characterized by an energy spread ΔE. The magnetic field action is stronger on the electrons with lower energy, focusing them at a shorter distance than those with higher energy. Again, the final effect on the image is to introduce a disk of confusion in the focal plane with radius

$$r_{chr} \propto C_C \frac{\Delta E}{E_0} \beta \tag{2.3}$$

where E_0, is the energy of the incident beam, β the angular aperture of the lens and C_C is the chromatic aberration coefficient.

The chromatic aberration can be easily corrected by means of an energy filter directly put in the column, acting as a monochromator, using for the image formation only the electrons which have not undergone any energy loss.

2.3.3 Astigmatism

The astigmatism is due to a non symmetric magnetic field, with respect to the axis of the lens, caused by the hysteresis of the lenses poles pieces and/or defects in their geometry.

In presence of astigmatism, rays that propagate in two perpendicular planes have different focal distance, as schematically shown in Figure 8.

The rays lying in the red plane are focused in the point T_1 while those that lie in the blue plane are focused in S_1: therefore a point object Q is displayed in the image plane as a disk of radius $r_a = \beta \Delta f_a$ with Δf_a equal to the maximum focal length difference due to astigmatism.

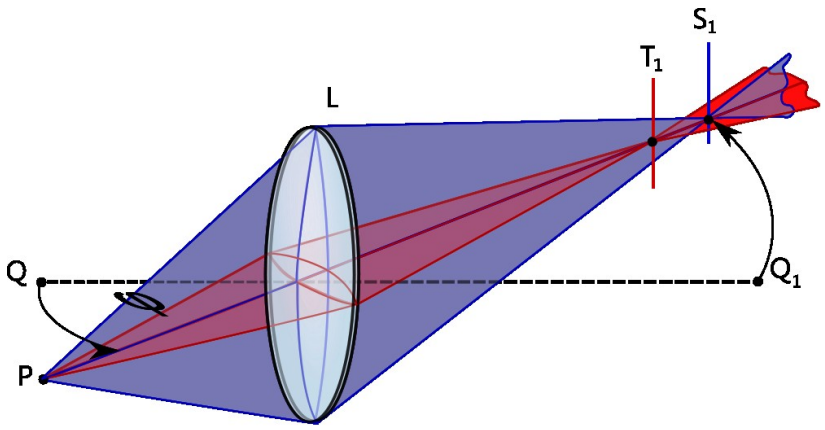

Figure 8: ray diagram showing the effect of the astigmatism on the image formation.

The lenses that are mainly affected by astigmatism are the condenser lenses, with a reduction of beam coherence, and the objective lens, with the worsening of the instrument resolution. The astigmatism can be corrected through proper stigmators [6], [7] to balance the inhomogeneities causing the astigmatism.

2.3.4 The aberration function

Spherical and chromatic aberration and astigmatism are the three major defects in electromagnetic lenses but there are many other aberrations to be taken into account. It is useful to introduce the aberration function $\chi(\vartheta, \varphi)$ [8], in order to quantitatively describe the aberrations. The aberration function is defined as the phase shift between the actual wavefront of the electron beam and an ideal spherical wavefront. Following the notation proposed by Krivanek [9] it can be written as:

$$\chi(\theta,\phi) = \sum_n \sum_m \frac{C_{n,m,a}\vartheta^{n+1}\cos(m\phi) + C_{n,m,b}\vartheta^{n+1}\sin(m\phi)}{n+1} \tag{2.4}$$

Where the angles ϑ and φ are the polar angular coordinates of a ray converging on the sample. The n index in the $C_{n,m}$ notation system refers to the order of the aberration: the wavefront distortion due to an aberration of nth order increases as the distance of an electron ray from the optic axis in the aperture plane to the $(n + 1)$th power and it displaces the corresponding ray in the image plane as the nth power of the distance. The m index refers to the angular multiplicity: the wavefront distortion due to an aberration of multiplicity m goes through m maxima (and m

minima) when the coordinate system is rotated through 360 degrees. The *a* and *b* indices account for the fact that azimuthally varying aberrations (all aberrations with $m > 0$) have two orthogonal components, rotated by $\pi/2m$ with respect to each other. The magnitude of each $C_{n,m,a}$ or $C_{n,m,b}$ aberration stands for the strength of the corresponding aberration coefficient.

The sum over *n* is taken from 0 to the highest order of aberrations of interest, and the sum over *m* is taken from 0 (or 1) to $n + 1$ for each order *n*, subject to the additional constraint that $m + n$ is odd.

According to this notation the defocus is described by the $C_{1,0}$ term while the astigmatism is the $C_{1,2}$ one. As an example, the wevefront distortions for the two components (x and y) of the astigmatism are reported in Figure 9.

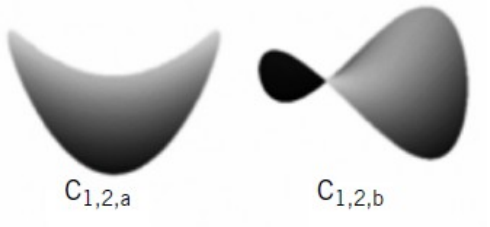

Figure 9: the wevefront distortion for the two components (x and y) of the astigmatism.

2.4 Theory of electron diffraction

The problem of the diffraction from a crystal lattice can be treated, from a classical point of view, within the wave optics framework.

If there is a large distance between the source and the sample and between the sample and the objective lens it is possible to consider all the wavefronts, involved in diffractive phenomena, as plane waves, in the context of the Fraunhofer diffraction. The wave function of the electrons is then fully described by the wave vector $\vec{k}$ and can be written as $\phi(\vec{r},\vec{k}) = Ae^{-i\vec{k}\cdot\vec{r}}$.

The discussion is further simplified by making the following assumptions:

1) The amplitude of the diffracted wave is negligible compared to the one of the incident wave that remains constant over the whole sample.
2) The interactions between the incident beam and the diffracted beam, and multiple diffractions are neglected.
3) Any absorption phenomenon is neglected.

In the frame of this approach, called kinematic theory of diffraction, the amplitude diffracted by two points objects, as those shown in Figure 10, is given by the sum $A_{TOT} = A + Ae^{i\varphi}$, where φ is the phase difference between the two waves which is directly proportional to the difference in the path travelled by the two beams: $\varphi = 2\pi(\vec{k}'-\vec{k})\cdot\vec{r}$.

The term $\vec{q} = \vec{k}'-\vec{k}$ is usually called scattering vector.

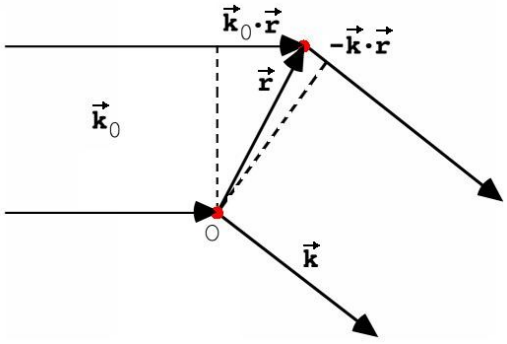

Figure 10: illustration of the scattering from two point objects.

The sum can be now generalized to a three-dimensional infinite lattice. The resulting amplitude of the scattered wave, in the direction given by $\vec{q}$, is

$$A(\vec{q}) = F_q \sum_n^N e^{2\pi i \vec{q}\cdot\vec{r}_n} \tag{2.5}$$

The index *n* runs over the unit cells in the crystal, $\vec{r}_n$ defines the position of n-th cell and F_q is the structure factor.

F_q contains all the information about the geometry of the unit cell and the scattering factors of the atoms composing the cell.

It is worth noting that eq. 2.5 actually is the Fourier Transform of the real lattice, being the sum, in the limit of $N \to \infty$, a Dirac delta function. The scattered amplitude $A(\vec{q})$ is different from 0 only for those values of the scattering vector such as the scalar product $\vec{q}\cdot\vec{r}_n$ is integer, i.e. when $\vec{q}$ coincides with one of the vectors of the reciprocal lattice $\vec{g}$.

The requirement $\vec{q} = \vec{k}' - \vec{k} = \vec{g}$ is called Laue condition and can be graphically represented with the geometrical construction known as Ewald Sphere according to the scheme shown in Figure 11.

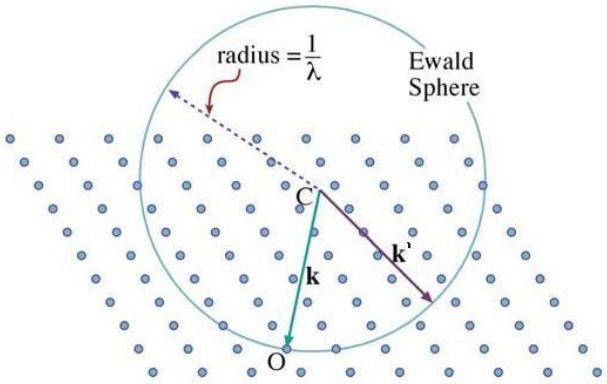

Figure 11: Ewald sphere construction.

Assuming all the scattering events to be elastic, the moduli of the incident and the scattered wave are the same: $|\vec{k}'| = |\vec{k}| = 1/\lambda$.

The center of the sphere is defined by the wave vector of the incident beam pointing a node of the reciprocal lattice chosen as origin O. The radius of the sphere is equal to the modulus of the

wavevector, $1/\lambda$. This way, every point of the reciprocal lattice $\vec{g}$, which is located on the surface of the Ewald sphere, satisfies the Laue conditions, provided its structure factor is different from zero.

Remembering the relationship between the reciprocal lattice and the atomic planes in the real lattice:

- The direction of reciprocal vector $\vec{g} = h\vec{u}_1 + k\vec{u}_2 + l\vec{u}_3$, being $\vec{u}_1$, $\vec{u}_2$ and $\vec{u}_3$ the basis set of the reciprocal lattice is normal to the family of atomic planes having Miller index hkl.
- The modulus of $\vec{g}$ is equal to the inverse of the spacing between the planes belonging to the family *hkl*: $|\vec{g}| = \frac{1}{d_{hkl}}$.

The familiar Bragg equation can be derived from the Laue condition following the simple geometrical consideration as in Figure 12:

$$2d_{hkl}\sin\theta = \lambda \tag{2.6}$$

in which the order of the reflection *n* has been incorporated in the interplanar distance: if *h, k, l* can be simultaneously divided by the factor n then the diffracted ray is the nth order reflection by the planes family having the real distance d_{hkl}/n.

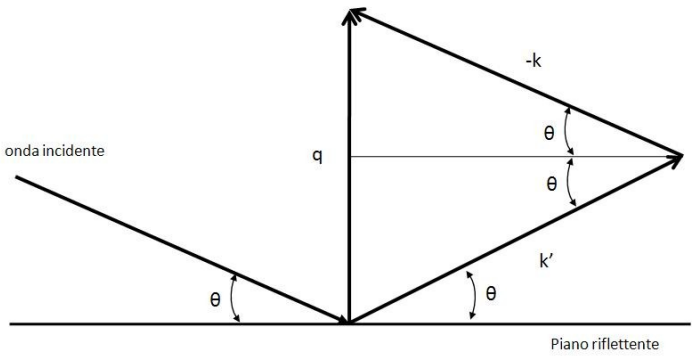

Figure 12: Bragg reflection from a set of crystalline planes.

The constraint imposed by the Laue condition is a strict requirement for a crystal of infinite size, to say, whose dimensions largely exceed the dimension of the unitary cell. This is not always the case for samples prepared for TEM analysis which need to be very thin (typically 5 to 200 nm) along the observation direction z in order to allow the electrons transparency.

For this reason, the Laue condition is valid only by two directions, x and y. Along z, the Laue condition becomes not so strict.

In fact, explicitly writing the three components x, y and z, the diffracted intensity in the $\vec{q}$ direction is:

$$I(\vec{q}) = |A(\vec{q})|^2 = F_q^2 \left(\frac{\sin^2 \pi N_x \vec{q} \cdot \vec{a}}{\sin^2 \pi \vec{q} \cdot \vec{a}} \right) \left(\frac{\sin^2 \pi N_y \vec{q} \cdot \vec{b}}{\sin^2 \pi \vec{q} \cdot \vec{b}} \right) \left(\frac{\sin^2 \pi N_z \vec{q} \cdot \vec{c}}{\sin^2 \pi \vec{q} \cdot \vec{c}} \right) \quad (2.7)$$

Where N_x, N_y, N_z are the numbers of unit cells in the three directions with $N_x N_y N_z = N$.

Equation 2.7 has been derived from equation 2.5 exploiting the mathematical relations: $\vec{r}_n = n_x \vec{a} + n_y \vec{b} + n_z \vec{c}$ with $\vec{a}$, $\vec{b}$ and $\vec{c}$ the basis set for the direct lattice and $\sum_n^N x^n = \frac{1-x^N}{1-x}$, the summation rule for the geometric series.

When $N \to \infty$, the function $\left(\frac{\sin^2 \pi N \vec{q} \cdot \vec{r}}{\sin^2 \pi \vec{q} \cdot \vec{r}} \right) \to \delta_{\vec{q}=\vec{g}}$, a delta function centered on the positions $\vec{q} = \vec{g}$ while, for finite values of N, the intensity is different from 0 even for $\vec{q} \neq \vec{g}$. The vector $\vec{s} = \vec{q} - \vec{g} = s_x \vec{u}_1 + s_y \vec{u}_2 + s_z \vec{u}_3$, representing the deviation from the Bragg law, is called excitation error.

For a crystal infinite in the direction x and y, with thickness $t = N_z |\vec{c}|$, the scattered intensity becomes:

$$I(\vec{q}) = F_q^2 \delta(s_x) \delta(s_y) \left(\frac{\sin^2 \pi t s_z}{\sin^2 \pi s_z} \right) \quad (2.8)$$

We can take into account this weakened condition directly into the Ewald Sphere construction by replacing the reciprocal lattice points with rods, elongated along the z direction, as shown in Figure 13. It is now obvious that the reflection condition is much more easily met and that several reflections can be visible at the same time.

According the values given in Table 1, the radius of the Ewald sphere is several tens of $Å^{-1}$ (e.g. 40 $Å^{-1}$ at 200 kV), while the typical distance between the rods in a semiconductor material is about 0.5 $Å^{-1}$.

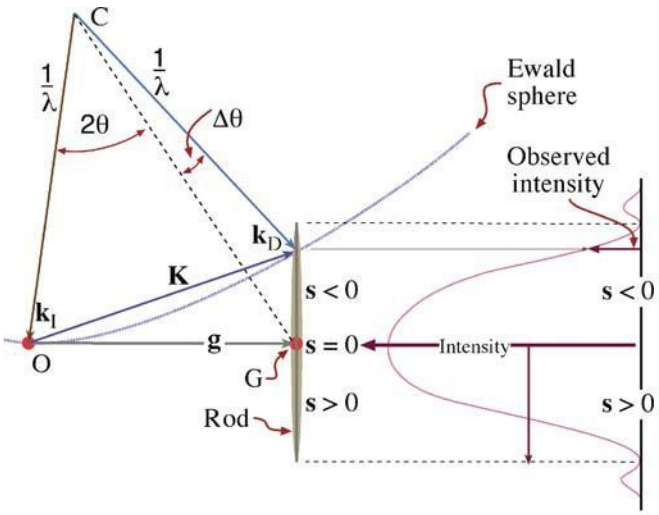

Figure 13: diagram showing the deviation from the Bragg law. The scattered intensity is reported on the right side as a function of the excitation errors.

Therefore, the Ewald sphere can be considered flat with respect to the reciprocal lattice and usually intercepts a very large number of rods. If the sample is oriented along a major symmetry axis, the DP is actually a whole section of the reciprocal lattice perpendicular to the direction of the incident electrons. The direction lying in all the planes appearing in the diffraction pattern is called **zone axis.** When the beam is parallel to this vector, the sample is said to lie in a zone axis.

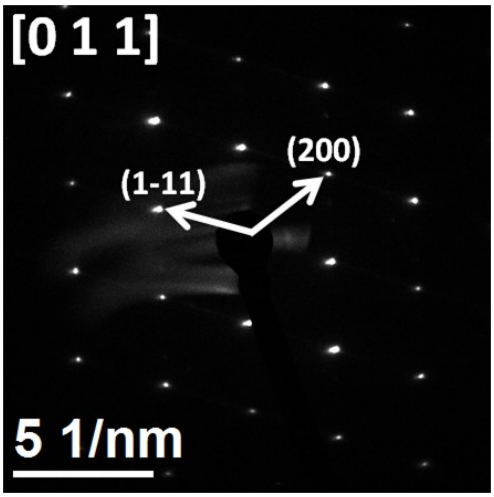

Figure 14: a typical diffraction pattern showing the [011] zone axis of a Silicon sample.

The nomenclature for the zone axis is mutated from the Miller notation for the atomic planes. A zone axis is named with three indexes *u, v* and *w* such as the vector [u v w] is orthogonal to any

reflection in the DP. The zone axis has not to be confused with the direction (u v w), orthogonal to the plane whit the same indexes, because with the exception of cubic lattices, the two are not necessary parallel.

Every dot in the DP represents a particular vector $\vec{g}$ in that section and contains the details on the spatial frequency, i.e. the frequency of the set of planes (hkl) from which it originated.

As an example, an experimental DP for a Silicon sample is reported in Figure 14. The length of the $\vec{g}$ corresponding to two diffraction spots has been measured and they have been identified as the (200) and the (1-11) reflections. Therefore the zone axis can be indexed as the [011].

A particular case is represented by the hexagonal lattices, which have three equivalent directions on the basal plane. In order to make this equivalence more apparent, a 4 indices notation is used where the fourth index is equal to *i=-h-k* and the reflections are indexed in the form (*h k i l*), with the first three indexes commutating. For example, the equivalence between the (110) and (1-20) hexagonal directions is more obvious if they are written in the forms (11-20) and (1-210).

2.5 Image formation mechanism

The treatment of the phase contrast imaging can be developed using the formalism of the information theory. The electron microscope can be modeled as a series of communication channels that sequentially act on the incident electron beam; each of them is described by its transfer function. The main channels are:

- The interaction between the electrons and the specimen
- The information transfer inside the microscope

The overall transfer function of the microscope is the combination of the transfer function of the individual channels. As a general remark, the transfer functions affect the wave function of the electrons, being therefore complex quantities with a modulus and a phase.
As a first approximation, the effect of the microscope is to transform each point of the sample in a disc in the final image, as discussed in chapter 2.3. The function describing this transformation, $h(\vec{r})$, is called **point spread function (PSF)**.

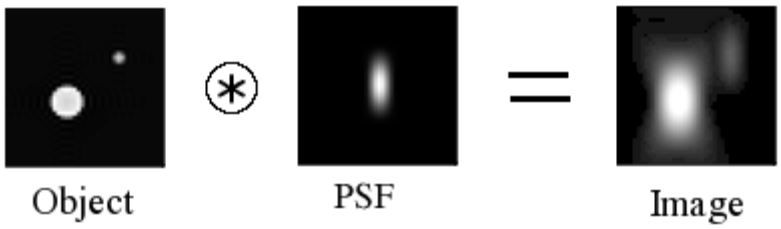

Figure 15: Image formation in the microscope.

Any imaging device is fully characterized when its PSF is known. In fact, the final image $g(\vec{r})$ is the convolution of $h(\vec{r})$ with the object function $f(\vec{r})$ as represented in Figure 15:

$$g(\vec{r}) = \int f(\vec{r}')h(\vec{r} - \vec{r}')d\vec{r}' = f(\vec{r}) \otimes h(\vec{r}) \tag{2.9}$$

It is convenient to work in the reciprocal space in order to exploit the convolution theorem for the Fourier transforms. This simplifies equation 2.9 in:

$$G(\vec{u}) = F(\vec{u})H(\vec{u}) \tag{2.10}$$

Where $\vec{u}$ is the spatial frequency and the functions named with the capital letters are the Fourier transforms of the corresponding lower case letter functions in equation 2.9.

The Fourier transform of the point spread function, $H(\vec{u})$, is the microscope **transfer function** and describes the way how each spatial frequency is transferred to the image.

$H(\vec{u})$ is a very complicated function accounting for any factor influencing the electron beam inside the microscope. The main contributions include:

1. Apertures: described by the aperture function $A(\vec{u})$
2. Attenuation of the wave: described by the envelope function $E(\vec{u})$
3. Aberration of the lenses: described by the aberration function $B(\vec{u})$

We write $H(\vec{u})$ as the product of these three terms:

$$H(\vec{u}) = A(\vec{u})E(\vec{u})B(\vec{u}) \tag{2.11}$$

The effect of the aperture function $A(\vec{u})$ is to allow only certain frequencies to be transmitted by the microscope and to cut off all the frequencies exceeding the aperture radius.

The resolution is also limited by the spatial coherence of the source and by chromatic effects. The exact mathematical form of these effects is complex but we can include them by imposing on the transfer function the envelope function $E(\vec{u})$ that further reduces the maximum frequency below the cut off imposed by the aperture.

Finally, the aberration function $B(\vec{u})$ is simply the phase shift due to the aberration, as already formalized in equation 2.4, $B(\vec{u}) = e^{i\chi(\vec{u})}$.

The effect of the sample is more important: it transforms the incident wave into the function $f(\vec{r})$. If the sample is very thin, as indeed are the specimens prepared for TEM observation, it is possible to assume that the sample acts exclusively on the phase of the incident wave while leaving unchanged the amplitude.

This approximation goes under the name of **phase object approximation** and was first proposed by Van Dyck. [10] Following his arguments, it is also possible to show that the phase change is

solely due to the potential that the electrons feel while passing through the sample as schematically shown in Figure 16.

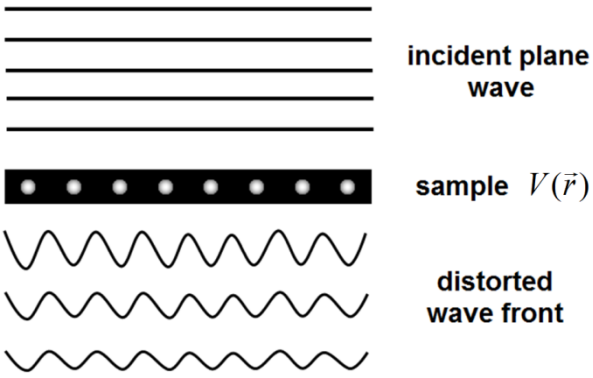

Figure 16: schematics of the phase object approximation.

During their motion in the sample, the electrons feel the effect of the local lattice potential $V(\vec{r})$ and consequently the wavelength changes.

In a non relativistic framework, accounting for the lattice potential, equation 2.1 becomes:

$$\lambda = \frac{h}{\sqrt{2me[E + V(\vec{r})]}} \tag{2.12}$$

Assuming the electrons are travelling along the *z* direction, the phase shift between the electron travelling through the specimen and those travelling outside it, for a thin slice whit thickness *dz* is:

$$d\varphi = 2\pi\frac{dz}{\lambda'} - 2\pi\frac{dz}{\lambda} = 2\pi\frac{dz}{\lambda}\left(\frac{\sqrt{E + V(\vec{r})}}{\sqrt{E}} - 1\right) \approx \sigma V(\vec{r})dz \tag{2.13}$$

Where the interaction constant $\sigma = \frac{\pi}{\lambda E}$. The total phase shift is obtained by integrating equation 2.13 over the whole sample thickness

$$\varphi = \sigma\int V(\vec{r})dz = \sigma V_T(x,y)dz \tag{2.14}$$

The total phase shift is hence dependent on the projected potential along the z direction $V_T(x,y)$ and the object function takes the form $f(x,y) = e^{-i\sigma V_T(x,y)}$.

We can further simplify the model if the specimen is very thin, so that $V_T(x,y) << 1$.Then we can expand the object function to the first order. The $f(x,y)$ becomes

$$f(x,y) = 1 - i\sigma V_T(x,y) \tag{2.15}$$

The last assumption is called the **weak-phase object approximation** (WPOA). The WPOA essentially says that, for a very thin specimen, the amplitude of a transmitted wave function will be linearly related to the projected potential of the specimen.

It is now possible to evaluate the final image by replacing equation 2.15 into equation 2.9:

$$g(x,y) = \left[-i\sigma V_T(x,y)\right] \otimes h(x,y) \tag{2.16}$$

If we represent the complex function $h(x,y)$ in the general form $h(x,y) = \cos(\mathrm{Re}[h]) + i\sin(\mathrm{Im}[h])$ then $g(x,y)$ becomes:

$$g(x,y) = 1 + \sigma V_T(x,y) \otimes \sin(\mathrm{Im}[h]) - i\sigma V_T(x,y)\cos(\mathrm{Re}[h]) \tag{2.17}$$

The image intensity is given by $|g(x,y)|^2 = g(x,y)g^*(x,y)$. After the multiplication is carried out and neglecting the terms in σ^2, because σ is small we find that:

$$I(x,y) = 1 + 2\sigma V_T(x,y) \otimes \sin(\mathrm{Im}[h]) \tag{2.18}$$

Knowing this result, it follows that under the WPOA, only the imaginary part of aberration function $B(\vec{u})$ contributes to the intensity, being it the only imaginary part of $H(\vec{u})$. Thus, it is possible to simplify $B(\vec{u}) = 2\sin[\chi(\vec{u})]$. This brings the transfer function to its final form:

$$H(\vec{u}) = 2A(\vec{u})E(\vec{u})\sin[\chi(\vec{u})] \tag{2.19}$$

Summarizing, if the sample is thin enough to satisfy the WPOA it introduces a modulation in the phase of the incident electrons proportional to the lattice potential and therefore characterized by specific frequencies. Each frequency is transmitted in a different way by the microscope according

to the microscope transfer function which coincides with the sine of the aberration function under the WPOA conditions. Being the transfer function proportional to sine it has several zeros. This means that some frequencies are filtered out by the microscope and cannot be found in the image. In order to avoid losing information, i.e. frequencies that are needed for a correct interpretation of the crystal lattice, the correct optical parameters have to be chosen in order to reduce the number of zeros.

If only defocus and spherical aberration are considered, equation 2.4 can be written in a simplified form $\chi(\vec{u}) = \pi \Delta f \lambda u^2 + \frac{1}{2}\pi C_s \lambda^3 u^4$. Being C_s a fixed parameter, the only way to influence the transfer function is changing the defocus. In Figure 17 the function $\sin[\chi(\vec{u})]$ is reported for three different defocus values.

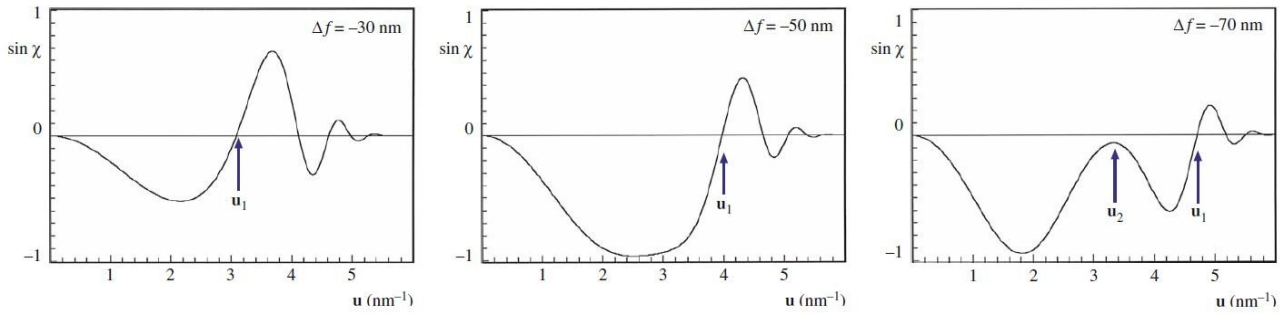

Figure 17: defocus series for the function sin[χ(u)] (V = 200 kV; Cs=1.0 mm).

The transfer function is very sensitive to the focus and small changes can drastically affect the number and the position of the zeros, marked by the black arrows in Figure 17.

The best transfer function, among the three shown, is the central one because it has the fewest zeros and nearly constant amplitude over the wider range of frequencies. Both these features largely simplify the interpretation of the image contrast.

For each Cs value, a particular defocus exist which optimize the transfer function. This defocus condition is known as Scherzer defocus [8] and its value is $\Delta f_{Sch} = -1.2(C_S \lambda)^{1/2}$.

An example of transfer function, considering the effect of the aperture and the envelope function, calculated for Scherzer defocus is shown in Figure 18.

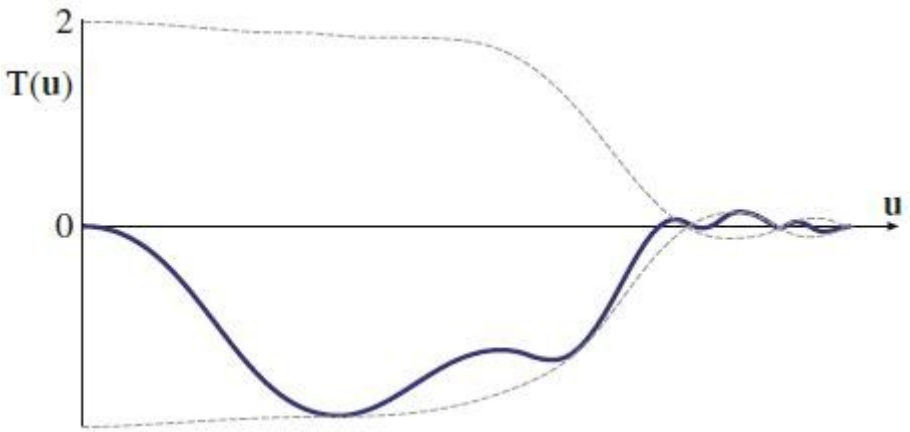

Figure 18: the contrast transfer function versus wave vector u modified by the damping factor (dashed line); Δf = -100 nm, Cs = 2.2 nm.

It has to be stressed that this way of interpreting the high resolution electron micrograph (HREM) images is valid only until the WPOA is valid. Unfortunately the WPOA holds true only for very thin samples. The actual thickness limit depends on many parameters such as the atomic number of the species composing the specimen, its density, the zone axis, etc… Therefore a great care has to be taken during the interpretation of the HRTEM images.

Figure 19 shows a set of simulations of HREM images for a [110] zone axis GaAs sample[11], whose atomic structure is reported in the bottom right corner for comparison, at different defoci and thickness.

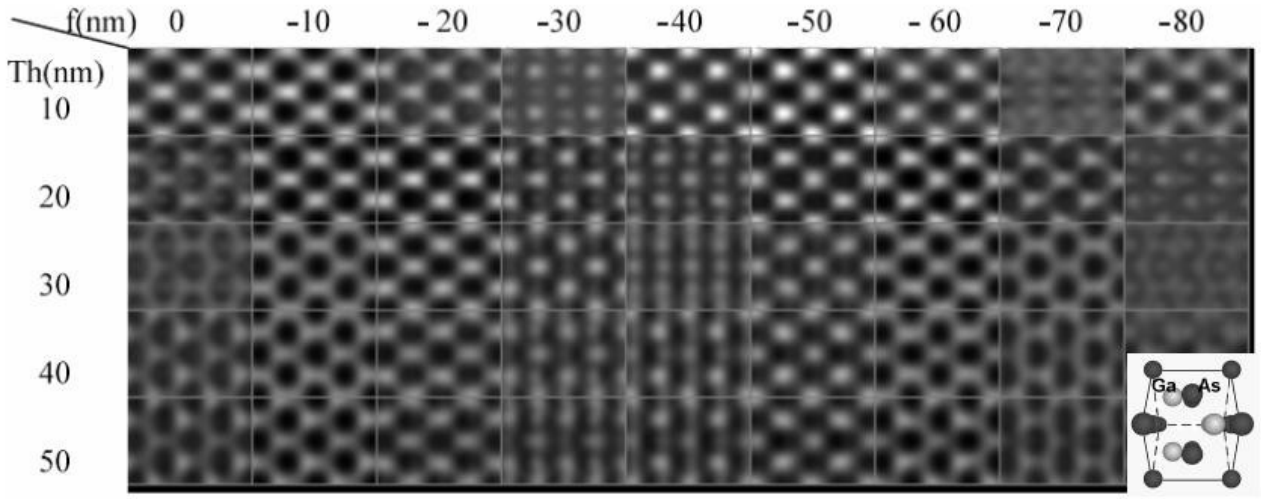

Figure 19: Simulation of HRTEM images for different values of thickness and defocus for a GaAs sample in a [110] zone axis (Cs = 0.5 mm).

The bright spots in the images are directly related to the atomic position in few cases only, sometimes with a contrast reversal though. In other cases the images cannot be compared with the crystal structure at all.

Nevertheless, despite the contrast, the spatial frequencies are always the same, only the relative intensities change.

Today's analysis softwares are able to extract these frequencies from the images by using Fast Fourier Transform (FFT) Algorithms. The Fourier transform of a HREM image shows bright spots at the spatial frequencies of the real lattice and, as a result, it will be a representation of the reciprocal lattice comparable with a diffraction pattern.

2.6 Scanning TEM (STEM) mode

Unlike the conventional TEM operation mode so far described, in which the beam illuminates a part of the sample at least as large as the entire area of interest, in STEM mode the electron beam is focused into a narrow spot, called probe, which is scanned over the sample in a raster.

Scan coils allow moving the probe on the sample and the electrons that interacted with the sample are then collected and their intensity reported as function of the probe position to form the image.

If a thin sample is oriented along a major zone axis, the primary electrons are confined by the Coulomb potential of the atomic columns. From a classical point of view, while passing through an atomic plane the electrons are attracted towards the positively charged nuclei and they gradually change their path, according to the graphical representation in Figure 20, to follow the direction of one atomic column. This phenomenon is called channeling and will be discussed more in details ahead in this chapter.

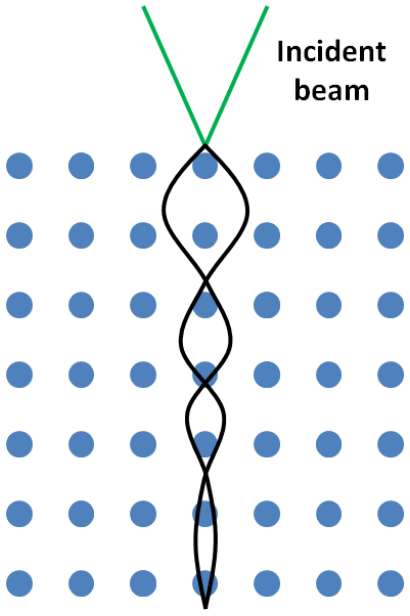

Figure 20: graphical representation of the electron channeling.

Thanks to the channeling, the probe doesn't spread away while travelling inside the sample so the spatial resolution, in STEM mode, is mainly controlled by the dimension of the probe at the entrance surface of the specimen. In modern microscopes it is possible to obtain probes as small

as 1 Å, a dimension smaller than the interatomic distances of many materials, so that atomic resolution images are now routine.

In order to get the smallest probe possible a large beam convergence is needed but, as shown in chapter 2.3, off-axis rays are strongly affected by the lenses aberrations thus they are the main limiting parameters to the STEM resolution. Hence obtaining the best probe size requires reducing the acceptance angle of the objective lens to exclude the rays that are most affected by the aberrations. This is achieved by means of an aperture in the image plane of the objective lens.

The aperture is represented in the front focal plane of the objective lens by a two-dimensional step function $H_\alpha(\vec{k})$, whose value is 0 if the $\vec{k}$ vector lies outside the convergence angle α and 1 inside. In other words, the probe is formed by a set of plane wave with wavevectors $\vec{k}$ having the same modulus and with direction uniformly distributed in an illumination cone with angle α.

If we combine now the effect of the aberrations with the effect of the aperture, we obtain the function describing the probe in the front focal plane of the objective lens: $A(\vec{k}) = H_\alpha(\vec{k})e^{i\chi(\vec{k})}$.

The front focal plane of the objective lens is conjugate to the sample plane thus the probe wavefunction $P(\vec{r})$ can be obtained by Fourier transforming $A(\vec{k})$:

$$P(\vec{r}) = \int H_\alpha(\vec{k})e^{i\chi(\vec{k})}e^{-i2\pi\vec{k}\cdot\vec{r}} \tag{2.20}$$

For a fixed value of C_s it is also possible to calculate the optimal defocus value and the maximum usable aperture:

$$\alpha = 1.3\lambda^{\frac{1}{4}}C_S^{-\frac{1}{4}} \tag{2.21}$$

The radial profile of the probe intensity $|P(\vec{r})|^2$, calculated according equation 2.20 at optimal defocus and aperture radius for a Cs=0.5 mm, is reported in Figure 21, while a two dimensional simulation of the probe intensity is reported in the inset.

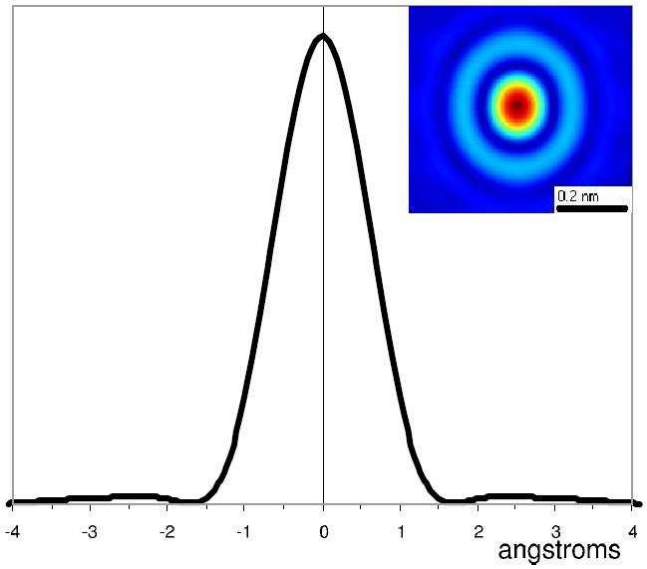

Figure 21: radial intensity profile of the simulated probe, shown in the inset.

The intensity profile provides a useful measure of the theoretical resolution limit that is assumed to be equal to the full width at half height of the profile. For optimal values of the defocus and the object lens aperture it is:

$$d = 0.44\lambda^{\frac{3}{4}} C_S^{\frac{1}{4}} \tag{2.22}$$

As an example, for a microscope working at 200 kV equipped with an objective lens having $C_s = 0.5\,\mathrm{mm}$, the theoretical resolution is 1.19 Å, and atomic resolution can be obtained.

The detectors are placed immediately below the sample, in the back focal plane of the objective lens, and consist of a series of concentric rings, centered on the optical axis, to incoherently integrate the signal over a large symmetric surface.

The detectors are classified, according their inner radius in Dark Field (DF) and Bright Field (BF) detectors, as shown in Figure 22.

The BF detector, so called because it covers the bright transmitted beam, has a radius of few mrads.

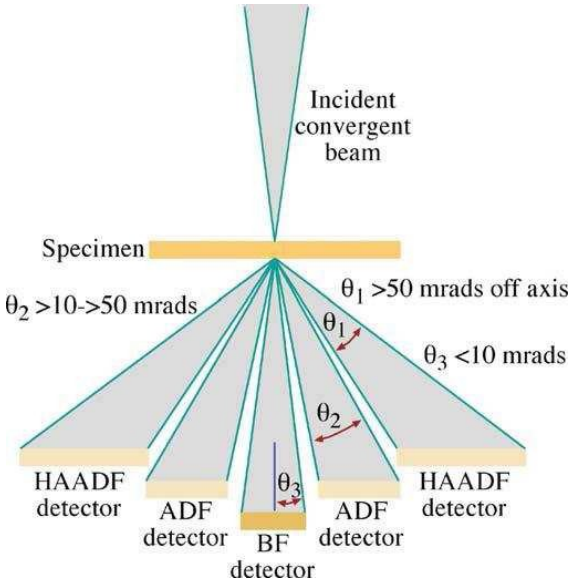

Figure 22: Schematic layout of the HAADF detector. It also shows the conventional ADF and BF detectors with the respective detection angles.

The annular DF (ADF) detector, so called for its shape, covers an angle ranging from 10 through 50 mrad. Lastly, the high angle ADF (HAADF) detector covers an angular range typically exceeding 50 mrad.

The main advantage of imaging with the HAADF detector, compared to other high resolution techniques, is related to the fundamentally incoherent nature of the scattering occurring at such a high angle [12], as shown in Figure 23.

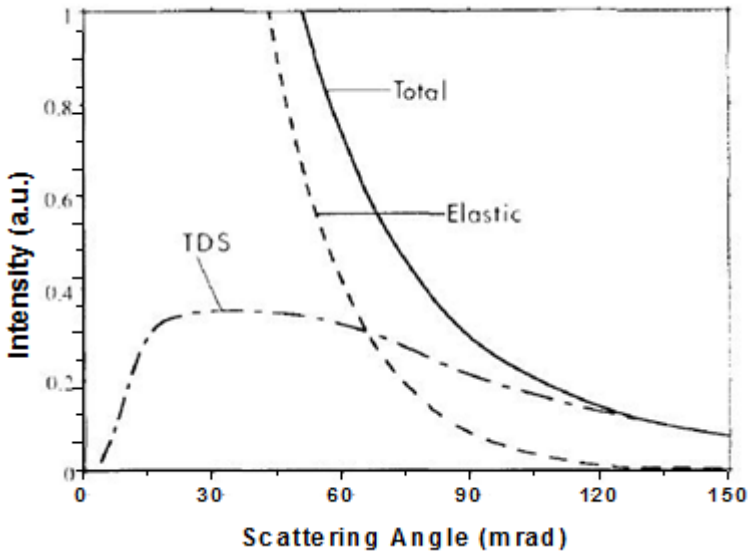

Figure 23: the total, elastic and thermal (TDS) scattering amplitude for an isolated silicon atom at room temperature per unit of solid angle.

As the scattering angle increases, thermal diffuse scattering becomes increasingly important, eventually dominating the scattering. The thermal scattering is governed by a Rutherford cross section whose intensity depends on the potential of the unscreened nucleus.

The intensity of a HAADF image depends on atomic number. In fact, the intensity is proportional to Z^{α} with 1.7<α<2 and for this reason the technique is also called Z-contrast imaging.

A lower intensity in HAADF images is thus given by material with a lower atomic number. Conversely, a higher intensity relates to heavier elements, for the same thickness.

Although predominant, Z is not the only component of the image contrast. An accurate definition of the cross section is in fact:

$$\frac{I(\vec{r})}{P^2(\vec{r})} = N\sigma t \tag{2.23}$$

Also the density of scattering centers *N* and the sample thickness *t* influence the image contrast.

In conclusion, being the Rutherford scattering intensity high only close to the atomic positions, HAADF images can be represented as the convolution of the probe with a suitable object function.

$$I(\vec{r}) = O(\vec{r}) \otimes P^2(\vec{r}) \tag{2.24}$$

The object function $O(\vec{r})$ is usually the projected potential of the whole specimen.

Although this simple model provides an easy way to qualitatively interpret the HAADF images, it cannot be used for a quantitative analysis. Moreover, the simple Z-contrast interpretation, neglects other dynamical effects that may affect, even though not significantly, the image contrast. Especially, when the inner detection angle is not high enough, defects and strain fields can affect the image contrast.

For a correct interpretation of the TEM images, both conventional HREM and HAADF-STEM, it is usually necessary to resort to image simulations.

2.7 Bloch wave theory

So far a phenomenological description of the electron-material interaction has been given. This is, in many cases, sufficient to relate the images to the structure of the specimen. However, if we want to obtain quantitative results from the experiment, before recurring to the image simulation, we need to understand what goes on in the sample. The Bloch waves theory provides an accurate description of how the electrons behave inside the sample and, at the same time, a tool for image simulations.

The following analysis is just a summary of the original work of Bethe[13]. Please refer to this paper for a detailed treatment of the problem.

The starting point of the treatment is the time-independent Schrödinger equation:

$$\left[-\frac{h^2}{8\pi^2 m}\nabla^2 + v(\vec{r})\right]\Psi(\vec{r}) = E\Psi(\vec{r}) \tag{2.25}$$

The first term (in ∇^2) represents the kinetic energy and the second term, the potential energy; E represents the total energy. As in TEM we usually talk of acceleration voltage V_a it is useful to redefine equation 2.25 in terms of voltages.

Being $E = -eV_a$ and $v(\vec{r}) = -eV(\vec{r})$, assuming they are positive, equation 2.25 becomes:

$$\nabla^2\Psi(\vec{r}) + \frac{8\pi^2 me}{h^2}\left[V_a + V(\vec{r})\right]\Psi(\vec{r}) = 0 \tag{2.26}$$

Because we are working with crystals, $V(\vec{r})$ is periodic: $V(\vec{r}) = V(\vec{r} + \vec{R})$ with $\vec{R}$ any lattice vector of the crystal. It can be expressed as a Fourier series in which we sum over all the lattice points of the reciprocal space $\vec{g}$.

$$V(\vec{r}) = \sum_g V_g e^{2\pi i\vec{g}\cdot\vec{r}} \tag{2.27}$$

Here V_g is, by definition, the *g* component of $V(\vec{r})$ in the Fourier series. It can come handy to redefine the Fourier components, in order to make future equations easier, introducing the parameter $U_g = \frac{2me}{h^2} V_g$.

The new Fourier coefficients U_g posses the same properties of the old ones. Being $V(\vec{r})$ positive and real, its Fourier components are real and symmetric: $U_g = U_g^* = U_{-g}$.

Since the electrons are travelling in a periodic potential, their wave function must have the symmetry of the crystal. The solutions of the Schrödinger equation having the required translation property are known as Bloch waves. According to the Bloch's theorem this wave function can be written as:

$$b^{j,k}(\vec{r}) = \mu(\vec{r}) e^{2\pi i \vec{k} \cdot \vec{r}} \tag{2.28}$$

Where j is an integer and $\vec{k}$ is a real vector within the first Brilluin zone.

Each Bloch wave is a plane wave with wave vector $\vec{k}$ multiplied by a periodic function $\mu(\vec{r})$, called the Bloch function. Being $\mu(\vec{r})$ a periodic function, can be expressed as a Fourier series: $\mu(\vec{r}) = \sum_g C_g^j e^{2\pi i \vec{g} \cdot \vec{r}}$. The Bloch waves become:

$$b^{j,k}(\vec{r}) = \sum_g C_g^j e^{2\pi i (\vec{g} + \vec{k}) \cdot \vec{r}} \tag{2.29}$$

According to the equation 2.29, each Bloch wave is associated with just one $\vec{k}$ but it is a continuously varying function of $\vec{r}$. At the same time, each Bloch wave is a sum over all the points of the reciprocal space. In other words, each Bloch wave depends on every $\vec{g}$, and conversely, each $\vec{g}$ beam depends on every Bloch wave.

It is possible to demonstrate that for a plane wave illumination only a single $\vec{k}$ is excited for each band j. Therefore, as long as plane wave illumination is used (as in TEM), we will drop the k index. Also, we will use the symbol $\vec{k}_j$ to indicate the unique $\vec{k}$ associated to a band j at the given plane wave condition.

The solution of the Schrödinger equation in a TEM is therefore a linear combination of Bloch waves expressed as:

$$\Psi(\vec{r}) = \sum_{j=1}^{n} A^j b^j(\vec{r}) \tag{2.30}$$

The coefficients A^j are called *excitation coefficients*. They tell us the relative contribution of each Bloch wave to the final wavefunction and are eventually responsible for the image intensity.

The A^j coefficients are determined by the boundary conditions imposed by the specimen, such as the specimen type and orientation.

We rewrite the Schrödinger equation to automatically incorporate the properties of the Bloch waves by replacing the lattice potential in equation 2.26 with the expression given in equation 2.27:

$$\frac{1}{4\pi^2}\nabla^2\Psi(\vec{r}) + \left(\frac{2me}{h^2}V_a + \sum_g U_g e^{2\pi i\vec{g}\cdot\vec{r}}\right)\Psi(\vec{r}) = 0 \tag{2.31}$$

We can further manipulate this equation excluding the term with $\vec{g} = 0$ from the sum. As a matter of fact, the U_0 is a continuum property of the crystal and does not depend on the orientation. It represents the mean inner potential of the crystal. Equation 2.31 becomes

$$\frac{1}{4\pi^2}\nabla^2\Psi(\vec{r}) + K^2\Psi(\vec{r}) + \sum_{g\neq 0} U_g e^{2\pi i\vec{g}\cdot\vec{r}}\Psi(\vec{r}) = 0 \tag{2.32}$$

Where we have defined:

$$K^2 = \frac{2me}{h^2}V_a + U_0 = \chi^2 + U_0\,. \tag{2.33}$$

In order to understand the meaning of K, first consider the case of an electron traveling in the vacuum, then $U_0 = 0$. The remaining term χ is simply the wave vector of the electron in the vacuum, therefore K is the wavevector inside the crystal.

It is worth noting now that, being $V(\vec{r})>0$, also $U_0>0$ and $K>\chi$, therefore electrons travel faster in the crystal than they do in the vacuum, in opposition with what the light does.

Moreover, equation 2.33, provides a dispersion relation for the electrons in the crystal.

It is now possible to replace the expression for the general solution $b^j(\vec{r})$, equation 2.29, and obtain the final form of the Schrödinger equation:

$$\frac{1}{4\pi^2}\left(-4\pi^2\sum_g\left|\vec{k}_j+\vec{g}\right|^2 C_g^j e^{2\pi i\left(\vec{k}_j+\vec{g}\right)\cdot\vec{r}}\right)+K^2\sum_g C_g^j e^{2\pi i\left(\vec{k}_j+\vec{g}\right)\cdot\vec{r}}+\sum_{h\neq 0}U_h e^{2\pi i\vec{h}\cdot\vec{r}}\sum_g C_g^j e^{2\pi i\left(\vec{k}_j+\vec{g}\right)\cdot\vec{r}}=0 \qquad (2.34)$$

For clarity $\vec{h}$ replaces the $\vec{g}$ vector appearing in equation 2.32, but both represent a vector of the reciprocal lattice. In the third term we are summing over all the $\vec{g}$ vectors, therefore it is licit to rename $\vec{g}=\vec{g}-\vec{h}$. This substitution further simplifies the equation:

$$\sum_g\left(\left\{-\left|\vec{k}_j+\vec{g}\right|^2+K^2\right\}C_g^j+\sum_{h\neq 0}U_h C_{g-h}^j\right)e^{2\pi i(\vec{k}_j+\vec{g})\cdot\vec{r}}=0 \qquad (2.35)$$

As $e^{2\pi i(\vec{k}_j+\vec{g})\cdot\vec{r}}$ is a phase factor, equation 2.35 is true only if all the terms in the bracket are separately equal to zero. The result is a series of equations, one for each value of $\vec{g}$.

Changing again the name of the variable and replacing $\vec{h}=\vec{g}-\vec{h}$ the set of equation can be written as:

$$\left\{-\left|\vec{k}_j+\vec{g}\right|^2+K^2\right\}C_g^j+\sum_{h\neq g}U_{g-h}C_h^j=0 \qquad (2.36)$$

This set of equations are called the *secular equations* and are the fundamental equation in the dynamical theory. It is called dynamical because the many $\vec{g}$ beam are not simply travelling inside the specimen but are coupled together by the crystal potential, the U_{g-h} terms.

Due to the coupling of the Bragg vectors it is not possible to calculate every C_g^j but only the relative intensity C_g^j/C_0^j.

In a more compact notation, the set of equations 2.36 is expressed as:

$$T^j\left\{C_g^j\right\}=0 \tag{2.37}$$

Where T^j is a matrix whose diagonal terms are $t_{gg}=K^2-\left|\vec{k}_j+\vec{g}\right|^2$, and the off-diagonal terms are $t_{gh}=U_{g-h}$, while $\left\{C_g^j\right\}$ is a column vector with elements C_g^j.

The problem can now be solved by diagonalizing the matrix T^j.

A more detailed analysis demonstrates that it is possible to further simplify. In fact, the propagation along z is much faster than in x and y (high energy approximation) and the 3D problem can be reduced to a 2D one. In this approximation it is still possible to introduce dispersion curves that relate the propagation velocity of each state with the quantum numbers k and j. In any case the dispersion surface is calculated by imposing the condition $\det\left|T^j\right|=0$.

The first six branches of the dispersion surface are shown in Figure 24.

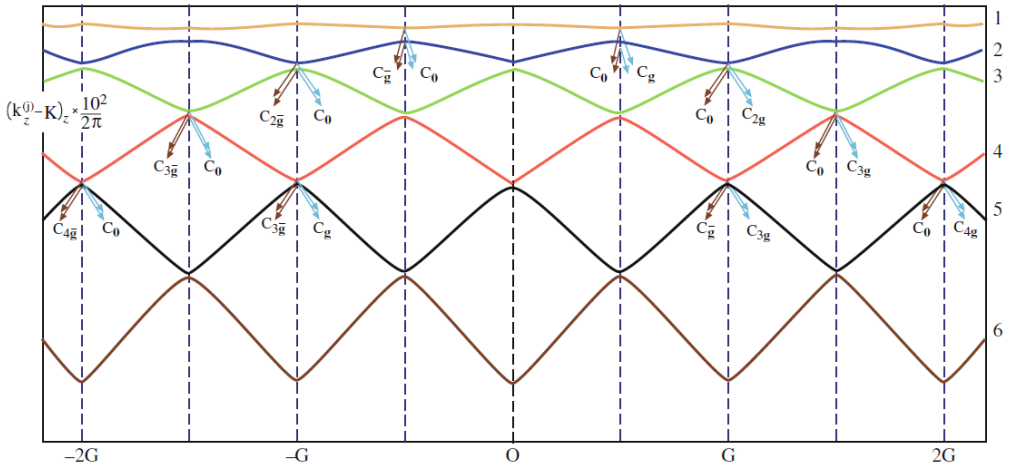

Figure 24: The first six branches of the dispersion surface.

Each branch of the dispersion surface relates to a Bloch state and the shape of the first 4 Bloch states, calculate for a (110) zone axis GaAs sample, are reported in Figure 25, together with the unit cell.

The Bloch states are similar to a set of molecular orbitals comprising bonding and antibonding (denoted by *) combinations therefore the same nomenclature is used: we call 1s state the highest energy state which is confined on the atomic columns, and so on.

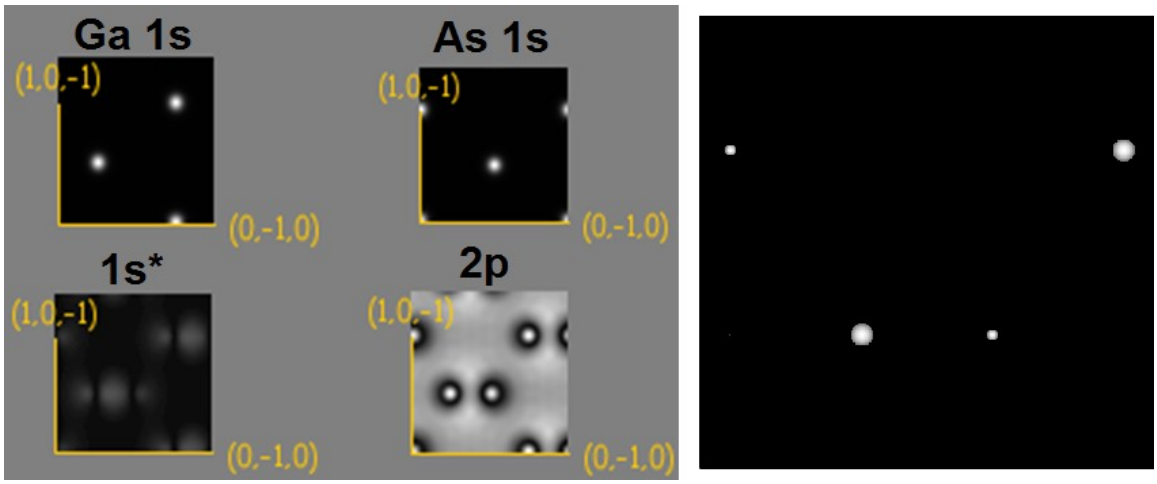

Figure 25: the first 4 Bloch states, calculate for a [110] zone axis GaAs sample, reported on the right (big atoms Ga, small atoms As)

In summary, when the primary electrons enter the crystal they speed up due to the lattice potential. Also, the lattice potential is periodic so the wavefunction describing the electrons in the vacuum is no longer valid. Hence the primary beam wavefunction is projected on the Bloch States here described.

The imposition of the appropriate boundary condition is typically performed by assuming the phase matching of the waves at the entrance of the sample.

Another equivalent approach is to calculate the excitation coefficients A^j as projection of the electron wavefunction $P(\vec{r})$ at the entrance of the sample onto each Bloch state. This approach can be useful in the case of the convergent illumination (e.g. STEM).

The boundary condition on the entrance surface of the specimen, remembering equation 2.30, is:

$$\Psi(\vec{r}) = \sum_j b^{j,k}(\vec{r}) \int P(\vec{r}) b^{j,k}(\vec{r})^* d\vec{r} = \sum_j A^{j,k} b^j(\vec{r}) \tag{2.38}$$

Notice that now we used both j and k quantum numbers in the description of the Bloch wave. The dependence on $\vec{k}_j$ can be neglected only for the non dispersive 1s state.

It turns out that, both in TEM and STEM, when the sample is oriented along a high symmetry zone axis, the excitation coefficient A^j is large only for the first few Bloch states.

This means that only a small number of Bloch waves determine most of the appearance of the HREM images [14][15], providing the crystal has a sufficiently high symmetry. In this context we can also redefine the channeling condition as a strong excitation of the 1s state: $A^{1s} >> 0$.

Since every Bloch wave is travelling inside the sample with a different speed, a phase difference between them will soon arise. This phase is responsible for the interference between the Bloch states and, in turn, for contrast in HREM images.

2.8 Multislice simulations

As shown in the previous section, the Bloch wave theory is a powerful tool for the interpretation of the TEM images that, at the same time, explains the physics behind the image formation.
Unfortunately it only works for perfect crystals. By definition a crystal is infinite and the simple presence of a surface can be considered as a defect. A new approach must be considered in order to be fully quantitative .
The basic multislice approach is to section a realistic model of the specimen into many slices, which are normal to the incident beam. Because there are no constrains on the slice thickness and composition, every slice can be different from the others allowing for an accurate reproduction of the sample, even in presence of defects.
Every slice, depending on the computing time availability and the size of the sample itself, can be made as thin as a single atomic plane. For such a thin slice the WPOA surely holds true.
Remembering the equation 2.14, the wavefunction of the electrons emerging from the n-th slice can be written as:

$$\Psi_n(\vec{r}) = \Psi_{n-1}(\vec{r}) \times t_n(\vec{r}) \quad \textit{with} \quad t_n(\vec{r}) = e^{i\sigma V_n(\vec{r})} \tag{2.39}$$

Where $V_n(\vec{r})$ represents the projected potential of the n-th slice.
The electron wave then propagates, into the vacuum, to the next slice. The wavefunction on the following slice is calculated as the convolution of the previous one with the propagation function $p(\vec{r}, \Delta z)$, where Δz is the slice thickness which is assumed (for simplicity but it is not required) to be the same for all the slices. The phase term for the new slice is calculated and it is applied to the wave function which is then propagated to the next slice.
The calculation follows a recursive scheme till the exit surface of the specimen according the model proposed in Figure 26.

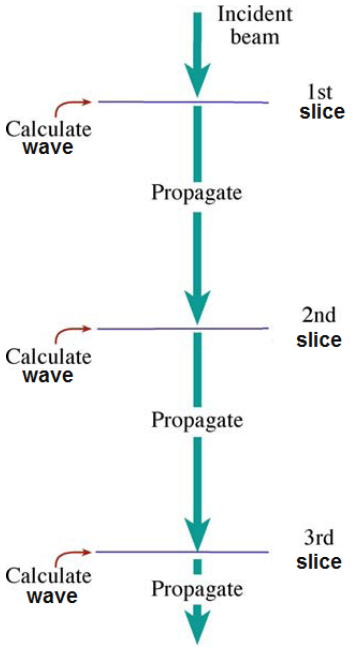

Figure 26: a schematics of the multislice simulation methods.

In formulas, it can be written as:

$$\begin{cases} \Psi_1(\vec{r}) = t_1(\vec{r})\Psi_0(\vec{r}) \\ \Psi_n(\vec{r}) = t_n(\vec{r})\left[\Psi_{n-1}(\vec{r}) \otimes p(\vec{r}, \Delta z)\right] \end{cases} \tag{2.40}$$

Where $\Psi_0(\vec{r})$ is the incident beam's wavefunction.

The square modulus of the wave exiting the last slice is the intensity of the respective HREM image while its FFT is the DP.

The intensity of the DP can be averaged on a suitable annular section to give the corresponding ADF-STEM intensity. In the latter case, the multislice simulation has to be performed on every pixel in order to get the final image.

Multislice simulations offer several advantages, even though they are more time-consuming, with respect to Bloch waves calculations.

First of all, they are not limited to perfect crystals; images of defects and grain boundaries can be easily simulated by carefully tailoring the sample. More over the thermal agitation can be included in the simulation.

This is very important for the simulation of HAADF-STEM images where the thermal diffuse scattering (TDS) plays a major role. The way to do this is trough the Einstein model.

We can assume the atoms move randomly and independently around their equilibrium position. Because the primary electrons are moving faster than the average thermal motion of the atoms they will see a single configuration, as the whole lattice is frozen during the vibration.

Therefore every atom in the sample is randomly displaced from its equilibrium position accordingly to its Debye-Waller factor. Then the multislice simulation is performed following the same scheme as in equation 2.40. The best result is achieved by incoherently summing over several configurations: usually more than 10 are necessary.

As already mentioned, the multislice algorithm offers the advantage to simulate defected and strained structures provided they are correctly modeled. This usually requires disregarding the specific symmetry and periodicity of the unit cell and treating the atomic positions independently from a possible unit cell shape. The whole modeling process is very challenging especially for wide samples that can easily contain thousands of atoms. All these needs can only be handled with a specific software dealing with the cells preparation and the parameters optimization.

The software used in this work is STEM_CELL [16][17], a simulation tool created by Doctor Vincenzo Grillo and based on the original work of E. J. Kirkland [18]. See appendix A for more details on the software.

During the thesis I personally worked of the development of the software, writing the input interface for the atomic models, see image A.2 in appendix A.

2.9 Energy Dispersive X-ray spectroscopy

The highly energetic primary electrons interact with the core electrons of the atoms composing the specimen. If, during the process, more than a critical amount of energy is transferred to this inner-shell electron, it escapes the attractive field of the nucleus, leaving a hole in the inner shell.
This interaction leaves the atom in an excited state so that it tries to return to its ground state by filling the hole with an electron from an outer shell. This transition is accompanied by the emission of a X-ray photon.
The name of the inner shells follows a particular nomenclature: the innermost electron shell is called the K shell and the next innermost is the L shell, the next the M, and so on. The difference between the two shells energies involved in the relaxation process equals the energy of the characteristic X-ray.
Each characteristic X-ray has a name as well, obtained by combining the name of the shell where the hole is filled and a letter from the Greek alphabet. Thus, if we fill a K-shell hole from the L shell we get a K_α X-ray, but if we fill it from the M shell we get a K_β X-ray. If the hole is in the L shell and we fill it from the M shell we get an L_α X-ray, while, if we fill it from the N shell we get an L_β X-ray. If we consider also the subshells the notation becomes even more difficult. The complete scheme of the possible characteristic X-rays is given in Figure 27.
Luckily, the cross section of only few of these spectral lines is high enough to give a signal detectable by the TEM. Moreover, being the energy resolution not better than 135 eV, the spectrometer is not able to resolve between α and β lines if they are too close. As a result, the number of detectable spectral lines is strongly reduced and all of them are comfortably recorded into the analysis softwares with their relative intensities.
The analysis software not only provides the identification of the atoms present in the specimen but also their abundance within a few % error.

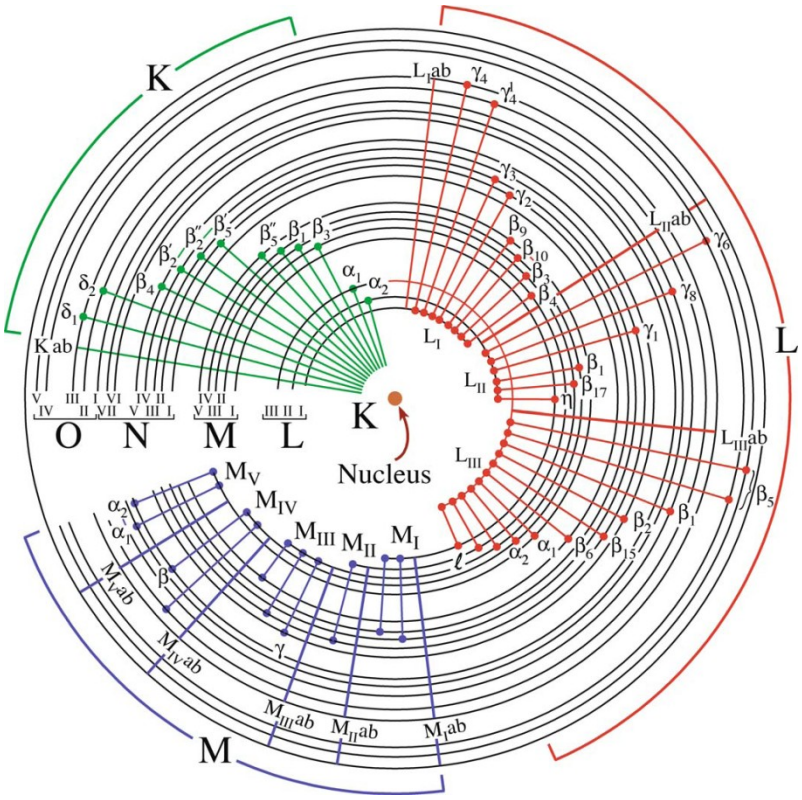

Figure 27: summary of all the possible X-ray lines.

If the analysis of the characteristic X-rays is performed during the scan in STEM mode, the quantitative analysis is achieved with a great lateral resolution.

As a result, elemental maps can be obtained, routinely with nanometric resolution and, in the modern Cs corrected microscope, with atomic resolution also.

Chapter 3: CATHODOLUMINESCENCE

Cathodoluminescence (CL) is the emission of light as the result of electron bombardment in an electron microscope and is an optical characterization technique with character of microscopy and spectroscopy at the same time.

CL occurs because the impingement of a high energy electron beam onto a semiconductor will result in the promotion of electrons from the valence band into the conduction band, leaving behind a hole. When an electron and a hole recombine, it is possible for a photon to be emitted. The energy of the photon and the probability that a photon will be emitted depends on the material, its purity, and its defect state. For these reasons the study of the CL emission spectra gives many information about the material itself. The technique does not limit to semiconductors but, in fact, it can be applied to almost any non-metallic material.

Although it can be performed in a TEM, cathodoluminescence is usually carried out in a Scanning Electron Microscope (SEM) owing to the higher current they can use that significantly increases the signal.

The scheme of a typical SEM-CL apparatus is shown in Figure 28.

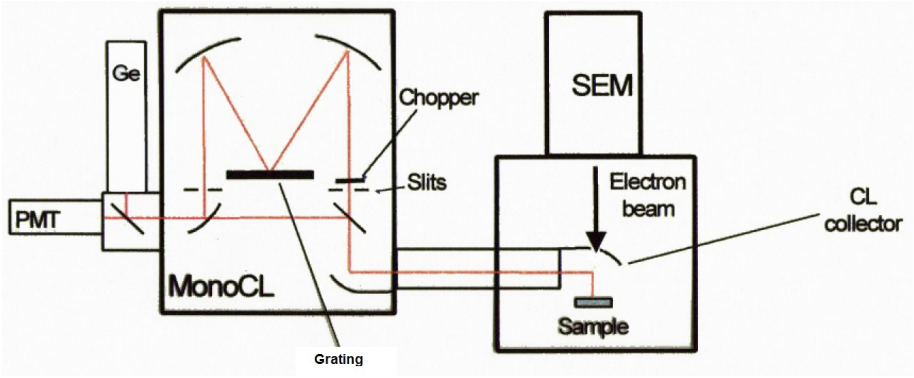

Figure 28: a typical SEM-CL apparatus.

The electron beam is generated by the SEM electron gun and accelerated at voltages ranging from a few hundred Volts to 40 kV. The electrons are then focalized by a system of electromagnetic lenses, usually 2 condenser lenses and 1 objective lens, which control the diameter and the angular divergence of the electron beam. The resulting beam size on the sample surface, which is a fundamental parameter to reach a good spatial resolution, typically ranges between a few microns and a few tens of nanometers. However, the actual analytic and in-depth resolution is not simply the lateral resolution at the surface, but depends on the generation volume determined by the incident beam energy and by the physical properties of the sample.

Typical Monte Carlo plots, visualizing the electron trajectories and the lateral and in-depth dose function are reported for example in Figure 29.

The effects of beam energy, sample thickness and material density on the size and shape of the carrier generation distribution can be studied directly. For low energy, high density and thick specimens the distribution is found to be a small hemisphere centered about the surface; as the energy/density ratio increases it becomes spherical, bigger and has its origin below the surface; for highest energy/density ratios the distribution is pear shaped and much larger; for thin samples the shape is conical and much smaller. For nanostructured materials, the generation volume is limited by the actual thickness of the structure and usually coincides with the neck of the pear.

The electron-hole pairs are generated within this volume and start diffusing inside the specimen. The recombination, that produces the radiation, takes place in a region bigger than the generation volume according to the carrier diffusion length. These processes worsen the spatial resolution.

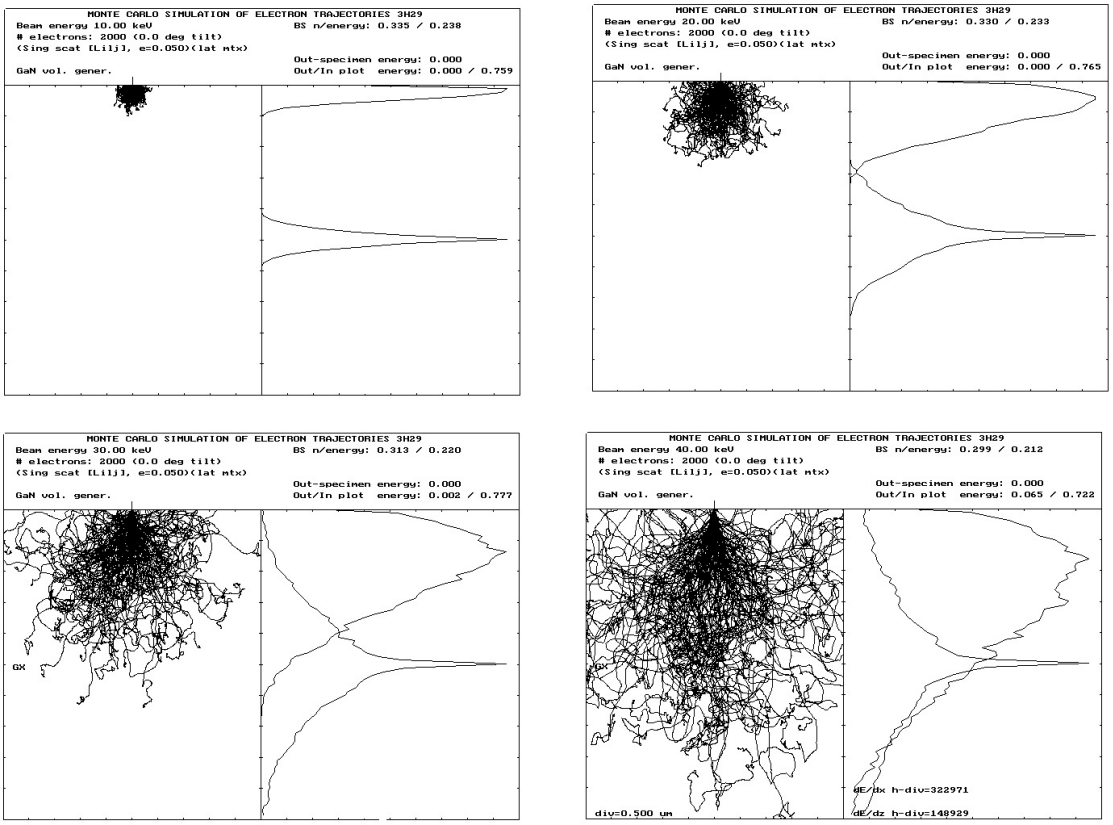

Figure 29: Monte Carlo simulations of the trajectories of the electrons in a SEM sample for increasing beam energy (10, 20, 30 and 40 KeV).

After the light is emitted, it is collected by a parabolic mirror and carried through a guide to the monochromator unit where a diffraction grating disperses the light which is finally detected and electronically processed for the spectral analysis.

Two kind of analyses can be performed: the spatial distribution of the total intensity can be acquired by scanning the electron beam in an X-Y pattern (panchromatic or monochromatic maps) exploiting the high in-plane and in-depth resolution of the SEM, or the spectrum from a selected area of the sample can be acquired and analyzed.

Each band in the CL spectra is related to a particular transition, i.e. a valence band to conduction band or an intraband defect mediated transition. SEM-CL can thus identify the nature and the spatial localization/density of such defects.

Chapter 4: (Ge)-Sb-Te NANOWIRES

4.1 Introduction

A promising research area in the wide materials science field is devoted to the study of the commonly called phase change materials (PCM). In the same temperature and pressure conditions, these materials are able to exist in at least two stable or metastable phases: an amorphous phase and one or more different crystalline phases. They are also characterized by a combination of properties that are usually not observed among the known materials: they have a pronounced difference of optical and electrical properties between the amorphous and crystalline phases, resulting from a different spatial arrangement of the atoms. Moreover, the phase change between the amorphous and crystalline state is extremely rapid. Because of this lucky combination of properties, PCM are used in data storage devices.

Chalcogenides are the most technological appealing compounds among PCM. They are semiconductor materials containing at least one element of the group VI of the periodic table, such as Sulphur (S), Selenium (Se) or Tellurium (Te). They exhibit marked differences between the crystalline and the amorphous phase, hardly found in other materials, and crystallization times of the order of tens of nanoseconds.

A significant number of Chalcogenides PCM can be placed on the ternary phase diagram containing the elements Germanium (Ge), Antimony (Sb) and Tellurium (Te) reported, as an

example, in Figure 30. Here, the most important Ge-Sb-Te compounds (GST) are reported; a more complete diagram can be found in reference [19].

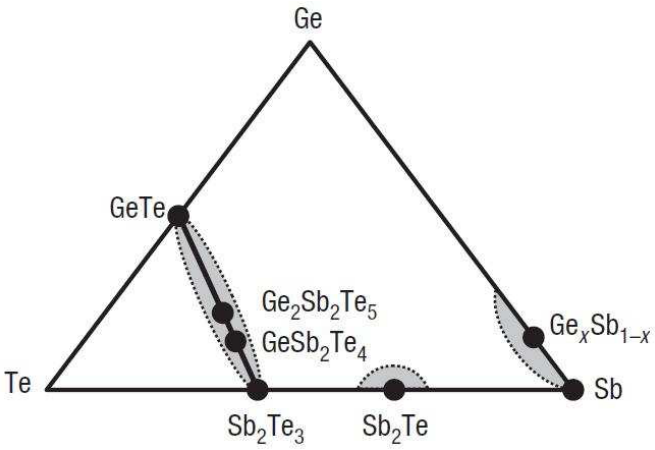

Figure 30: ternary diagram Ge-Sb-Te: the compounds representing the most studied and considered of technological interest are reported.

In the diagram the three areas within which it is possible to find PCM are highlighted, in particular the tie line joining the Germanium Telluride (GeTe) and the Antimony Telluride (Sb_2Te_3), which contains the first discovered PCM, namely the ternary alloys $Ge_2Sb_2Te_5$ and $Ge_1Sb_2Te_4$, that are the most used and studied compounds.

Their discovery, happened in 1987 [20], has in fact marked the birth of the technology for data storage on rewritable optical devices. This still is the predominant technology in the industry with the presence on the market of four generations of media: compact disc rewritable (CD-RW), digital versatile discs (DVDs), and the last arrived on the market, the Blue-ray disc (BD) single and dual layer.

Thanks to the success and rapid development of the PCM-based optical data storage technology, the research on the Chalcogenides has expanded towards the solid-state non-volatile memories, currently dominated by the "flash memory" technology, based on charge trapping. These are an essential component of integrated circuits due to their ability to retain the stored information even after the power has been switched off.

However, despite the wide commercial success of the flash technology, the semiconductor industries are looking for alternative solutions to improve the device performance (writing speed), and the possibility of integration (density of information stored per unit area).

The phenomenon allowing the PCM utilization in the electronic data storage devices was observed for the first time by Ovshinsky in 1968 [21]. He reported on the observation of the phase transition between a conductive state and a high-resistance state by means of an electric field in chalcogenide glasses. The two states were actually coinciding with the crystalline and the amorphous phase.

The operation principle of the PCMs is schematized in Figure 31.

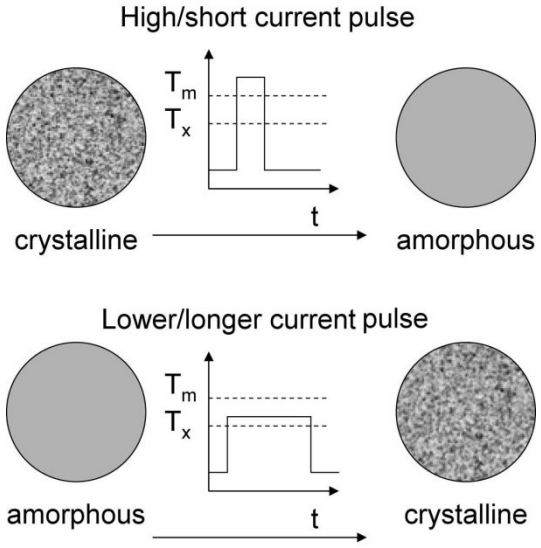

Figure 31: a schematic of the working principle of a PCRAM.

A 50 - 100 ns long current pulse through the memory cell causes the melting of the PCM. The current intensity and the pulse duration depend on the particular material and the geometry of the cell. At the end of the pulse, due to the small size of the melted area, there is an abrupt cooling (quenching) that "freezes" the material in the amorphous state. The reverse phase transition can, in principle, be obtained with a similar pulse, with lower intensity and longer duration, which increases the temperature above the glass transition point, but below the melting point, causing the crystallization.

Anyway, converting the active volume from the amorphous phase to crystalline one in a memory cell would require an extremely high voltage, exceeding 500 V, due to the high resistance of the amorphous phase. Powering a device with such a high voltage is unfeasible.

However, this limitation is overcome thanks to the particular feature of the I-V characteristic of the PCM shown in Figure 32.

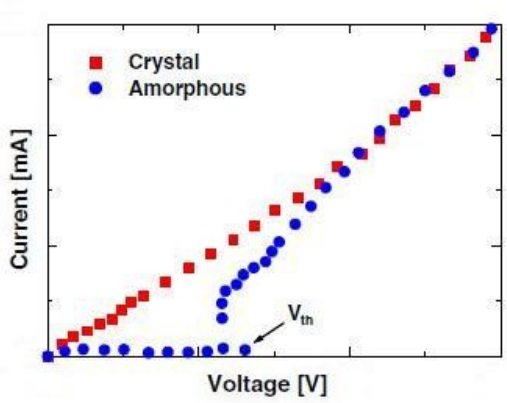

Figure 32: typical I-V curves for the crystalline (red squares) and the amorphous (blue circles) phases of GST compounds.

It can be noted how the resistance of the amorphous state is large only below a certain threshold potential. Above this value, V_{th}, the conductivity abruptly increases to the same value of the crystalline phase. This phenomenon is known as threshold switching and till now it is not completely explained.

The information can be read by measuring the resistance of the memory cell: a high resistance, due to the presence of amorphous material, is translated with a binary "0" state; vice versa, a low resistance, characteristic of a completely crystalline material, is translated as a "1".

Since the write/erase operations have both duration of about 50 - 100 ns, the device promises very high programming speeds, significantly improved in comparison with the Flash technology.

The main limitation of the PCM based memories is the huge programming current required to induce the transition from the crystalline to the amorphous phase. To reduce the programming current of a given PCM, it is necessary to lower the volume of PCM active layer employed in the memory cells.

The currently used method to reduce the device size, borrowed by the semiconductor technology, is said Top-Down and it is entirely based on the use of deposition techniques to reduce the thickness and sophisticated photolithography techniques to reduce the areas.

A strong limitation of the top-down methods prevents reducing the size of the devices: they require multiple steps of lithography and etching which can degrade the structural properties and the proper functioning of the devices.

Bottom-up is an alternative method which consists in exploiting specific growth processes in order to directly grow nanometric structures avoiding photolithographic techniques.

For example, in 2007, it has been shown that PCM NWs have a transition temperatures significantly lower than the bulk material: for the GeTe was observed a 46% reduction of the melting temperature [22]. Also other important properties scale down reducing the dimension. In a recent study on $Ge_2Sb_2Te_5$ NWs [23] it has been noted how the writing current and the power consumption scale down exponentially with NW thickness, as reported in Figure 33.

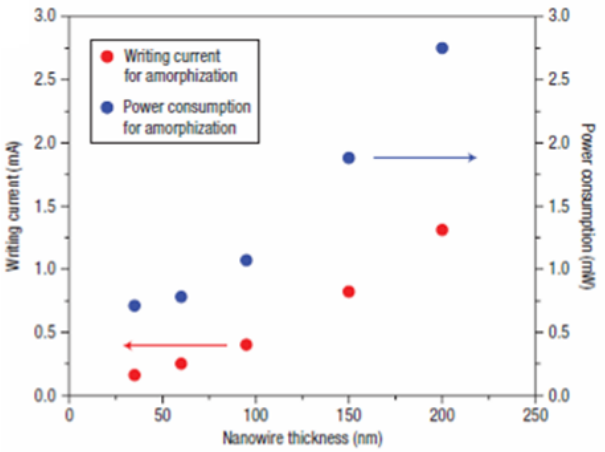

Figure 33: the writing current and the power consumption required for the amorphization of a GST NW as a function of the NW thickness.

4.2 NWs Growth and electrical characterization.

The samples studied in this work are (Ge)-Sb-Te, with different stoichiometry and Ge content, grown on an oxidized Silicon substrate, with a 50 nm thick SiO_2 layer.

The growth technique employed is called Metal Organic Chemical Vapor Deposition (MOCVD) and the samples have been grown by Dr. Massimo Longo at the MDM Laboratory of CNR-IMM, Agrate Brianza.

The growth of one-dimensional nanostructures with vapor phase deposition is achieved by the VLS (Vapor-Liquid-Solid) mechanism [24]. The growth of a crystal for direct adsorption of a gaseous phase on a solid surface is generally slow. The VLS approach uses a metal seed particle in order to decompose a vapor-phase reactant into a semiconductor through a liquid eutectic alloy at high temperature. The catalyst metal is typically gold and is deposited before the growth of the wires. The eutectic droplet adsorbs the nutrients in the vapor phase and, when it is oversaturated, the growth takes place at the solid-liquid interface according the scheme in Figure 34a.

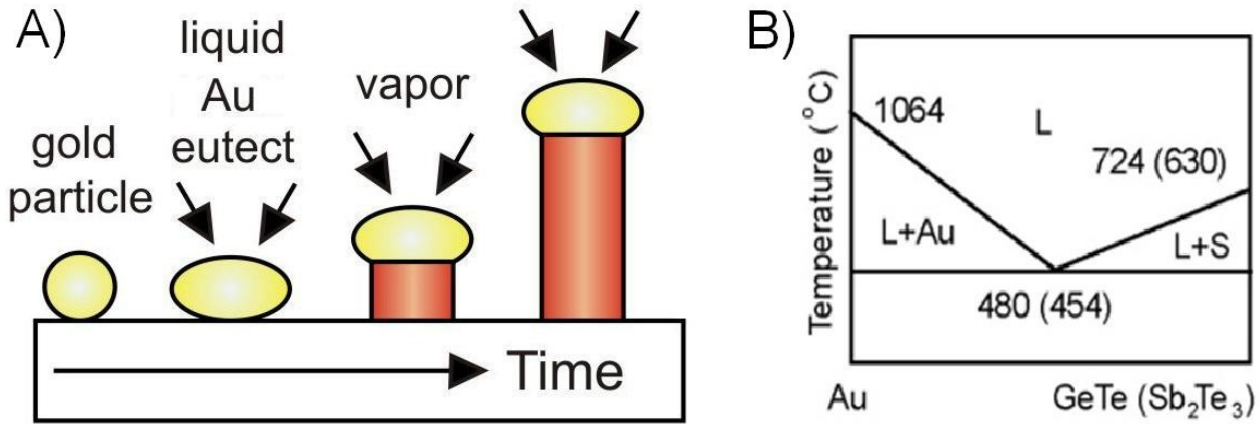

Figure 34: a) a graphical representation of the Au catalyzed VLS mechanism and **b)** the Au/GeTe and Au/Sb_2Te_3 binary phase diagrams **[25]**.

In Figure 34b) the binary phase diagram Au/GeTe and Au/SbTe are reported. The two diagrams are overlapped because they have the same shape. The temperatures in the bracket correspond to the Sb_2Te_3 while, those reported outside the bracket correspond to the GeTe.

In principle, the VLS growth is possible only at a temperature exceeding the eutectic point, however it is known that, for nanometric Au particles, the eutectic temperature may decrease and make VLS growth possible at lower temperatures [26].

The Au catalyst has been directly deposited onto the substrate via thermal evaporation. The partial coverage of the substrate leads to the formation of small nano islands and these islands acts as catalytic seeds during the growth.

The size of the Au islands therefore influences the morphology of the resulting NWs being the NWs diameter equal, but usually bigger, than the size of the catalyst.

The typical appearance of the substrate used for the NW growth is shown in the SEM image of Figure 35.

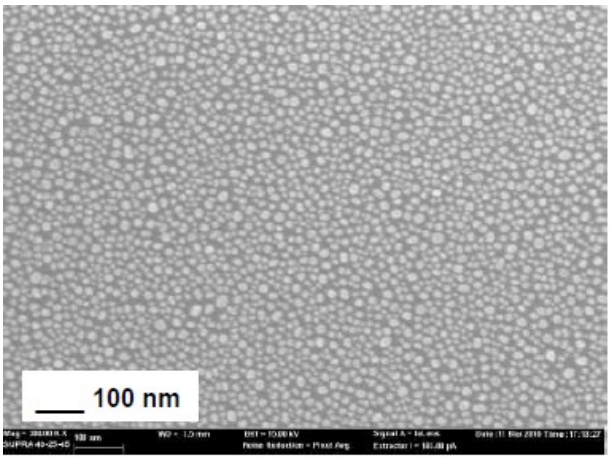

Figure 35: the substrate used for the growth of the NWs.

The average dimension of the Au nanoislands is 20 – 30 nm producing NWs whose diameter exceeds 40 nm.

The nutrient phase is composed by a mixture of gases: N_2 acts as a carrier and process gas for the reagents, reported in Figure 36, that are the tetrakisdimethylaminogermanium ($[N(CH_3)_2]_4Ge$, TDMAGe), the trisdimethylaminoantimony ($[N(CH_3)_2]_3Sb$, TDMASb) and the diisopropyltelluride ($(C_3H_7)_3Te$, DiPTe), which are used as Ge, Sb and Te precursors, respectively.

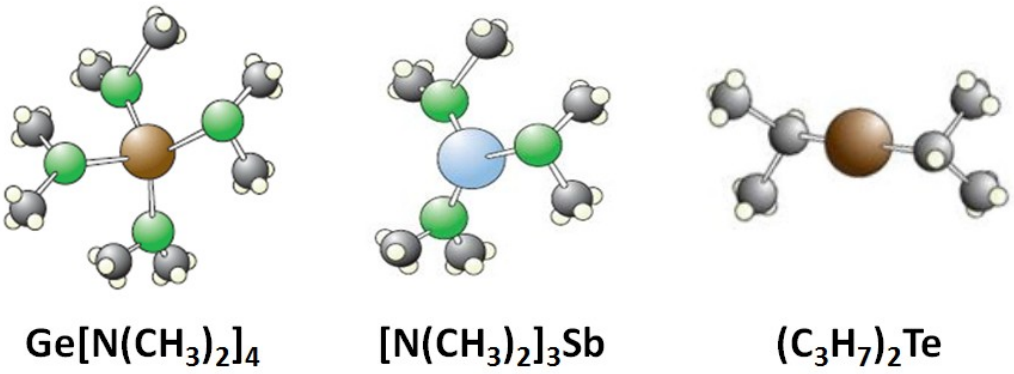

Figure 36: formulas of the precursors used in this work.

The stoichiometry of the resulting NWs can be changed by changing the partial pressure of the precursors.

In particular, many compounds on the GeTe-Sb_2Te_3 tie line have been investigated by changing the Ge content in the range of 0-22%: pure and Ge-doped Sb_2Te_3 [27], $Ge_1Sb_2Te_4$ and $Ge_2Sb_2Te_5$[28].

The phase change behavior of our NWs has always been assessed after the growth. The electrical characterization of single NWs requires the deposition of Pt electrodes on both NW ends, employing focused ion beam (FIB). The NW phase change was observed through pulsed current/voltage (I/V) measurements performed by an Agilent Pulse Generator 81110 to supply the voltage pulses.

As an example, the results obtained on a $Ge_1Sb_2Te_4$ NW are reported in Figure 37. The SEM image of a 1 µm long and 80 nm thick NW after electrode preparation is shown in a).

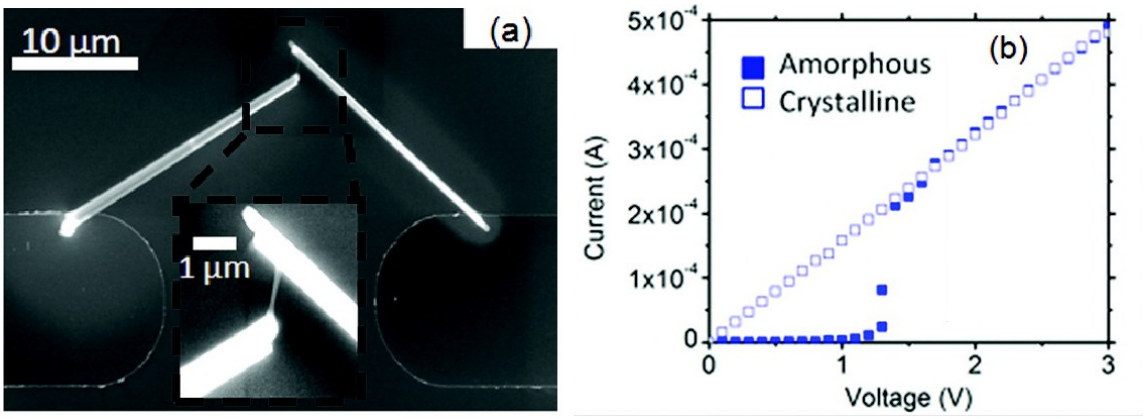

Figure 37: a) SEM image of a $Ge_1Sb_2Te_4$ NW, contacted by FIB; the NW area is visible in the enlargement. **b)** Pulsed I/V measurement of the device in a) (full squares for amorphous GST, open squares for crystalline GST).

The pulsed I/V plot obtained from the same NW is shown in b). The as grown $Ge_1Sb_2Te_4$ NW is in the low resistance state (~6 kΩ) and exhibits a linear I/V characteristic (open squares). Amorphization of the NW was achieved by supplying 3 V, 300 ns voltage pulse; in this state, the resistance increased to 450 ± 50 kΩ, corresponding to about a 2 orders of magnitude programming window. Pulsed I/V of the amorphized NW displays threshold switching at around V_{th} =1.35 V (full squares). The two curves are in perfect agreement with the expected behavior already described in Figure 32.

4.3 Crystal structure of the chalcogenide alloys

The ternary Ge-Sb-Te compounds have two crystalline polymorphs, namely, a ground-state phase and a metastable phase with slightly higher formation energy.

The metastable phase crystallizes in a cubic rocksalt-type (RS-type) structure, in which the Te atoms occupy the anion sites, whereas the Ge, Sb, and intrinsic vacancies randomly occupy the cation sites[29][30][31], as shown in Figure 38a.

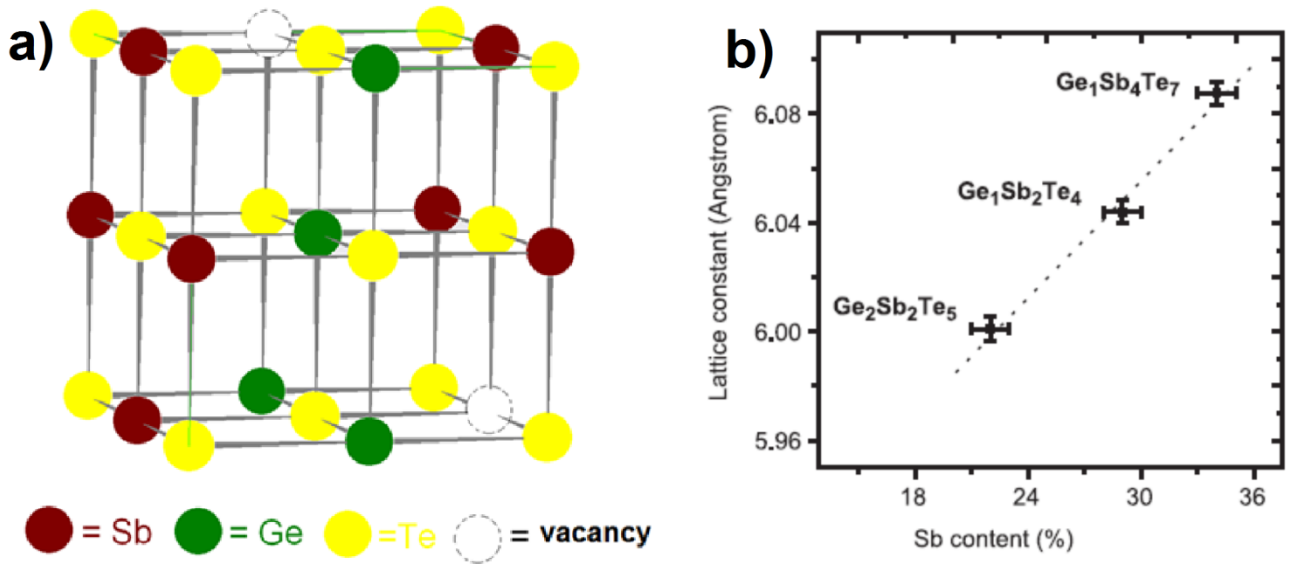

Figure 38: a) the crystal structure of the GST metastable cubic phase. **b)** dependency of the lattice constant on the Sb content.

The lattice parameter is slightly different for the various compounds and linearly depends on the Sb content as shown in Figure 38b.

The binary compound Sb_2Te_3 has the stable phase only. It crystallizes in a rhombohedral layered structure with space group *R*-3*m* composed by three building blocks, as shown in Figure 39a. Each building block, marked by the red dashed lines, consists of five atomic planes stacked along the (0001) direction of the conventional hexagonal lattice, in the sequence -Te-Sb-Te-Te-Sb-, according to the *a,b,c* close packed stacking.

Because the *a*,*b*,*c* stacking requires that the number of planes along the *c*-axis, within the unit cell, is always a multiple of 3, principle known as the *3n+3 rule,* the unit cell contains three building blocks, for a total of 15 atomic planes. The resulting c-axis length is c=3.045 nm. [32]

The interplane distance is ≈0.18 nm with the exception of the distance between the two consecutive Te planes that is about 0.3 nm, being these planes connected by weak van der Waals interactions instead of strong covalent bonds. This creates a gap between two neighboring blocks called van der Waals gap, highlighted with the black circle. The length of each building block is c/3=1.015 nm.

The structures of the stable phase of the other stoichiometric compounds along the binary tie line have strong similarities with the Sb_2Te_3 structure already described.

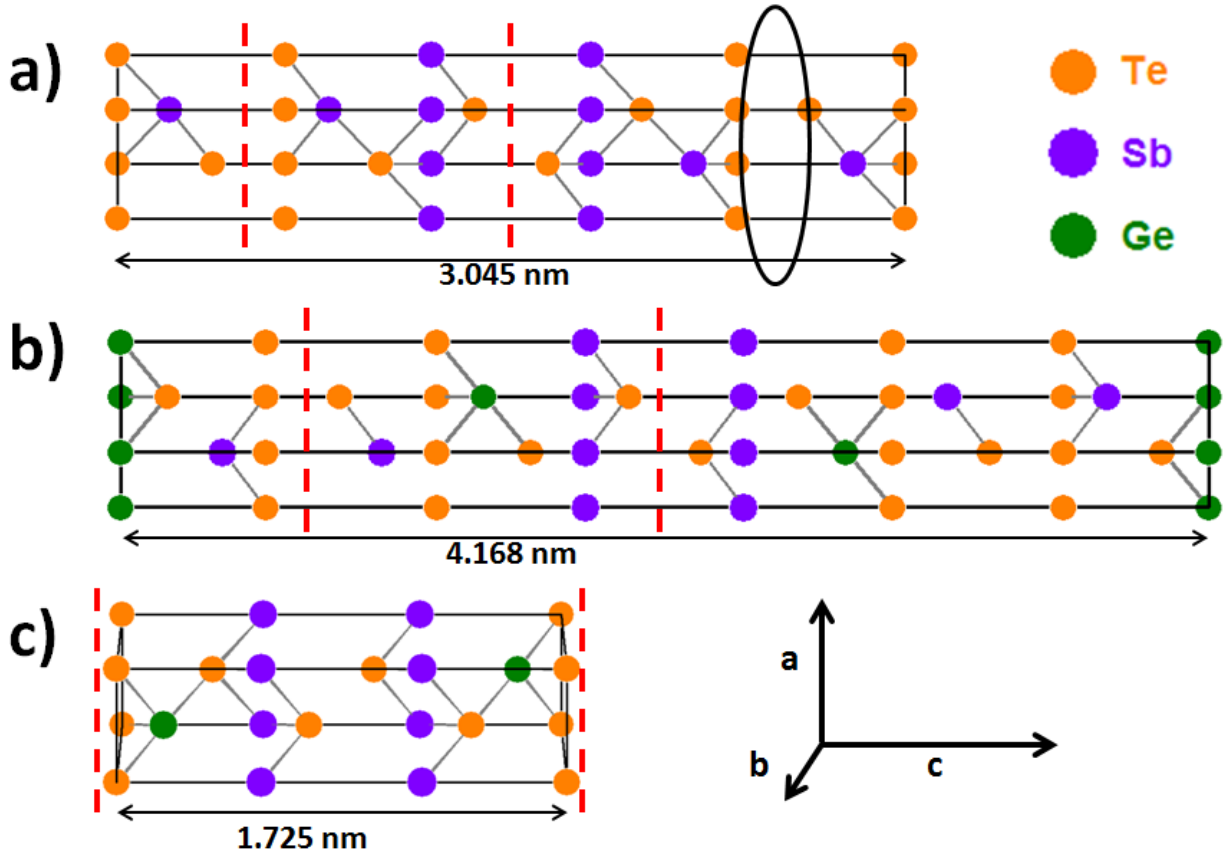

Figure 39: the crystal structure of the stable hexagonal phase of the **a)** Sb_2Te_3, **b)** $Ge_1Sb_2Te_4$ and **c)** $Ge_2Sb_2Te_5$ compounds. The red dashed lines mark the building block composing the unit cell. The black circle highlights the van der Waals gap.

The structure of the $Ge_1Sb_2Te_4$ stable phase can be described as the formal insertion of a GeTe bilayer, see Figure 39b. The building block now contains 7 atomic planes and is 1.39 nm long [33].

According the *3n+3 rule,* in this case also 3 building blocks are needed to obtain a hexagonal stacking. The unit cell therefore contains 21 atomic planes and c=4.168 nm.

With the insertion of a second GeTe bilayer the $Ge_2Sb_2Te_5$ is formed. In this case the building block contains 9 atomic planes and the *3n+3 rule* is automatically satisfied, hence the building block coincides with the unit cell. The c-axis length is 1.725 nm [34]. The crystal structures details stable compounds are summarized in Table 2.

Compound	Space Group	Atomic planes	a (nm)	c (nm)
Sb2Te3	R-3m	5	0.421	3.045
$Ge_1Sb_2Te_4$	R-3m	7	0.427	4.168
$Ge_2Sb_2Te_5$	P-3m1	9	0.425	1.725

Table 2: summary of the crystal structures described in Figure 39.

Being the c-axis length distinctive of each phase its measurement allows to identify which phase is present in the sample. This method has been used in the following sections and proved to be very reliable.

4.4 Effect of Ge-doping on the Sb_2Te_3 NWs

As it has been mentioned in the previous chapter, the structures of the stable phases on the binary phase diagram can be described as GeTe bilayers inserted in the structure of the Sb_2Te_3 compound. Therefore each phase has a characteristic, different Ge content. Conversely we can say that the introduction of Ge in the Sb_2Te_3 changes its structural properties and turns it into the other compounds.

The stoichiometry affects not only the structure but also other properties that are crucial for the final device. In particular a strong correlation between the Ge content and the melting temperature is observed.

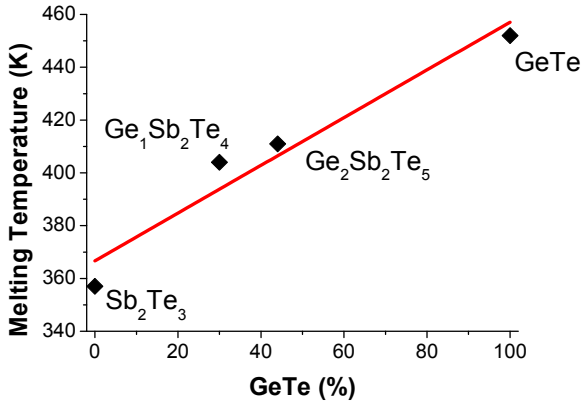

Figure 40: the melting temperature as a function of the GeTe content.

In Figure 40 it is shown that the melting temperature, reported as a function of the GeTe content, linearly increases with the increasing GeTe content, ranging between the 360K (pure Sb_2Te_3) to the 460K (pure GeTe) [35].

The melting temperature is a key parameter for PCM devices: lowering the melting point means a reduced energy consumption required to melt the active region in the memory cell and, at the same time, a higher programming speed. Conversely, for high power/high temperature applications (automotive) high crystallization temperatures are needed to ensure the correct functioning of the device.

Growing non stoichiometric material, for example by doping with Ge during the growth, can open the way toward a fine tuning of the properties of the PCM. In this framework, Ge doped SbTe, with a 10% Ge concentration and a low Sb/Te ratio has been recently reported to provide a high speed and a low power memory device [36].

Following this idea, Ge-doped SbTe NWs have been analyzed in order to explore the possibility to grow defect free material. In particular it has been quantified how much Ge can be incorporated in the NWs before introducing remarkable modification in the lattice, and the way it affects the crystal structure.

It was found that the NWs having a Ge content in the 0-5% range retain the Sb_2Te_3 crystal structure, illustrated in Figure 39a, and can be grown without introducing defects.

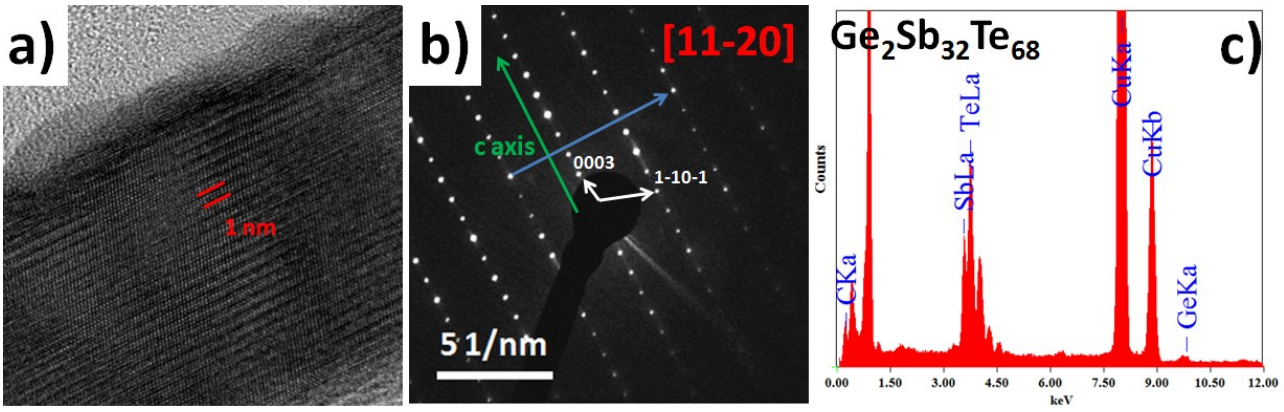

Figure 41: a) HREM image of a [11-20] oriented NW and **b)** its electron diffraction DP. The NW possesses the Sb_2Te_3 structure as it can be identified by the c axis length highlighted in a) and from the study of the DP (see text). The EDX spectrum in **c)** confirms the phase identification**.**

In Figure 41a the HREM image of a NW, oriented along the [11-20] zone axis, with a very low Ge content is shown. The chemical composition is evaluated from the EDX spectrum shown in c). The spectrum has been recorded while illuminating a large part of the sample in order to maximize the signal. In the spectrum, the *Sb* (Lα) and *Te* (Lα) characteristic lines are clearly evident while the *Ge* characteristic line is barely visible. The total composition, evaluated by the analysis software, is reported on the spectrum and reveals a *Ge* composition of about 2%.

In the spectrum, the lines corresponding to the *C* and *Cu* characteristic X-rays, also appear. These two signals come from the carbon coated copper grid supporting the sample and are always present in the XRD spectra. Anyway, they do not affect the quantitative analysis.

It also worth noticing that the Sb and the Te characteristics lines are very close each other, partially overlapping. This happens because the atoms are very close on the periodic table and have similar properties. The vicinity of the lines hampers the chemical quantification and so, even if the Sb/Te ratio is not 2/3, the stoichiometry can still be compatible with the Sb_2Te_3 compound.

In the HREM picture in Figure 41 a) the lattice fringes corresponding to the c-axis are highlighted by the red markers. The spacing between the fringes is about 1nm. According to the unit cell description summarized in Table 2 it corresponds to the c/3 spacing of the Sb_2Te_3. This information confirms the chemical analysis obtained from the EDX spectrum.

The analysis of the DP reported in Figure 41 b) reveals other features of the crystal structure further confirming the phase identification. The two main frequencies in the DP have measured and indexed as the (0003) and the (1-10-1) reflections, according the labels in the picture. In the (1-100) direction, namely the direction orthogonal to the c-axis, indicated by the blue arrow, a 3 fold super periodicity can be observed. As a matter of fact, there is only one diffraction spot on the blue line every three rows. This periodicity comes from the selection rules typical of the space group of the Sb_2Te_3, see Table 2. The selection rules is due to the *3n+3 rule* which implies that only the reflections with $-h + k + l = 3n$, with n being an integer, are allowed.

To conclude, when the Ge content is not exceeding the 5%, it is completely incorporated in the Sb_2Te_3 lattice without affecting the NWs structure.

When the Ge concentration increases things drastically change. The atomic structure of the NWs with Ge content exceeding 5% was found to depend on the incorporated *Ge* amount itself.

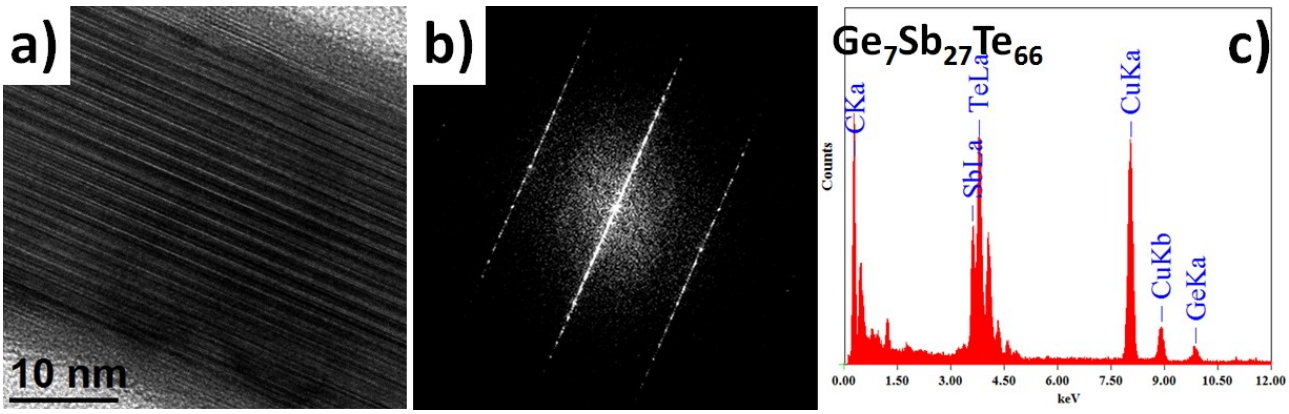

Figure 42: a) HREM image and **b)** diffraction DP of a NW having a 7% Ge content as shown in the EDX spectrum in **c).**

Figure 42a shows the HERM image of a NW containing 7% of *Ge* as testified by the EDX spectrum of Figure 42c acquired on the same wire, showing the result of the chemical analysis. Both this spectrum and the spectrum in Figure 41 c) have been normalized to the maximum value of Te Lα line. In this way the height of the Ge line is directly related to the composition.

The lattice fringes in the HREM image are not well defined if compared to those studied in the previous case. In some cases they seem to change their spacing going through the wire. It is difficult to give a value of the lattice spacing. Also, the spots in the FFT reported in Figure 42b, are not well defined and are elongated in the c-axis direction forming an almost continuous line.

The streaking, namely the elongation of the spots in the FFT, is caused by the presence of disorder in the imaged atomic structure and so we can conclude that what is displayed in Figure 42 a) is a disordered structure.

When the Ge content increases it can no longer be incorporated in the Sb_2Te_3 structure without distorting it. The random insertion of GeTe units in the Sb_2Te_3 slabs locally changes the stoichiometry of the wires and therefore the c-axis length. In some cases, this could result in forming embedded $Ge_1Sb_2Te_4$ units in the surrounding Sb_2Te_3 matrix, as shown in the high resolution HAADF image reported in Figure 43.

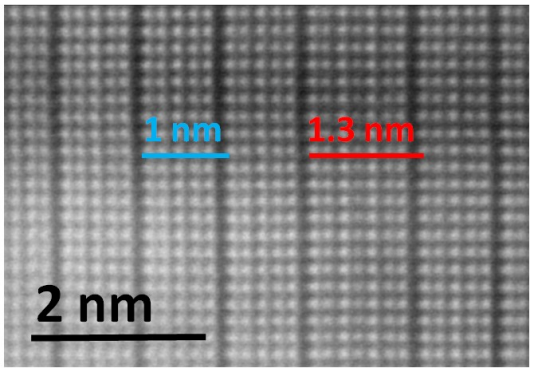

Figure 43: High resolution STEM-HAADF image of a NW presenting a mixed crystal structure. In the image a SB_2Te_3 (blue) and a $Ge_1Sb_2Te_4$ (red) segments are highlighted.

The van der Waals gaps appear as dark lines in the Z-contrast image and are used as references to measure the c-axis of the unit cell. The 1 nm periodicity, highlighted with the blue marker, corresponds to the Sb_2Te_3 slabs. Each slab contains 5 atomic planes as expected. Embedded in the Sb_2Te_3 matrix a single $Ge_1Sb_2Te_4$ slab is present, highlighted by the red marker, containing 7 atoms. Indeed, with Ge contents ranging from 5% to 13%, the NWs were found to have a completely disordered structure, showing random stacking of slabs with different stoichiometry. It is possible to obtain an image with such a clear contrast on a very thin part of the NW. When the NW

becomes thicker, the imaging process is impossible because the disorder is also extended in the in depth direction and produces the overlapping of NW segments with different crystal structure. This disorder is responsible for the spot streaking in the FFT.

Since the $Ge_1Sb_2Te_4$ phase contains 14% Ge, the Ge content ranging from 5% to 13% is too low to stabilize the $Ge_1Sb_2Te_4$ phase and, at the same time, it is too high for being incorporated into the Sb_2Te_3 phase as a dopant. Therefore NWs with such Ge content exhibit a disordered structure.

Only when the Ge content is above the 13% a perfect $Ge_1Sb_2Te_4$ structure can be found.

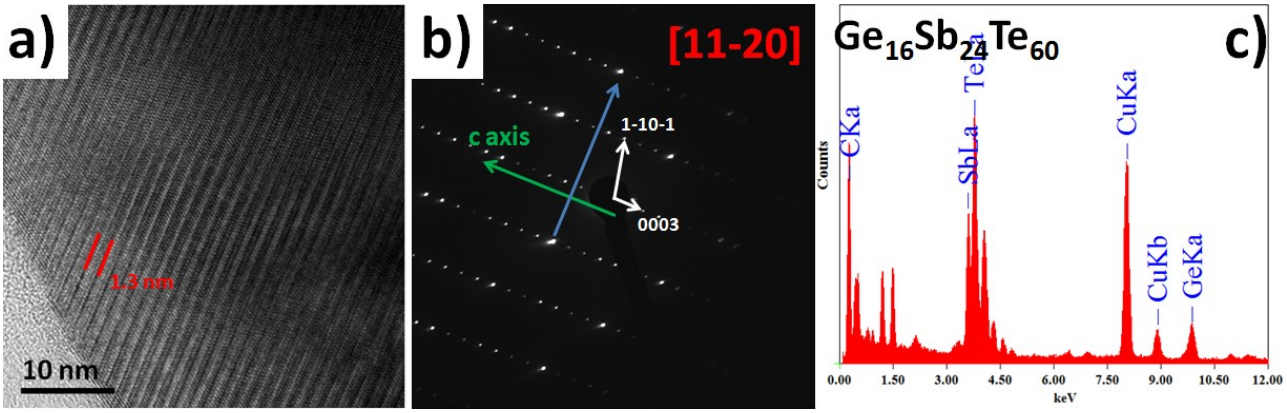

Figure 44: a) HREM image of a [11-20] oriented NW and **b)** its electron diffraction DP. The NW possesses the $Ge_1Sb_2Te_4$ structure as it can be identified by the c axis length in a) and from the study of the DP (see text). The EDX spectrum in **c**) confirms the phase identification.

In Figure 44 a) the HREM image of a NW exhibiting the $Ge_1Sb_2Te_4$ structure is shown. Along the c-axis a very clear 1.3 nm spacing can be easily measured confirming the phase identification and the good crystalline quality of the NW. According to the EDX spectrum in Figure 44 c) the Ge content is higher than 13%, the minimum required to stabilize the $Ge_1Sb_2Te_4$ structure.

In Figure 44 b) the DP of the wire depicted in a) is shown. It has been indexed following the same procedure previously exposed. Because the $Ge_1Sb_2Te_4$ structure belongs to the same space group of the Sb_2Te_3, the same selection rules observed in Figure 41 are expected.

Again the blue line runs orthogonally to the c axis and can be used to show the three-fold super periodicity produced by the selection rules.

Also, along the c-axis direction an intensity modulation is present. This modulation has a periodicity of 7 diffraction spots. This modulation is also expected because, recalling the

description given in Figure 39 and in Table 2, 7 atomic planes are stacked along the c-axis in the $Ge_1Sb_2Te_4$ structure.

All these observations confirm that, when a sufficiently high Ge concentration is incorporated, the NWs assume the perfect $Ge_1Sb_2Te_4$ structure.

To conclude this section and summarize the exposed results, the optimization of the growth parameters led to the formation of both pure defect free Sb_2Te_3 and Ge doped SbTe phase change single crystal nanowires. The results also show the structure and the composition gradually change from pure Sb_2Te_3 NWs to stoichiometric $Ge_1Sb_2Te_4$ NWs passing through a mixed state having a disordered structure.

Combining different imaging techniques, such as HRTEM and Z-contrast STEM, and diffractive techniques, like electron diffraction, the structure of all the growth products has been fully characterized. This work, even though preliminary, offers the back ground needed for a future understanding of the properties of the Ge-doped SbTe NWs for phase change memory application.

4.5 Crystal structure assessment of Ge-Sb-Te NWs

As already mentioned, chalcogenide ternary $(GeTe)_m(Sb_2Te_3)_n$ compounds are among the best active materials for the phase change memories, one of the most mature candidates for the future standard nonvolatile memory devices. The understanding of the phase transition mechanism, as well as a deeper knowledge of the structure of the phases involved in the transition, is an essential requirement for a successful downscale.

To this aim, many studies have been published in the last years, proposing numerous different atomic arrangements either for the amorphous [37][38][33] or crystalline phases of the possible GST compounds, some of them already reported in Figure 39.

However, despite the considerable amount of work, while the space groups are quite well assessed, the atomic arrangement of bulk crystalline GST compounds is still subject of a debate in the literature [39][40]. In particular, given the large number of atoms in the unit cell, there is indetermination of the Ge and Sb atom positions, even though they have more profound effects on the optical and electronic properties than the crystal structure itself [41].

Therefore, even though the GST compounds are currently used in rewritable technological applications, the knowledge and understanding of their atomic structure are far from satisfactory.

In this chapter a method based on the comparison of HAADF-STEM images and proper simulations is proposed. The method is also successfully used to determine the atomic arrangement of $Ge_1Sb_2Te_4$ and $Ge_2Sb_2Te_5$ compounds allowing, for the first time, the identification of the exact stacking sequence in GST NWs.

4.5.1 $Ge_1Sb_2Te_4$ NWs

In the following the result obtained on the $Ge_1Sb_2Te_4$ compound are reported.

According to the literature, in its stable phase, the $Ge_1Sb_2Te_4$ compound shows a rhombohedral crystal structure, space group R-3m, with lattice parameters a=0.424nm and c=4.161nm consisting in the stacking of 21 atomic planes, as already reported in Figure 39.

However the exact stacking sequence is still under debate with many different proposed ones found in the literature.

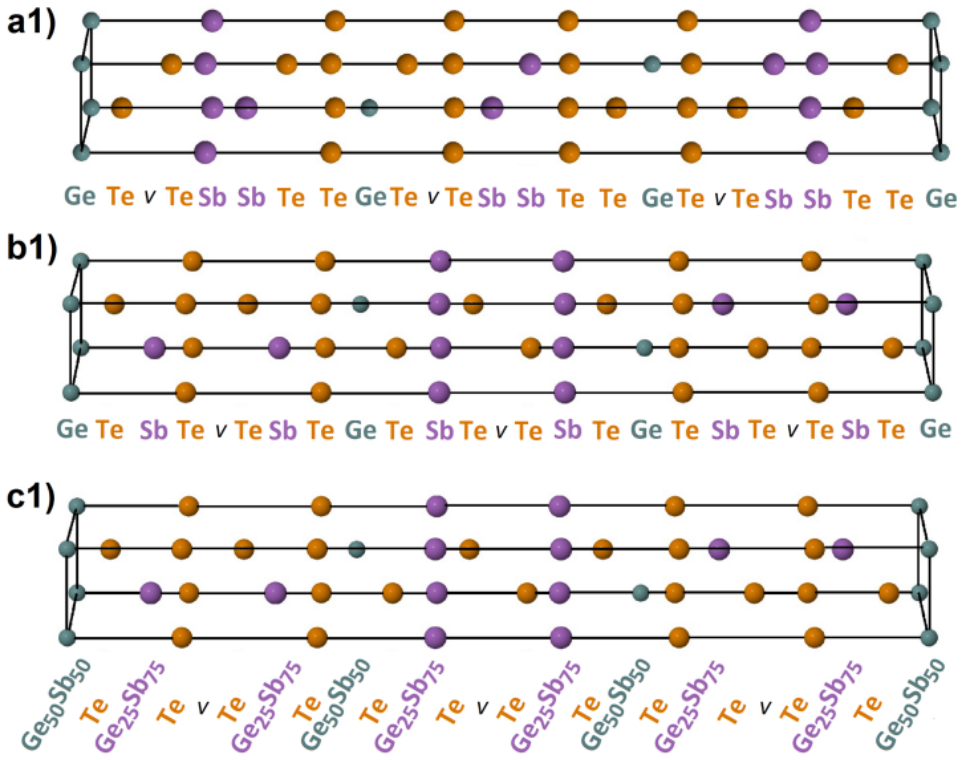

Figure 45: The layer sequences in the hexagonal $Ge_1Sb_2Te_4$ phase according to the models proposed by Agaev and Talibov **(a1),** Sun et al. **(b1)** and Matsunaga and Yamada **(c1).**

In Figure 45 the three stacking sequences, chosen to be simulated and compared with our experimental data, are shown. They represent the models proposed in references [42], [33][34], which are compatible with the R-3m symmetry, appearing this a solid experimental fact.

The structure labeled a1) was originally proposed by Agaev and Talibov [34] back in 1966. In this structure each atomic species occupies a different lattice site and the resulting stacking sequence is *Ge-Te-Te-Sb-Sb-Te-Te-Ge-Te-Te-Sb-Sb-Te-Te-Ge-Te-Te-Sb-Sb-Te-Te-Ge.*

In a more recent work Sun *et al.* [42] have investigated all the possible ordered stacking sequences by *ab initio* DFT calculations, finding out that the structure labeled b1) has the lowest cohesive energy and it is the most stable configuration among the structures they have analyzed. The 21 atoms are here organized in three forming units, each containing 7 atomic planes, with stacking sequence *Te-Ge-Te-Sb-Te-v-Te-Sb-*. *v* represents an ordered layer of vacancies that corresponds to the van der Waals gap between the two consecutive Te planes, naturally present in the Sb_2Te_3 structure [32]. As a matter of fact, according to another way of depicting the unit cell formation,

all the compounds in the homologous series $(GeTe)_m$ $(Sb_2Te_3)_n$ can be described with the formal insertion of GeTe units into Sb_2Te_3 slabs [43]. Sun *et al.* completely neglect the possibility of random occupation of the same site by Ge and Sb. This assumption seems to be reasonable as, in a similar study [44], a structure formation mechanism is proposed that does not allow for random partial occupation.

Despite these theoretical results, a structure with Ge and Sb sharing the same lattice sites has been refined by x-ray powder diffraction using synchrotron radiation facilities, [33] that we report in figure 1 labeled as c1). It is quite similar to the structure b1), with 3 forming units containing 7 atomic planes each but, in some planes, Ge and Sb atoms are mixed together in the rates reported in the figure.

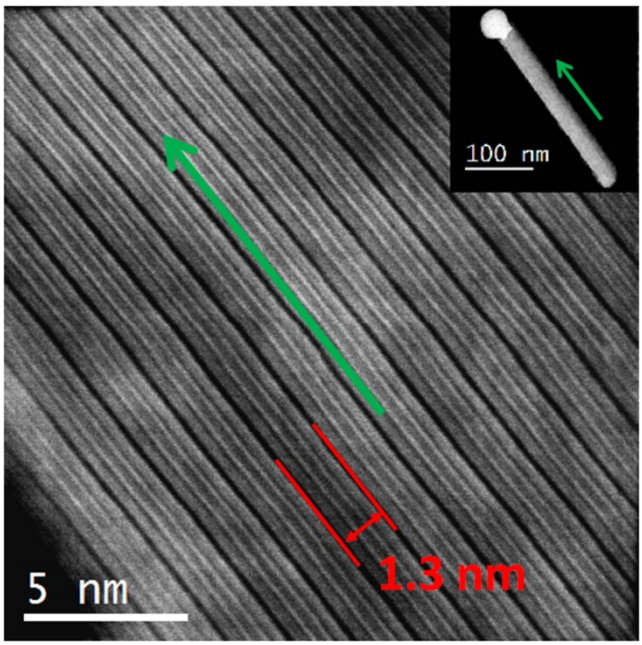

Figure 46: High resolution HAADF-STEM image of the $Ge_1Sb_2Te_4$ NW, reported in the inset, in the [10–10] projection. The period is 1.39 nm, corresponding to the distance between the van der Waals gaps in $Ge_1Sb_2Te_4$. The green arrows represent the growth direction of the NW.

An experimental HAADF image of a 500 nm long $Ge_1Sb_2Te_4$ NW is presented in Figure 46. A low magnification image of the whole wire is reported as inset. The bright particle on the top of the wire is the Au catalyst seed. The NWs composition has been assessed by EDX as reported in the previous section.

The equally spaced darkest lines correspond to the van der Waals gaps: the distance between them is 1.39 nm, consistently with the lattice parameters of the $Ge_1Sb_2Te_4$ phase given above.

The lattice planes orthogonal to the c-axis, although their 0.21 nm spacing could be resolved by the microscope, are not visible, possibly due to the poor signal-to-noise ratio (S/N) in combination with the not perfect zone axis condition. Both these conditions can be easily met because GST is especially sensitive to electron beam damage, which imposes very fast image acquisition exposure and alignment procedures to avoid any possible atom rearrangement under the beam.
Nevertheless it has been proven that these conditions do not affect the result [45].
In Figure 47, a magnified detail of the experimental image in Figure 46, together with the image simulation performed using the structures proposed by Sun (a1), Agaev (b1) and Matsunaga (c1) are reported on the left side; the corresponding image intensity line profiles are shown on the right side. The simulations have been performed according the linear approximation exposed in equation 2.24.
The images are aligned along the van der Waals gaps, inside which the different stacking of atomic planes results in strong differences of the contrast patterns among the images.
At a first glance it can be seen how the structure a1) does not fit the experimental contrast and can be excluded.

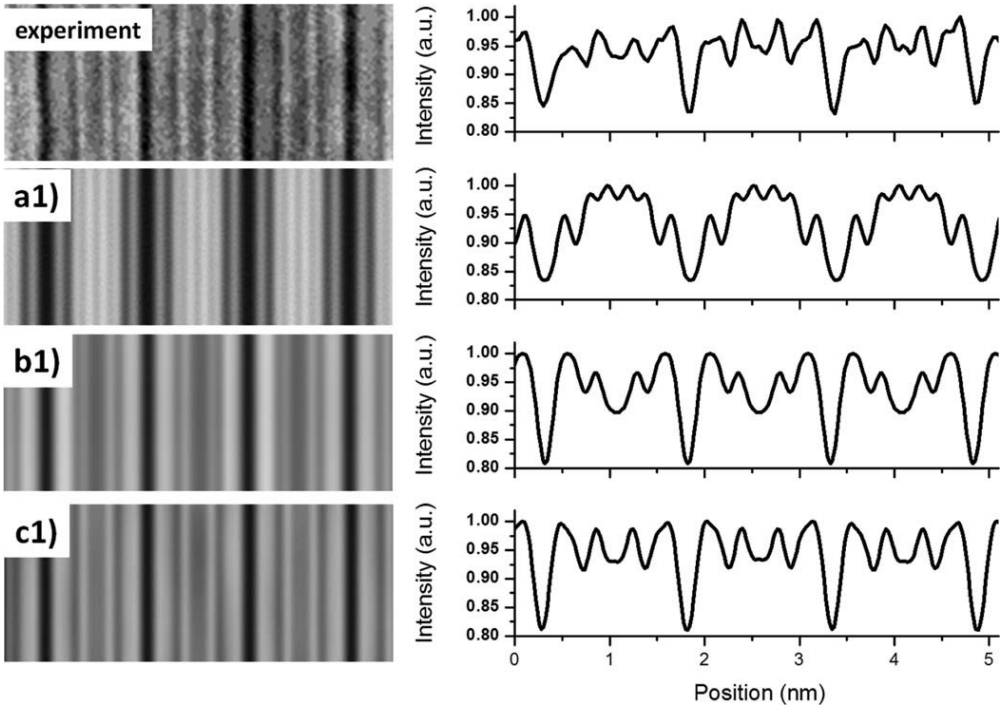

Figure 47: The simulation results: on the left side of the panel there are the experimental and the simulated images of the cell structures in Figure 45 with the same labels. On the right side, are the corresponding intensity line profiles.

The structure b1) and c1) look similar and both of them have similarities with the experiment. The main difference between the two is the chemical composition of the central plane in the slab: in the structure labeled as b1) the central plane contains Ge only and produces a darker contrast in the simulation, while in the structure c1) there is only 25% of Ge producing a brighter contrast.

The contrast observed in the experiment better matches the contrast produced by the c1) structure.

Even though the simulated patterns are characteristic for each sequence and can be easily recognized in the experimental images, the cross-correlation coefficients between the image of each simulated structure and the experimental one have been calculated.

In particular, we used the scale-free cross-correlation calculation proposed by Thust and Urban [46] which simplifies the matching procedure because it is independent on any scale factor and background typically present in the experimental images.

The cross correlation coefficient is calculated according to the formula:

$$C_{cor} = \frac{\sum_{x} \left(f_{\exp} - \bar{f}_{\exp}\right)\left(f_{sim} - \bar{f}_{sim}\right)}{\sigma_{\exp}\sigma_{sim}} \qquad (4.1)$$

Where $f_{\exp}$ and f_{sim} are the experimental and simulated profiles, $\bar{f}_{\exp}$, $\bar{f}_{sim}$, $\sigma_{\exp}$, σ_{sim}, are the average value and standard deviation. This coefficient is in the range [0,1] where 1 means that the two curves coincide.

The calculated cross correlation coefficients are summarized in Table 3.

	Agaev	Sun	Matsunaga
$\mathbf{C_{cor}}$	0.636	0.761	0.893

Table 3: Calculated cross-correlation coefficients between the experimental and the simulated images of the three stacking sequences in Figure 45.

The structure proposed by Matsunaga best fits the experimental contrast, with a cross-correlation coefficient close to 90%. The major difference between the experimental and the simulated images is located close to the vacancy layer: in the experimental one, the first peak on the right side of each dark line has a lower intensity than the symmetric peak on the left. Since the two

peaks are related to the Te planes, and no chemical contrast is expected, the difference is probably due to a slight misalignment of the wire under the electron beam. We can therefore assess that the analyzed nanowires possess Matsunaga's structure; it is worth noting that such a structure prefigures random partial occupation in opposition to the theoretical results obtained in ref. [42] and [44] that rule out this possibility.

4.5.2 $Ge_2Sb_2Te_5$ NWs

The method has also been applied to the $Ge_2Sb_2Te_5$ as reported in the following.

The $Ge_2Sb_2Te_5$ compound in its ground state also shows a rhombohedral crystal structure, space group P-3m1, with lattice parameters a = 4.22nm and c = 1.72nm [47], consisting of 9 atomic planes stacked along the (0001) direction.

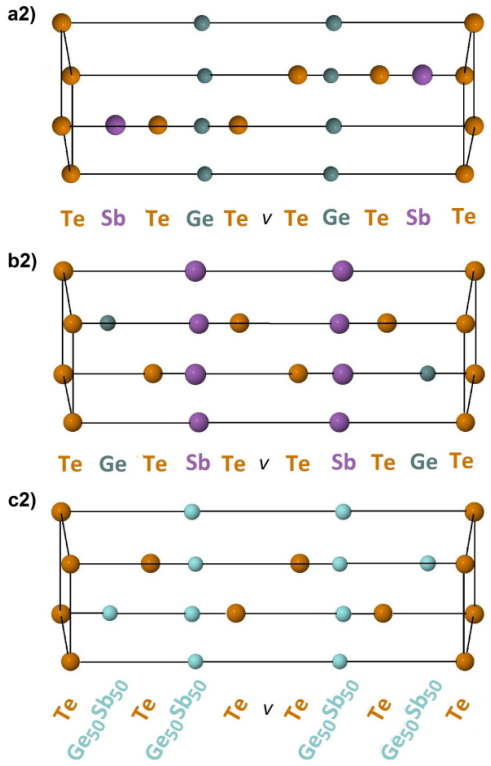

Figure 48: the layer sequences in hexagonal $Ge_2Sb_2Te_5$ phase according to the models proposed by Petrov *et al.* **(a2)**, Kooi and De Hosson **(b2)** and Matsunaga **(c2).**

As for the case of $Ge_1Sb_2Te_4$, the exact stacking sequence has not yet been assessed and many authors have proposed different candidate structures. Once again, we chose among these structures the three most commonly used and cited. They are reported in Figure 48 along with the atomic composition of each plane.

The structure labeled as a2) is the first reported in the literature and was proposed by Petrov *et al.* [48] in 1968. In this structure, each atomic species occupies a different lattice site and the resulting stacking sequence is *Te-Sb-Te-Ge-Te-v-Te-Ge-Te-Sb-.* As for the $Ge_1Sb_2Te_4$ structures, *v* represents the ordered vacancy layer. This structure well accounts for some experimental measurements like the absorption coefficient and the interatomic distances.[41]

The second structure we consider, labeled (b2), was proposed in 2002 by Kooi and De Hosson [49] by using electron diffraction and high-resolution electron microscopy results. It turns out to be the structure with the lowest formation energy [41],[50] and it is widely considered as the real cell structure. The stacking sequence is very similar to the previous one with the inversion of the Ge and Sb planes, the final stacking being: *Te–Ge–Te–Sb–Te–v–Te–Sb–Te–Ge–.*

Lastly, the third structure (c2) was proposed in 2004 (ref. [30]) by the same authors of the (c1) $Ge_1Sb_2Te_4$ structure and again shows disorder in Ge/Sb site occupation.

To identify the actual crystal structure of our $Ge_2Sb_2Te_5$ NWs, we followed the same procedure that was previously described.

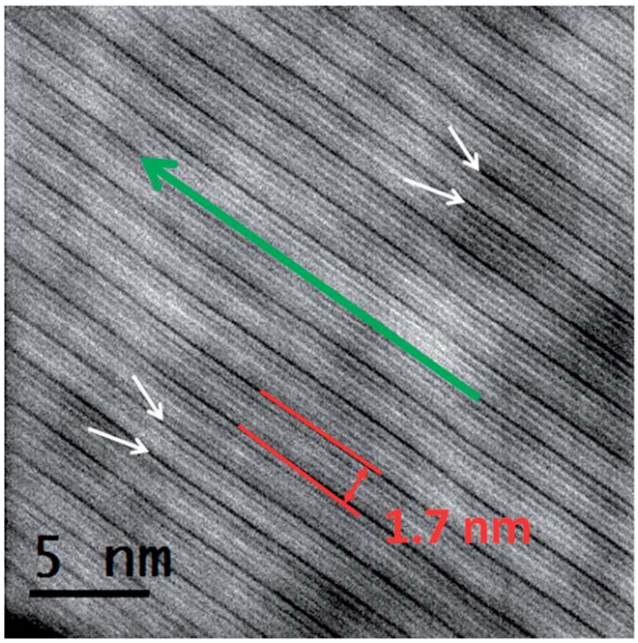

Figure 49: High resolution HAADF-STEM image of a $Ge_2Sb_2Te_5$ NW in the (10–10) projection. The period is 1.72 nm, corresponding to the $Ge_2Sb_2Te_5$ phase. The green arrow represents the growth direction of the NW.

The high resolution HAADF image of a portion of a $Ge_2Sb_2Te_5$ NW is reported in Figure 49. Again the darkest lines are due to the vacancy layers and their separation is ≈1.7 nm, in agreement with the above structure description. The white arrows indicate the presence of stacking defects running along the entire wire length. The distance between the vacancy layers and the contrast allows identifying these slabs with lower periodicity as insertions of $Ge_1Sb_2Te_4$ units in the $Ge_2Sb_2Te_5$ matrix in agreement with what exposed in the previous chapter.

The experimental image and simulated images according the three chosen structures are shown in Figure 50 where, from the top to the bottom, an enlargement of Figure 49 and the simulated images of the three structures are reported with their respective intensity line profiles. Again the four images have been aligned using as reference point the van der Waals gaps which appear as the darkest lines in the image.

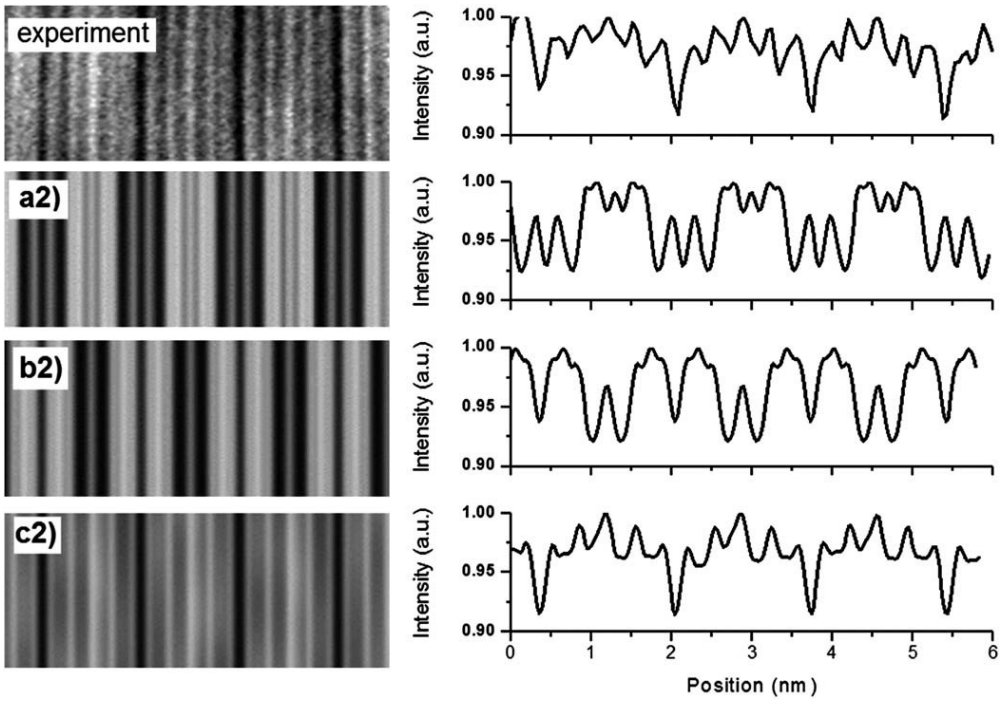

Figure 50: The simulation results: on the left side of the panel there are the experimental and the simulated images of the cell structures in Figure 48, according to the labels. On the right side there are the corresponding intensity line profiles.

The simulated intensity profiles related to the two ordered (a2) and (b2) structures are featured by a sequence of dark and bright lines, due to the ordered Ge and Sb planes, which are completely different from the pattern in the experimental image.

Only the structure (c2), allowing for random partial occupation of the Gs/Sb planes, correctly reproduces the details of the experimental image. This observation is expressed in a quantitative way by the cross correlation coefficients reported in Table 4.

	Petrov	Kooi	Matsunaga
C_{cor}	0.569	0.149	0.866

Table 4: Calculated cross-correlation coefficients between the experimental and the simulated images of the three stacking sequences in Figure 48.

For $Ge_2Sb_2Te_5$ NWs also, the structure with partial random occupation properly fits the experimental results with a cross correlation coefficient higher than 85%. We are led to affirm that all the observed NWs of both the GST compounds possess the structure proposed by Matsunaga, despite the available theoretical treatments predict the lowest stability for the mixed site occupation.

This result is not entirely unexpected since it was known, from theoretical calculations, that the energy difference between the ordered and the random structures is very small and of the same order of magnitude of the free energy contribution due to the configurational entropy of the disordered phase [51]. In our case we think that the energy balance can turn in favor of this structure due to low size effects. Even though no studies are present in the literature about size effects on the crystal structure of GST NWs, this topic has been investigated for other compounds, mainly III-V and oxide semiconductors. In these materials, different from bulk or unexpected crystal phases have been observed for diameters well beyond 50 nm, [52],[53] that is the typical size of our wires.

To summarize, in this chapter a method is discussed to assess the actual atomic plane stacking sequence of Ge-Sb-Te nanowires by the comparison of high resolution HAADF-STEM images and simulations. The method is direct, gives reproducible results in any microscope, provided that the experimental conditions are fulfilled, and it is a powerful tool to investigate at the nanoscale the entire class of GeSbTe compounds. The relevant finding is that, in both $Ge_1Sb_2Te_4$ and $Ge_2Sb_2Te_5$ NWs, only the structures with Ge and Sb atoms randomly sharing the same lattice sites properly account for the experimental results, despite the adverse predictions of all the theoretical models elaborated for the bulk material.

4.6 A new polymorph of Ge-doped Sb-Te

In chapter 4.4 we have already seen that the amount of Ge introduced in the Sb_2Te_3 affects the crystal structure of the nanowires and, in turn, their properties, in particular how it tunes the melting temperature (Figure 40).

All the sample described so far have been grown using the evaporated Au nanoislands (Figure 35) but this kind of substrate only gives NWs with diameter above 40 nm. In the continuous attempt of reducing the NWs diameter, commercial 10 nm colloidal Au nanoparticles have been used as different catalyst, that made it possible to grow NWs having diameter smaller than 40.

In this section we investigate the size effects on the NWs crystal structure and morphology due to the use of the new catalyst.

As a matter of fact, when the NWs are grown using colloidal Au nanoparticles, and incorporating a small amount of Ge, a new structure is observed which is never been reported in the literature.

It was found that not only the structure is different, but the NWs morphology is also influenced by the Au catalyst type.

I will describe the morphology first: the NWs are composed by many segments that give them their peculiar zig-zag shape, reported in Figure 51 a) and b), where the HREM images of two different NWs are shown.

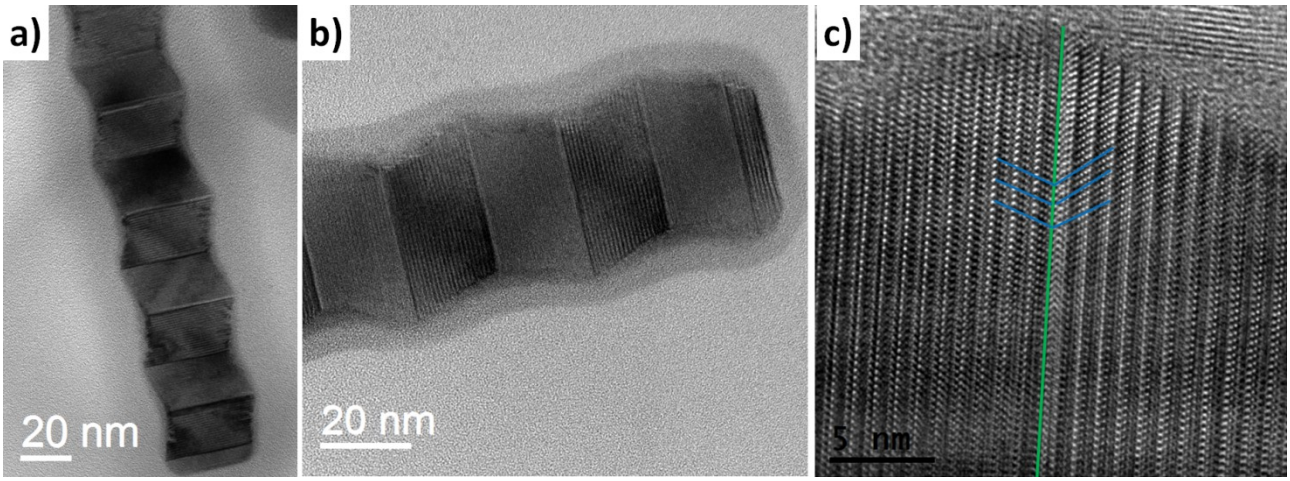

Figure 51: a) and **b**) TEM images of two different 3% Ge-doped Sb-Te zig-zag NWs. **c)** high magnification HREM image of a twin defect (green line).

The segments are always separated by twin defects as confirmed by the HREM image in Figure 51 c). The micrograph is taken near the sidewall of a NW and centered on the defect. The green line corresponds to the mirror plane. The blue lines are drawn parallel to the atomic planes in order to highlight the symmetry relationship between the two sides of the twin plane.

It is worth noting that the segment length L is uniform along the whole wire, usually several □m long, i.e. the twin defects are equally spaced and form a so called twin superlattice (TSL).

Most importantly, the TSL period depends on the wire volume in between the twins. The length of each segment and the diameter of the NW, L and D respectively in Figure 52a, are characteristic of each wire. Assuming that the wires have cylindrical shape, the volume of the segment is calculated and a characteristic volume is attributed to each NW.

The statistic of the recurrence of the characteristic volume in the sample is reported in Figure 52b.

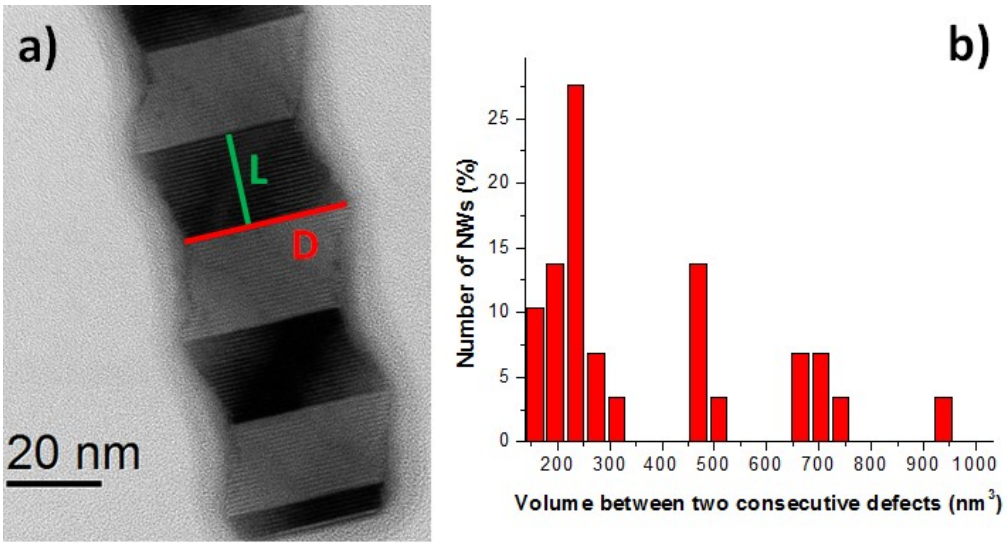

Figure 52: a) HREM image of a zig-zag NW. The period of the TSL and the diameter of the wire are highlighted. **b)** statistic of the recurrence of the characteristic volume in the sample.

The histogram shows a relatively narrow and "quantized" distribution of the segment volume. A first peak is centered around 240 nm^3 and the other peaks have are located at integer multiple of this "ground state" volume: 480 nm^3, 680 nm^3 and 940 nm^3.

TSLs have recently gained attention, especially in III-V semiconductors, because they allow tuning the NWs properties, in particular they have been predicted to introduce electronic miniband structures, which may be useful for bandgap engineering, as well as direct intersubband optical transitions. [54][55]

The phenomenology of the TSL formation has been well studied in system like GaAs [56], InP [57], InAs [58], GaP [59], SiC [60], but something similar has never been observed in chalcogenide NWs. Also, the mechanism leading to the formation of the TSL is not clear yet and two different models can be mainly found in the literature.

The first model well explains the TSL formation in III-V compounds. This class of material usually exists in two different polymorphs: a cubic zinc-blende structure and a hexagonal wurtzite one.

In cubic zinc-blende systems, a twin boundary along the (111) direction is consistent with the insertion of a single {001}-oriented wurtzite layer. The interface contains no dangling bonds and zero stress, therefore the formation energy of the twin boundary is very low.

During the growth the catalyst droplet tends to deform asymmetrically due to the faceting of the wire and the wetting angle changes consequently. Because the solid-liquid interface energy depends on the wetting angle, the deformation of the catalyst particle produces enough energy to induce the formation of the twin plane.[61]

The second model considers the accumulation of electrostatic charges during the growth. As a matter of fact, along the (111) direction of a zinc-blende semiconductor, the atomic bonds have both covalent and ionic character. For instance, in SiC, due to the difference of electronegativity between Si and C, some electrons would transfer from Si to C atoms. C atom carries negative charge as an anion and Si atom carries positive charge as a cation.

Therefore, in this system the electrostatic energy is a significant part of the total formation energy of the nano-wire. In particular, the accumulation of surface charge has been proved to lead to the periodical formation of twins.[62]

Anyway, both the models predict the TSL period to linearly increase with the NWs radius, and this behavior has actually been experimentally observed in zinc-blende III-V systems. In the present case no linear behavior is observed. Indeed, the TSL period is independent from the NW radius and a more complicated relationship is observed (Figure 52b).

The discrepancies with the models available in the literature are most likely due to the fact that these models have been developed for cubic systems, while Sb_2Te_3 has a hexagonal lattice. Further studies are ongoing to understand the TLS formation mechanism in Sb_2Te_3.

A deep investigation of the NWs crystal structure reveals other anomalies. We start our analysis with the study of the diffraction pattern of the wire in Figure 53. The long periodicity indexed as

the (0001) plane, parallel to the wire growth direction, is about 1 nm, consistently with the Sb_2Te_3 structure.

A second set of atomic planes, orthogonal to the first one is present, whose spacing is consistent with the (1-100) plane. Therefore the zone axis is indexed as the [11-20] one.

Anyway, the (1-100) reflection is forbidden and its intensity should be zero. If the diffraction pattern in Figure 53 is compared with the one reported in Figure 41, obtained in the same projection and already discussed, it can be noticed as the *h+k+l=3n* selection rule is not respected.

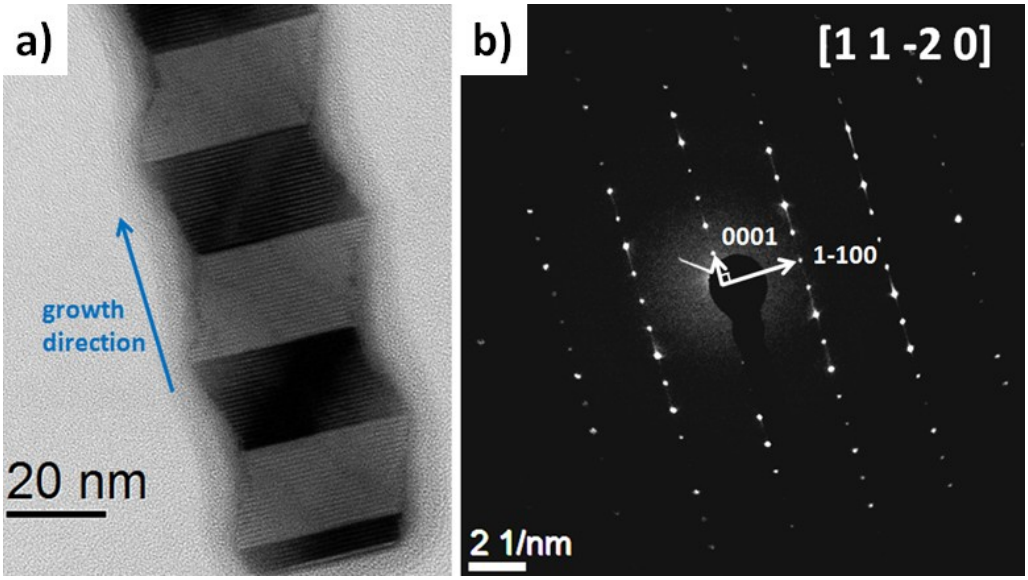

Figure 53: a) HREM image of a zig-zag NW. The relative DP is shown in **b).**

Before going on with the analysis, any possible artifact due to the presence of the defect needs to be ruled out. As a matter of fact, a twin defect doubles the diffraction spots if its mirror plane is not parallel to a direction that already contains a mirror symmetry element.

The only way to remove this ambiguity is to study the crystal structure in a single segment not containing the twin defect.

In Figure 54 a high magnification HREM image of the same wire shown in Figure 53 is reported. In the image two consecutive segments are depicted and the twin plane between them is highlighted by the red line. The FFT of the two regions, marked with the blue and green squares, are reported on the right side and are bordered with the same color of the region where they are taken.

As already mentioned in chapter 2.4, the FFT of an HREM contains the same information contained in the DP. For this reason it is now possible to compare the two FFTs with the DP shown in Figure 53 b. If the FFTs coincide with the DP, any effect of the twin on the DP can be ruled out.

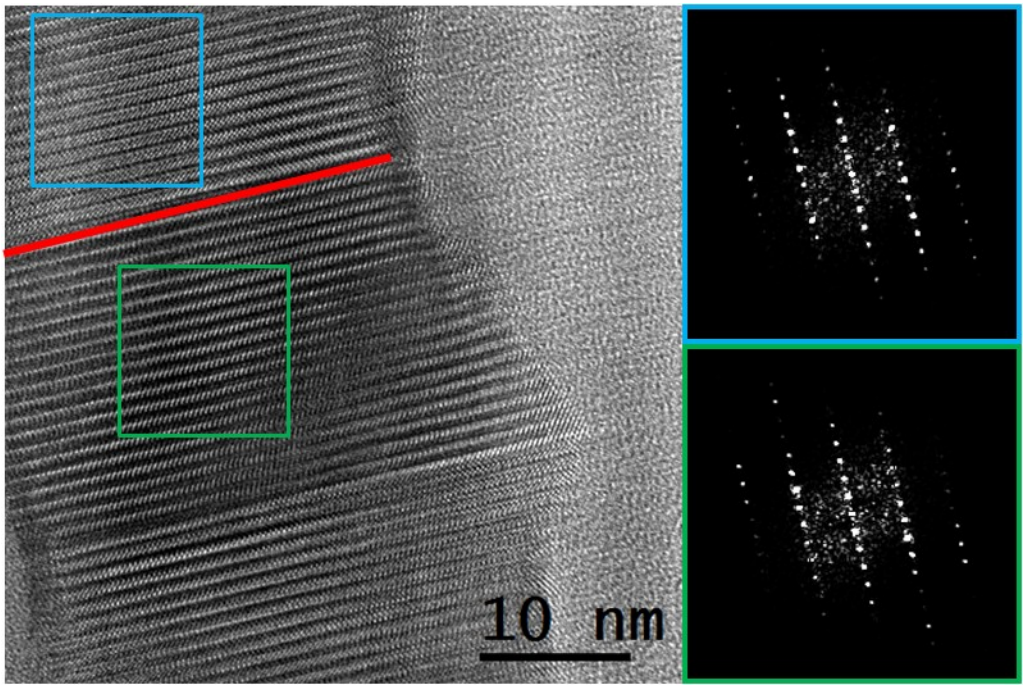

Figure 54: HREM image of two consecutive segments of the wire shown in Figure 53 a) The FFTs of the two marked regions are reported on the right side and are bordered with the same color.

The blue area is limited in the segment above the twin plane while the green one in the area below the twin so their FFTs are unaffected by the defect. The two FFTs are identical and they contain all the features also present in the DP which was obtained on the whole wire. Therefore what is seen in the DP is real and no artifacts are present.

The comparison allows to assess that the wires have a crystal structure different from the structure usually observed for the Sb_2Te_3 compound. More surprisingly, after an accurate investigation, no match with the observed structure is found in the literature indicating that the NWs probably possess a metastable phase never observed before.

Polytypism, namely the stabilization of metastable phases, is commonly observed in NWs because of the low dimension that can change the energetic balance of the structures.

Even though no studies are present in the literature about size effects on the crystal structure of Ge-Sb-Te NWs, this topic has been investigated for other compounds, mainly III–V and oxide semiconductors. In these materials, different from bulk or unexpected crystal phases have been observed. [63],[53]

Refining a new crystal structure directly from the TEM images can be difficult due to the strong dependence of the image contrast on the aberrations, defocus and thickness, as previously shown in Figure 19. In this context, HAADF-STEM imaging is more reliable.

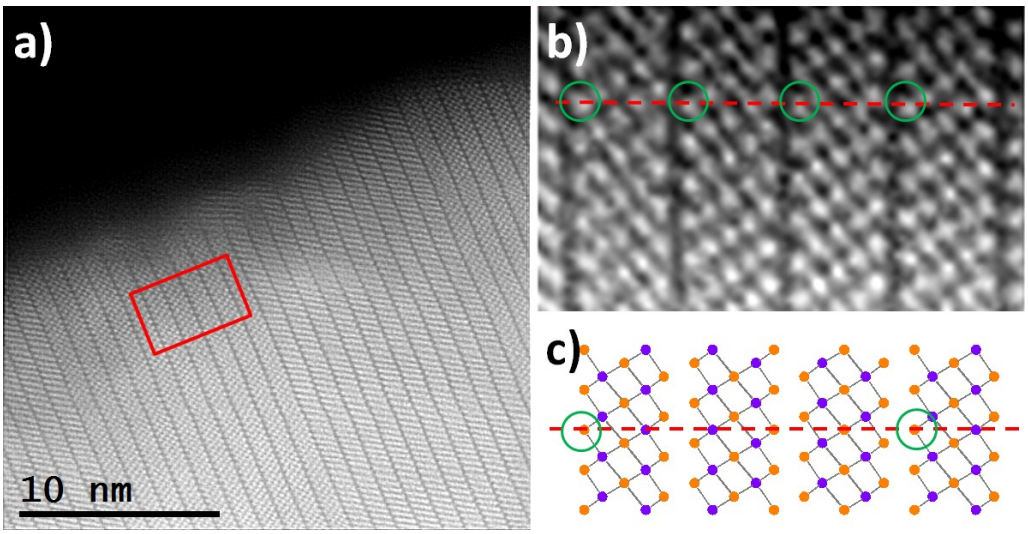

Figure 55: a) High resolution STEM-HAADF image of a zig-zag NW. **b)** enlargement of the red marked area in a). **c)** the crystal structure of the Sb2Te3 oriented in the same direction of the STEM images. The differences between them are marked.

In Figure 55 a) a Z-contrast image of a zig-zag NW oriented along the [11-20] projection is shown. A high resolution image of the red squared area is reported in b). The parallel dark lines correspond to the van der Waals gaps and each bright spot corresponds to an atomic column. The spacing between the van der Waals gaps is 1 nm and five atomic planes are present in each slab. These details are the same of the conventional structure.

Since the two structures are very similar, it can be useful, in order to refine a new structure, to highlight the difference between the observed structure and the one reported in the literature and reproduced in Figure 55 c). As an example, the red dashed line in Figure 55 b) runs parallel to the c axis and intercepts the first atomic column after each van der Waals gap, as indicated by the green circles. The same line, drawn on the structure from literature, intercepts one atomic column every three gaps only.

Finally, the new atomic positions are directly refined from the experimental image.

Combining these information with the previous analysis of the diffraction pattern we can conclude that the observed structure possesses a simple hexagonal lattice, with a 1 nm long c axis and 5 atoms per unit cell.

The details of the refined structure are reported in Table 5. An image of the refined structure is also reported in Figure 56.

Refined Cell			
Space group P-33m (#164)			
a = 0.426 nm		b = 0.426 nm	c = 1.060 nm
Atom	**x**	**y**	**z**
Te	0	0	0
Te	0.3333	0.6667	0.6385
Sb	0.3333	0.6667	0.1965

Table 5: details of the refined cell.

As further confirmation, an image simulation has been performed and has been found to perfectly match the experimental data, as shown in the right side of Figure 56, where the image simulation is overlapped, as inset, on to the experimental one.

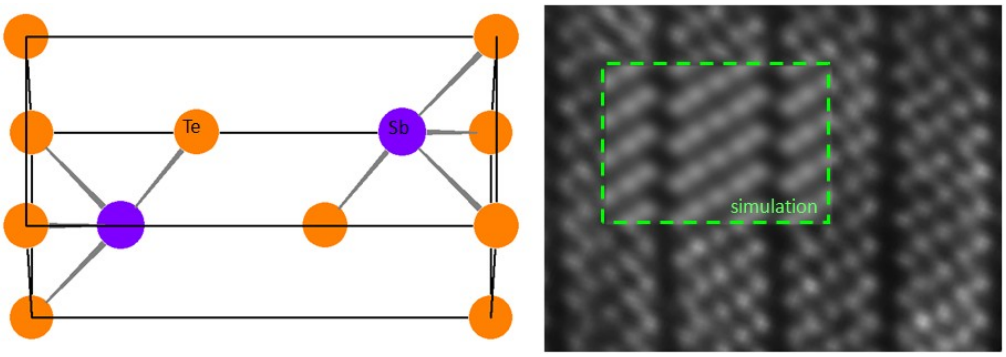

Figure 56: left side: graphical representation of the refined cell. **Right side:** an image simulation of the refined structure overlapped with the experimental image.

The building block is the same in the structure from literature and in the refined one. The only difference is the way they stack one on top of the other.

In the conventional structure each pentalayer is rotated by 120° with respect to the previous one and three of them, stacked along c axis, compose the unit cell. In the new one no rotation is present, and the block itself coincides with the unit cell.

In order to understand if a finite size effect can favor the Sb_2Te_3 to crystallize in the new structure with s.g. 164 symmetry instead of the common one, theoretical calculation have been performed

by the group of Prof M. Bernasconi in Università di Milano Bicocca. All the calculations have been performed on the basis of the density functional theory (DFT) using the Quantum-Espresso code.[64] The Perdew-Burke-Ernzerhof (PBE) exchange-correlation functional and norm conserving pseudopotentials were employed. The semiempirical Grimme correction was also used to account for van der Waals forces.

The analysis confirms that the new phase is energetically unfavorable in bulk material, being its formation energy higher than the phase from literature. The energy difference between them is $\Delta\mu = 5.4 meV / atom$.

It is widely recognized that this thermodynamic favoring of bulk structures can be offset in nanowires having small diameter by the relatively large contribution to the total energy of the lateral facets. [65]

The surface energy of the (11-20) and (1-100) facets, corresponding to the most important directions orthogonal to the wire growth axis, has been calculated. The results are reported in Table 6.

Surface Energy Analisys		
	(11-20) surface	**(1-100) surface**
Bulk structure	34.4 meV/Å^2	37.1 meV/Å^2
New structure	34.1 meV/Å^2	33.6 meV/Å^2

Table 6: comparison between the formation energy of the main facets, orthogonal the growth direction, of the two structures.

Including the surface energy contribution, the energetic balance becomes:

$$\Delta E = 2\pi\Delta g L R + \pi\Delta\mu R^2 \left[n_v L - n_s \right] < 0 \qquad (4.1)$$

being Δg the surface energy difference between the two phases, n_v the bulk atoms density per unit volume, n_s the surface atoms density per unit area, L and R the wires length and radius respectively.

Solving equation 4.2, a critical radius of 3.3 nm has been calculated, below which the NWs with the new phase should be more stable than NWs having the bulk structure.

Although the predicted value is smaller than our NWs size, the important result is that the finite size accounts for the growth of the new phase. On the contrary, the discrepancy between the values seems to be not as important: indeed, similar calculations to explain the occurrence of the metastable wurzite polymorph in GaAs NWs predict a critical radius of 5.6 nm, while it is commonly observed in wires with radii as large as 100 nm [66].

Chapter 5: HEXAGONAL Si NANOWIRES

5.1 Introduction

Silicon is the mainstay semiconductor in microelectronic circuitry but it is considered unsuitable for optoelectronic applications owing to its indirect electronic band gap, which limits its efficiency as a light emitter. As a matter of fact, cubic bulk silicon has an indirect band gap of 1.1 eV and does not emit radiation with an appreciable intensity neither in the visible range nor at any other wavelength.

Anyway, light emission in Silicon is found when selected active impurities (such as erbium [67]) or line defects (as dislocation [68]) and/or new phases (such as iron disilicide [69]) are inserted into the Silicon lattice.

Room-temperature light emission from silicon has been recently reported also in low-dimensional systems such as nanocrystals [70], nano-pillars [71] and porous silicon [72].

One-dimensional semiconductor architectures, such as nanowires and nanotubes, are crucially important in materials-based applications requiring large surface area, morphological control, and superior charge transport. In particular, diamond Si NWs have recently gained increasing attention for solar cell applications due to their superior properties, such as diameter-tunable optical absorption [73] and optical bandgap [74], low reflectivity [75], and stronger optical absorption in the visible region [76] compared to bulk and amorphous Si.

Si NWs have also other interesting properties: in 2007, the pioneering work of Fontcuberta i Morral and co-workers [77] demonstrated how a hexagonal wurtzite phase of Si can be stabilized in NWs thanks to the low dimension.

Wurtzite Si NWs are more attractive for solar cell applications than diamond NWs, due to the possible optical bandgap engineering of the different Si polymorphs in the device design, as for III–V based multijunction solar cells.

Despite the strong interest, the light emission properties of this material have not yet been studied in detail. Some theoretical studies [78] [79] predict that the WZ-Si indirect band-gap is in the near infra-red range, while a direct transition at the Γ point is expected at around 1.4-1.5 eV.

Should these predictions be proven and supported by experimental optical emission studies, a new scenario in the field of silicon-based rare-earth free optoelectronic devices will open. This development will have important implications not only for the scientific community, but also for the optoelectronic device market.

Si, in its stable bulk phase, crystallizes in the same pattern as diamond, in a structure described by Ashcroft and Mermin [80] as "two interpenetrating face-centered cubic" primitive lattices displaced along the body diagonal of the cubic cell by one quarter the length of the diagonal. It can be regarded as a face-centered cubic lattice with two atoms basis in the positions (0, 0, 0,) and $\left(\frac{1}{4},\frac{1}{4},\frac{1}{4}\right)$, as reported in Figure 57 a). The lattice parameter is a=0.543 nm.

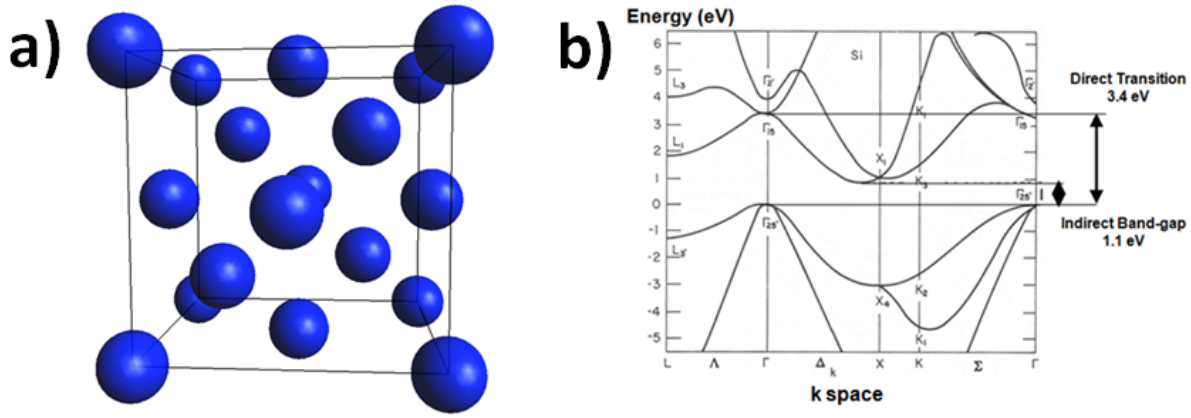

Figure 57: a) atomic model of the diamond cubic structure of Si. **b)** the band structure diagram of diamond Si.

The band structure of cubic Si is reported in Figure 57 b). The conduction band minima lie on the six equivalent Δ-lines, namely the straight line from point Γ to point X, and occur at about 0.85% of

the way to the zone boundary, close to the X point. There is also a second minimum in the first conduction band at point L, which lies 1.0 eV above the first valley.

The valence band maximum for the heavy-hole, light-hole, and for the split-off band is located exactly at the Γ-point. Therefore, Si is an indirect semiconductor because the maximum of the valence band (at Γ) does not coincide with the minimum of the conduction band (to the left of X).

The radiative efficiency of the 1.1 eV transition is very low because, in order to have the carriers recombination, a phonon is needed to balance the momentum.

The smallest energy for a direct transition is 3.4eV corresponding with the transition at the Γ point. Anyway the efficiency of this transition is too low to be exploited.

In contrast, the metastable phase presents a wurtzite structure (also named Si IV polymorph, space group *P6mc*). A wurtzite crystal structure belongs to the hexagonal crystal system, consisting of atoms coordinated in a tetrahedral way, stacked in an ABABAB pattern along the (0001) hexagonal direction. To highlight the difference between the cubic and the hexagonal structure, a cubic structure can be described using hexagonal axis but the resulting stacking along the (0001) will be ABCABC. The Si IV unit cell has lattice parameters a = 0.38 nm and c = 0.627 nm with two atoms basis in the positions $\left(\frac{1}{3},\frac{2}{3},0\right)$ and $\left(\frac{1}{3},\frac{2}{3},\frac{3}{8}\right)$, as reported in Figure 58 a).

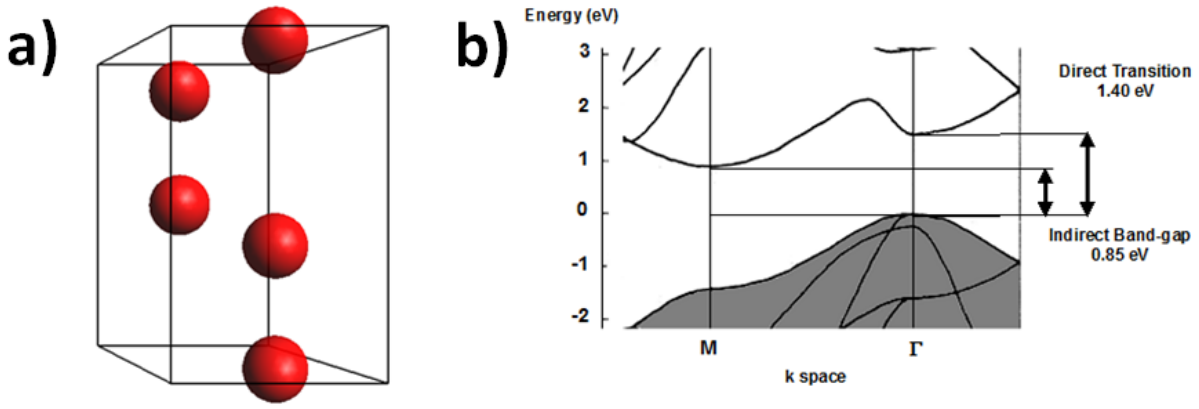

Figure 58: a) atomic model of the metastable wurtzite IV structure of Si. **b)** the band structure diagram of Si IV.

The different atomic arrangement results in a different band structure, shown in Figure 58 b). Here, the energy values of the indirect band-gap at the M point and of the direct transition at the Γ point are highlighted. The direct transition for Si IV is only 1.4 eV therefore high efficiency is expected, even if it has never been experimentally observed.

In order to stabilize the Si IV phase, Si NWs are synthesized by means of a gold nanocluster catalyzed VLS growth mechanism in a commercial cold wall CVD system at a total pressure ranging from 8 to 10 Torr. The growth rate of NWs was about 300 nm/min. The substrates were thermally oxidized Si with an oxide thickness of 200 nm; Au colloidal nanoparticles of 3 nm in diameter were used as metal catalyst. The growth temperature is 600 °C and SiH_4 is used as the silicon reactant gas. The samples have been grown by Doctor Naoki Fukata at the International Center for Materials Nanoarchitectonics in Tsukuba, Japan.

Figure 59 a) shows a SEM image of the typical nanowire mat obtained by this procedure.

In order to determine the optical bandgap of Si NWs, their optical properties are studied by means of cathodoluminescence spectroscopy.

The advantage of using CL spectroscopy in the characterization of NWs is mainly due to a straightforward information on the band gap nature (see, for example, ref [53]) and to the high injection power indispensable in case of materials with low luminescence efficiency like Si (see, for example, ref [81]).

In Figure 59 b) the CL spectra of the obtained NWs and of a reference Si bulk sample, red line and blue line respectively, are reported.

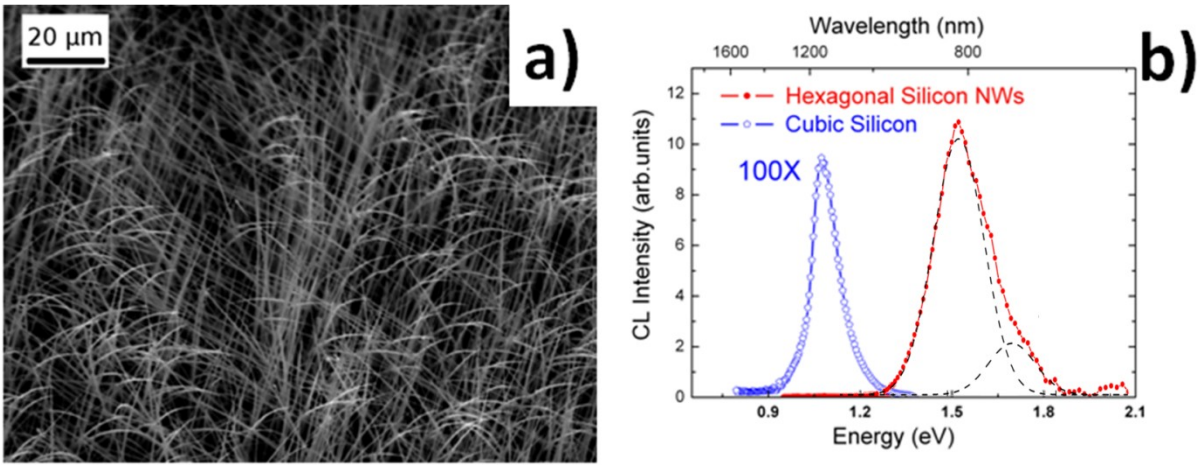

Figure 59: a) SEM tilted view of the as grown NWs. **b)** CL spectrum of the Si IV NWs in red. In blue a CL spectrum obtained on a reference bulk Si sample is reported.

The reference bulk Si sample spectrum shows a sharp peak located at about 1.1eV, corresponding to the indirect band transition while the spectrum obtained on the NWs sample contains emission in a completely different spectral range.

It is worth noticing that the intensity of the reference spectrum had to be enhanced a 100 times to be compared with the intensity of the spectrum obtained on the NWs sample, meaning this that

the radiative efficiency of the transition observed in the NWs is very high in comparison with bulk silicon.

Gaussian deconvolution procedure of the NWs sample CL spectrum, the black dashed lines in Figure 59, reveals the presence of two bands underneath the main broad emission. A first band is peaked at 1.53 eV with a shoulder on the high-energy side at 1.68 eV. The shoulder emission can be ascribed to amorphous silicon [82] and/or to under-stoichiometric silicon dioxide [83] while the value of the main peak is consistent with the theoretical predictions of the direct transition at the Γ point of Si IV.

The TEM analysis confirmed the presence of the Si IV phase in the analyzed NWs as discussed in the following section.

5.2 TEM analysis on Si IV

The existence of the Si IV phase is still a controversial topic in the literature and, during the years, many papers have been published confirming or otherwise denying the existence of Si phases different from the diamond one.

According to some authors, the wrong attribution of the wurtzite phase is possible if the TEM images are misinterpreted in presence of defects in the cubic phase that can produce the same fringes and diffraction patterns as in the hexagonal structure. In this chapter, the result of these works will be summarized and, for each theory, a specific experiment will be carried out in order to rule out any misinterpretation in the phase identification. The same procedures here exposed will be used, in the following sections, wherever an attribution to the Si IV system is done.

The first report on possible misinterpretation of TEM images in nanometric systems discussed in this section has been published in 2003 by Kohno and co-workers.[84]

The authors successfully demonstrate how a twin plane orthogonal to the (111) direction in cubic silicon originates misleading fringes, which can be easily confused with the (0001) projection of Si IV, when observed along this direction. Moreover these misleading fringes do not disappear even if the sample is rotated widely apart.

Figure 60 shows the atomic model of two NWs with the two different structure: the bulk cubic structure, containing a twin defect in the middle of the wire (yellow dashed line), in a) and the metastable Si IV in b). The two wires are imaged in a cross section view and the primary electron beam direction is reported. Finally, according to a similar paper, a tangled set of micro- and nanotwin, hidden inside the body of the NW, can produce the same effect.[85]

The image simulations obtained with the two structures are reported in Figure 60 c) and d) respectively.

The presence of the twin defect actually produces artifacts in the HREM image. The HREM image simulation of the Si IV sample, Figure 60 d) clearly shows a lattice periodicity of 0.33 nm. The lattice periodicity is marked in the image and the corresponding diffraction spot is pointed out, with the red arrow, in the FFT reported as inset. The 0.33 nm periodicity corresponds to the (1-100) interplanar distance in the Si IV system.

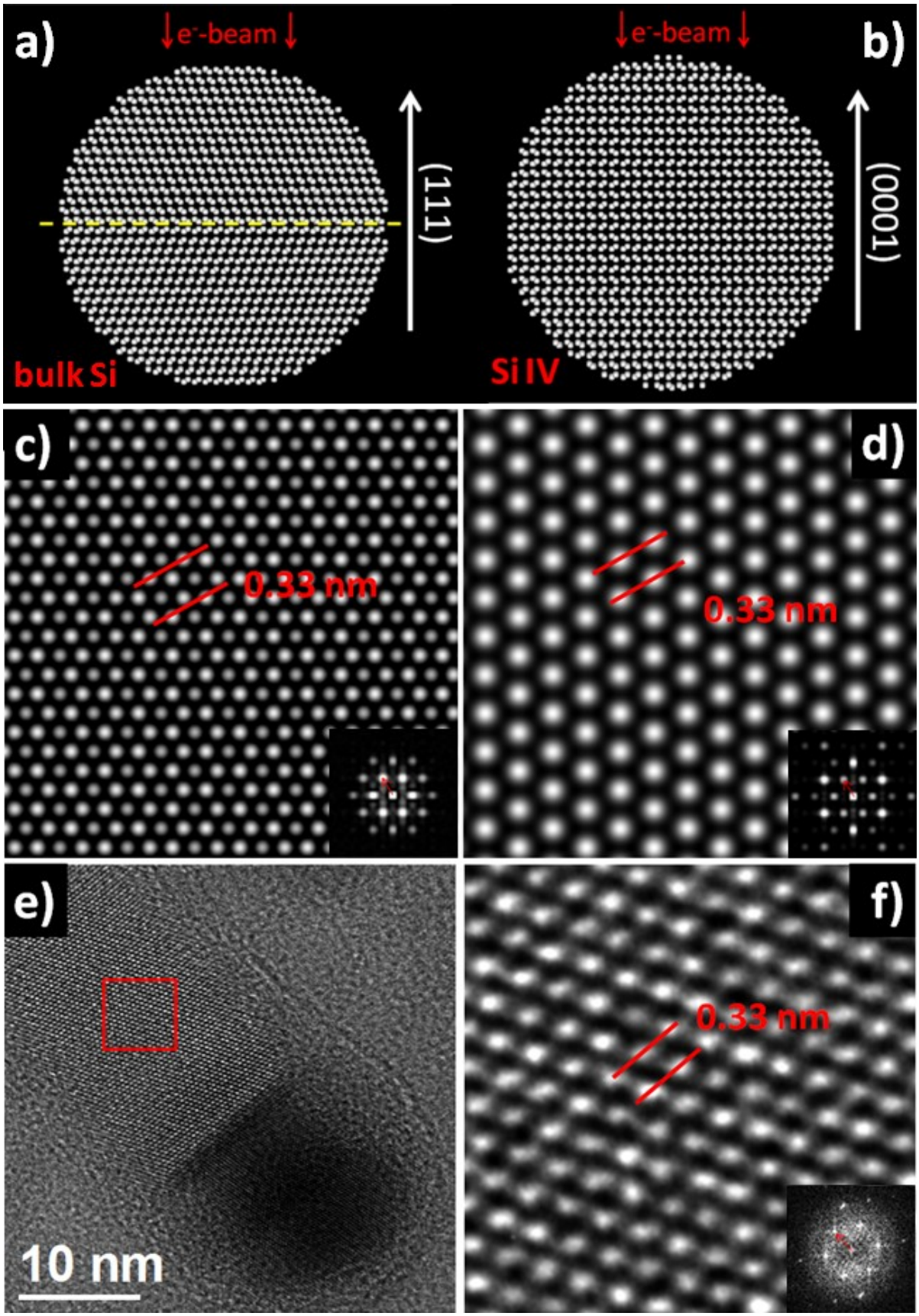

Figure 60: The simulation set up of the two structures that can be confused during TEM experiment: **a)** diamond silicon with a twin plane orthogonal to the (111) direction (Bulk Si) and **b)** wurtzite Si imaged along the (0001) projection (Si IV). The simulated images are reported in **c)** and **d)** respectively. For comparison, an experimental TEM image of a 10 nm thick NW is reported in **e)**. The high magnification image of the red marked region is reported in **f)**. The FFT of each image is reported as inset.

The same periodicity is also present in the simulation of the twinned bulk phase reported in Figure 60 c) and is clearly visible in the FFT. Anyway, after carefully analyzing the image, it can be seen how this periodicity only appears as a super-periodicity produced by an intensity modulation, while the real periodicity remains the equal to 0.192 nm, corresponding to interplanar spacing of the diamond Si (110) planes family.

Both the HRTEM image simulations have been done in order to mimic a 10 nm thick Si NW imaged at a defocus of −40 nm, corresponding to the Scherzer defocus of a microscope working at 200 kV and using an objective lens with spherical aberration coefficient Cs=0.5 mm, being these the same parameters of the microscope used to obtain the HREM image of the 10 nm thick Si NW reported in Figure 60 e).

An enlargement of the red marked square is reported in Figure 60 f) to better show the atomic periodicity. The 0.33 nm periodicity is found in the experimental image and has been highlighted both in the image and the FFT reported as the inset of Figure 60 f).

The pattern observed in the experimental image perfectly matches the simulation of the Si IV phase because the observed periodicity is real and no intensity modulation is observed.

It can be objected that the presented result is demonstrated only for a fixed thickness/defocus value. In order to make it more general a full set of simulation has been performed in order to cover a wider range of experimental conditions.

In Figure 61 the effect of the defocus on the image contrast pattern is studied. The first row, labeled as tSi, shows a focal series of the defected Si structure, for defocus ranging from -20 to -60 nm, symmetrical with respect to the Scherzer value. In the second row, the same focal series is proposed for the Si IV phase, shortened in hSi for simplicity. All the image simulations have been obtained for a fixed thickness of 10 nm.

Instead, in Figure 62, the effect of the thickness on the image contrast is studied. The two rows, labeled as in Figure 61, report the thickness series for the two structures, in the range from 10 to 40 nm. All the image simulations have been obtained at Scherzer defocus.

As expected, the contrast pattern is changing significantly with thickness and the defocus (see chapter 2.5) but all the images have a common feature: the 0.33 nm periodicity always appears as a real periodicity in the image referring to the Si IV phase and as super periodicity due to intensity modulation in the defected structure.

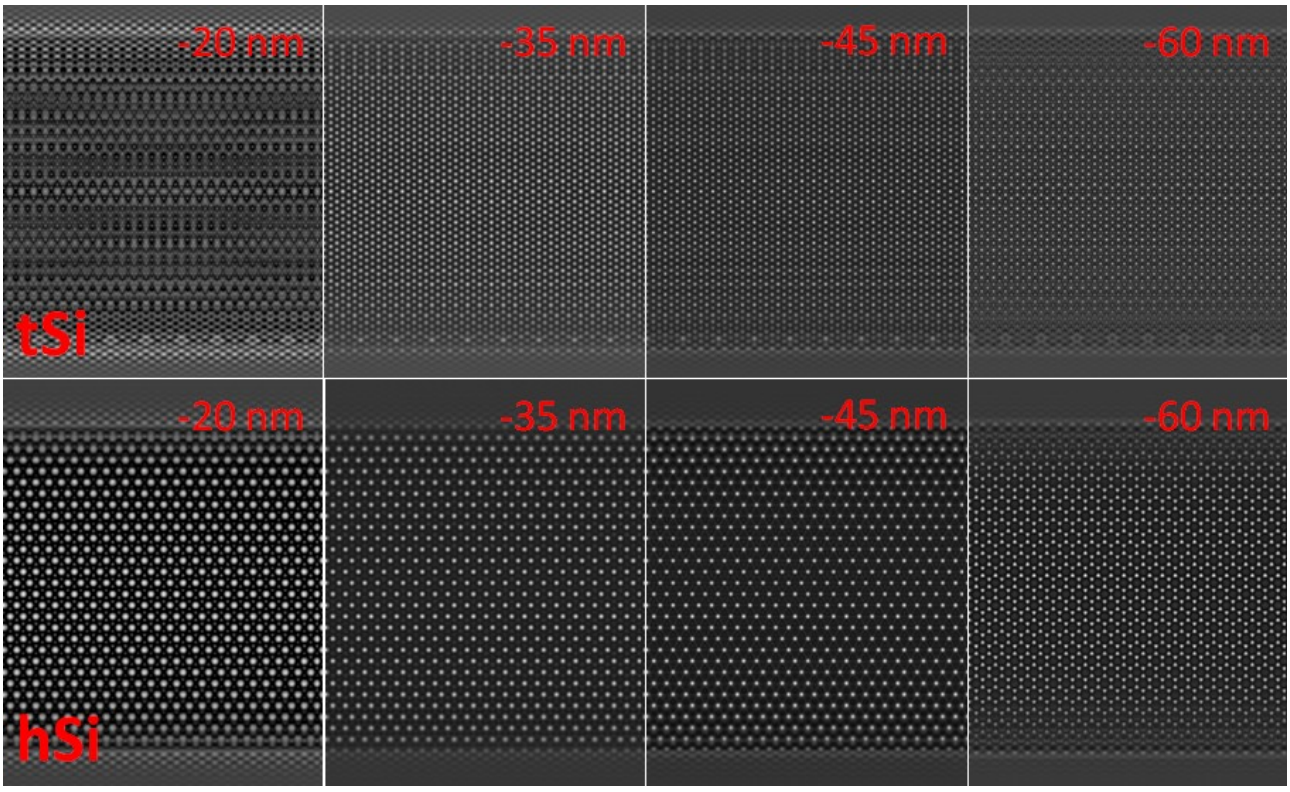

Figure 61: Comparison of HRTEM simulations of the twinned diamond Si (**tSi**) and wurtzite Si (**hSi**) at different defoci.

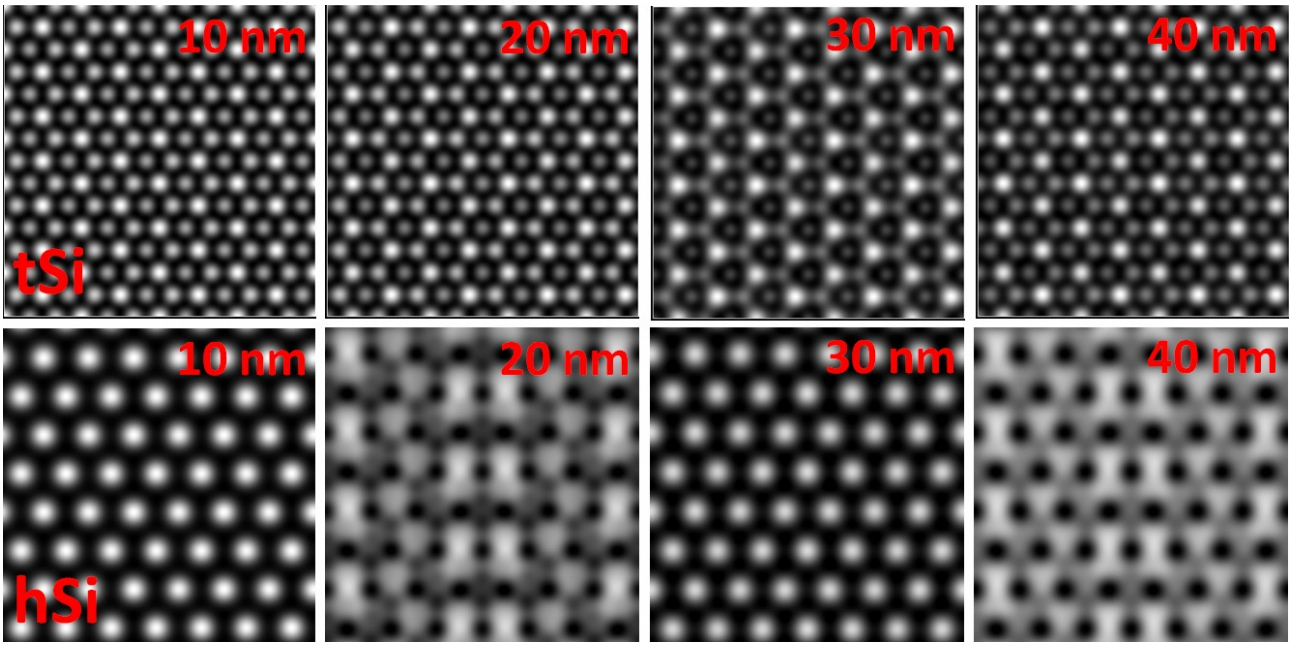

Figure 62: Comparison of HRTEM simulations of the twinned diamond Si (**tSi**) and wurtzite Si (**hSi**) at different thicknesses.

In the literature, the lattice periodicity of 0.33 nm has also been observed in very thin diamond Si nanowires (see, for example, refs [86][87][88]) where it has been attributed to the forbidden 1/3 ⟨422⟩ reflections of the bulk Si phase, according to very well known papers by Ourmadz *et al.* [89] and Gibson *et al.* [90].

The explanation to justify the presence of the forbidden fractional reflections of the type 1/3 ⟨422⟩ cannot be applied to our case for two main reasons:

(1) According to ref [89] the possibility to see such reflections is limited to "exceptionally thin and flat" samples having a thickness not exceeding 30 nm as in the case of refs [86] [87][88]. In the present case, those reflections are observed in wires with diameters up to 260 nm, as the one reported in Figure 63 a), that are neither thin nor flat.

(2) The papers that deal with these forbidden reflections (see ref. [90] and references therein) insist that they are weak; on the contrary, in the present case, they are at least as intense as the common [220] reflections, but in some cases they are even more intense, as it can be seen in DP reported in Figure 63 b).

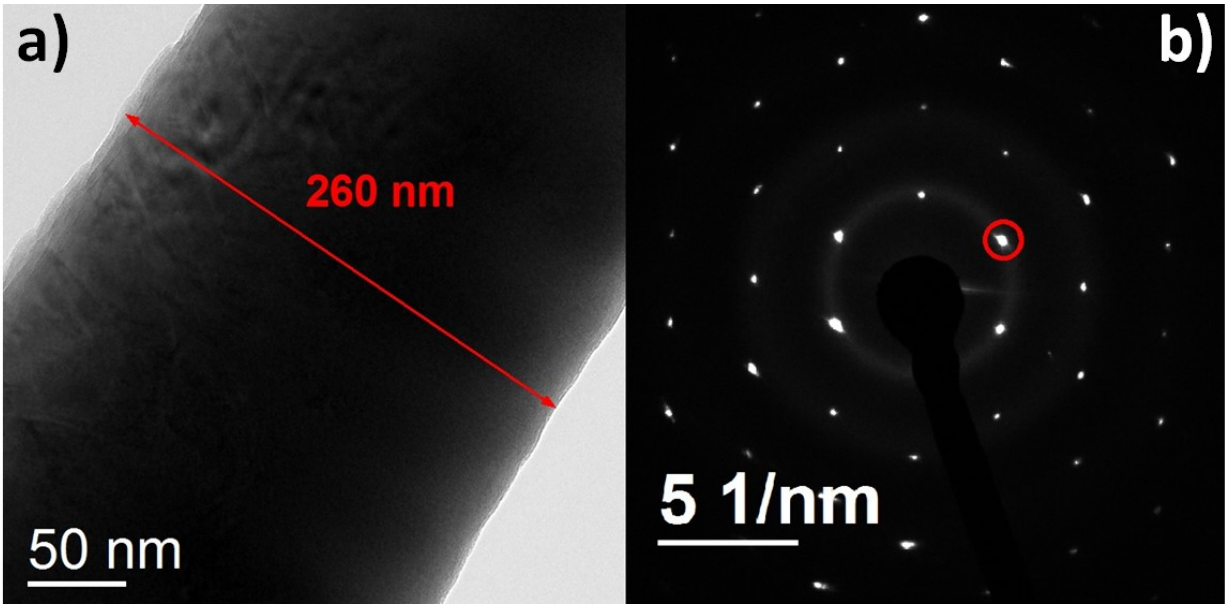

Figure 63: TEM image of a 260 nm thick NW **a)** and relative DP **b)**.

Before ending this section a conclusive remark is needed. The easiest way to remove any ambiguity in the identification of the crystal structure is imagine along the [11-20] projection. However, we were unable to find it. The wires analyzed in this work mainly grow along the (1-100) direction which is one of the six main basal directions. This implies the presence of other 5

direction equivalent to the growth axis in the same plane that causes our NWs to have an ellipsoidal section rather than circular.

This also means that our wire lie preferentially on the (0001) plane, that is orthogonal to the (11-20) one, which therefore is beyond the tilting limit of our microscope.

5.3 Doping of Si IV NWs

A material per se cannot be used for any application if not suitably treated. In particular, doping with selected electrically active impurities is of crucial importance to enable the control of the conductivity and the formation of p/n junctions, which are required for almost any electronic application. The study of wurtzite Si NWs is still in its infancy and until now only a very few papers reporting about growth mechanisms and structural properties can be found in the literature, none of them concerning the growth of doped wires.

To fill this lack of information in the literature an attempt to grow doped Si IV NWs have been done. This chapter reports on the growth of gold-catalyzed n-doped (doped with P atoms) and p-doped (doped with B atoms) Si IV NWs. [91][92].

The morphology and crystalline structure of the grown NWs, hence the optical properties and the bandgap, turned out to be strongly affected by doping. In particular, solid experimental evidences demonstrate that B and P dopants have different effects on retaining the phase of the grown NWs.

Si NWs are synthesized using the same experimental set up already described for the undoped wires. For B- and P-doped NWs synthesis, they are directly grown onto thermally oxidized Si substrates at a temperature of 600 °C for 30 min in flowing 19 sccm of SiH_4 as the silicon reactant gas, 1% B_2H_6 (0.5 sccm) in H_2 as p-type dopant gas, 1% PH_3 in H_2 as n-type dopant gas and 30 sccm of nitrogen (N_2) as the carrier gas. The growth results are shown in Figure 64.

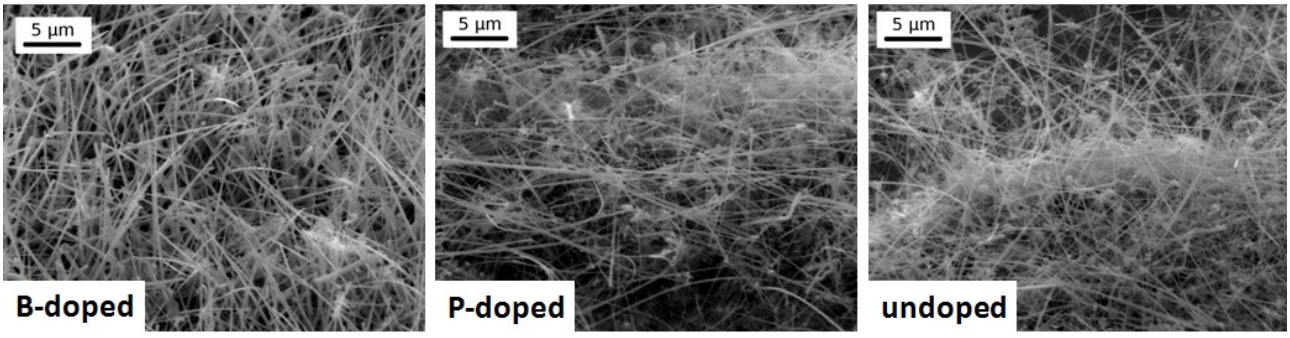

Figure 64: Morphological analyses of B-, P-doped and undoped Si NWs.

The comparison of the SEM images of the B-, P-doped and undoped Si NWs reveal a slightly different morphology of the B-doped sample in respect with the other two samples that show similar shape and size. The NWs present on the B-doped sample have a tapered shape, i.e. the

diameter varies from the tip, about 10 nm, down to the base of NWs, usually over 500 nm. Conversely, P-doped wires have cylindrical shape with an average of 50 nm diameter that does not vary along the wires length. As a direct consequence of the larger diameter of the NWs the B-doped sample has a lower NWs density. All the three kind of wires have a length exceeding 30 µm.
If the P-doped NWs have a trivial cylindrical shape that doesn't need further investigation, the morphology of the B-doped wires needs a deep understanding. TEM imaging reveals more details on the morphology of the B-doped wires as shown in Figure 65.

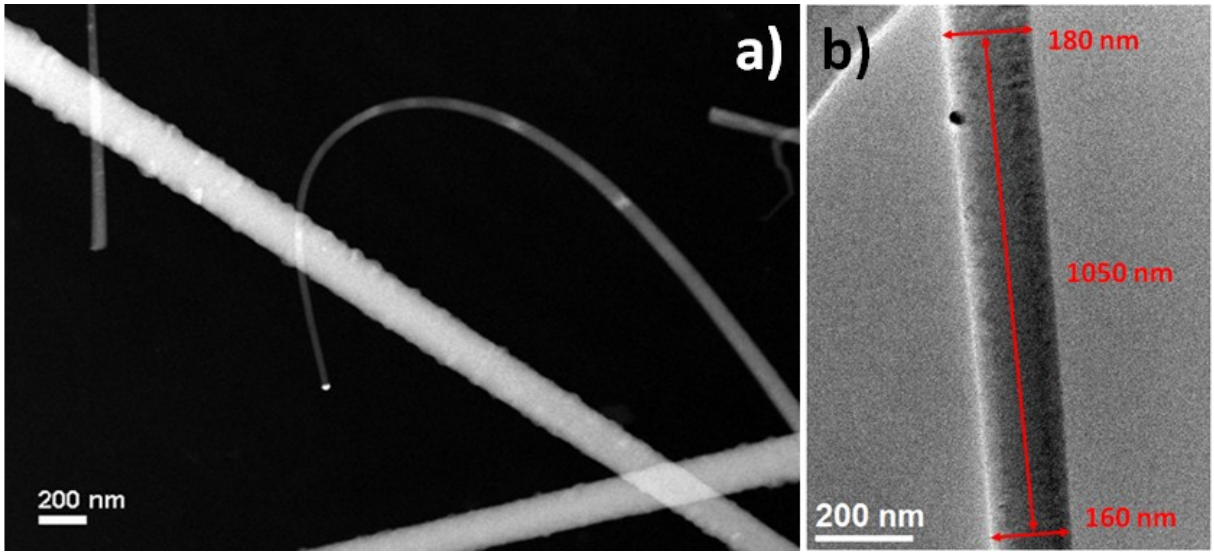

Figure 65: TEM morphology of B-doped wires**. a)** low magnification STEM image and **b)** low magnification TEM image.

Figure 65 a) shows a very low magnification STEM image of a few NWs dispersed on the C grid. The brightest particle in the center of the image is the Au tip of the thinner wire. The diameter, at the tip, is about 30 nm and monotonically increases towards the bottom of the wire. It can also be noticed that the wire walls are smooth. Unfortunately it is impossible to further follow this NWs because the TEM does not allow a lower magnification, therefore we move to the thicker wire, which is crossing the image from the upper left corner to the bottom right one.
The diameter is now increased to 250 nm (on the upper part). It can be noticed how the sidewalls of the wire become rough when the diameter reaches 200 nm.
The tapering has been evaluated by means of low magnification TEM images as shown in Figure 65 b) where the image of a 1 µm long part of a wire is reported. The wire diameter changes from 160

nm to 180 nm. The tapering can be evaluated as the percentage increase in diameter per length unit: $\frac{\Delta R}{L} = 2\% \frac{\Delta R}{L} \approx 2\%$.The same value has been measured for all the wires.

5.4 Crystal structure

As already mentioned, the crystalline structure of the growth products is also affected by the doping. The TEM investigations show that the undoped, the B- and P-doped NWs can crystallize in the wurtzite or diamond phases and the two different polymorphs never occur simultaneously in the same NW. Two HREM images of a Si IV and a diamond Si NW are shown in Figure 66 a) and b) respectively. The DPs of the two wires are indexed and reported as inset.

In particular the angle between the major directions in two DPs is indicated: for the Si IV wire in a) a 120° angle is measured, corresponding with the angle between two (10-10) reflections in the [0001] zone axis. Conversely, in b), a 109.5° angle is measured corresponding with the angle between the (111) reflection for a diamond system.

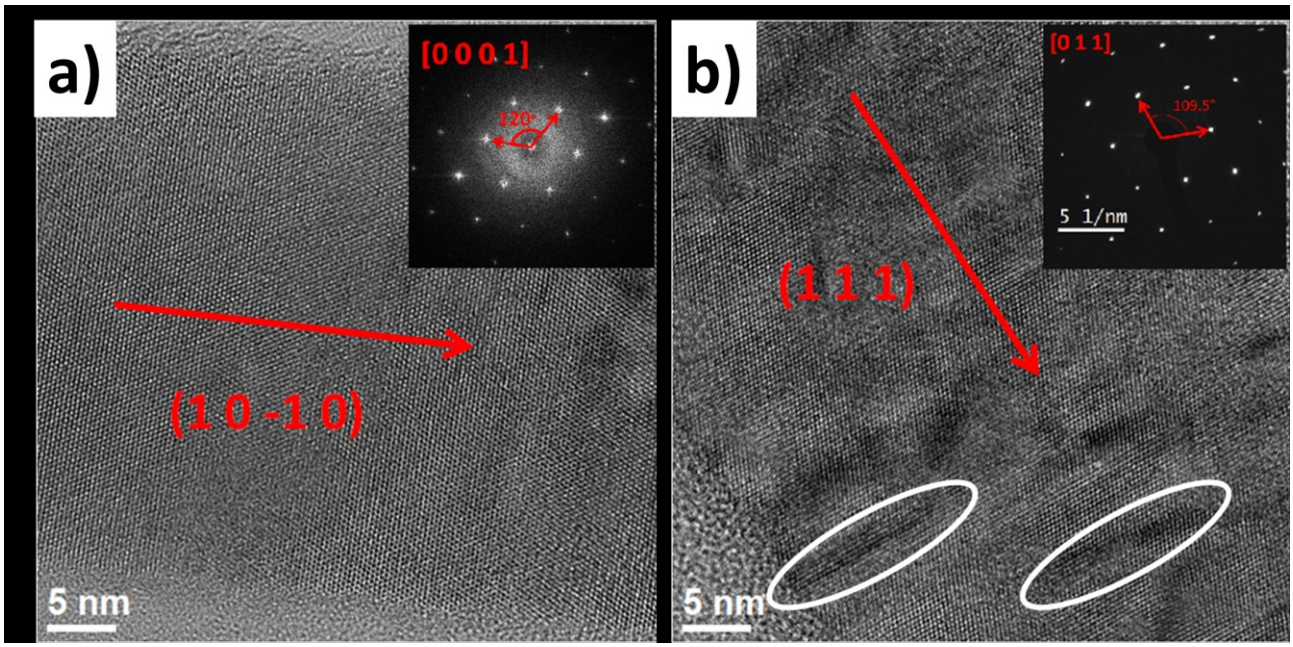

Figure 66: HREM images and DPs (in the inset) of a Si IV NW **(a)** and a diamond Si NW **(b).**

From the TEM analyses, it is found that the doping species have a completely different effect on the crystalline properties of the NWs, thereby causing the variation of the relative abundance of two polymorphs, as shown in the histogram in Figure 67 a) where the percentage abundance of the IV and diamond Si NW in the undoped (green), B-doped (red), and P-doped (blue) samples is reported.

The onset of the small percentage of the diamond phase in B-doped NWs compared to the undoped ones is probably related to the stress release caused by the formation of planar defects like the stacking faults circled in white in Figure 66 b).

Doping with P instead, destabilizes the Si IV as only 30% of the wire posses this structure.

The comparison among the CL spectra of undoped, B-, and P-doped Si NWs (closed symbols), and bulk Si (open symbols) is shown in Figure 67 a). Again, the CL emission from bulk Silicon, reported as reference, is magnified 100 times with respect to the other transitions. This result emphasizes the much higher emission efficiency of Si IV NWs, even if doped.

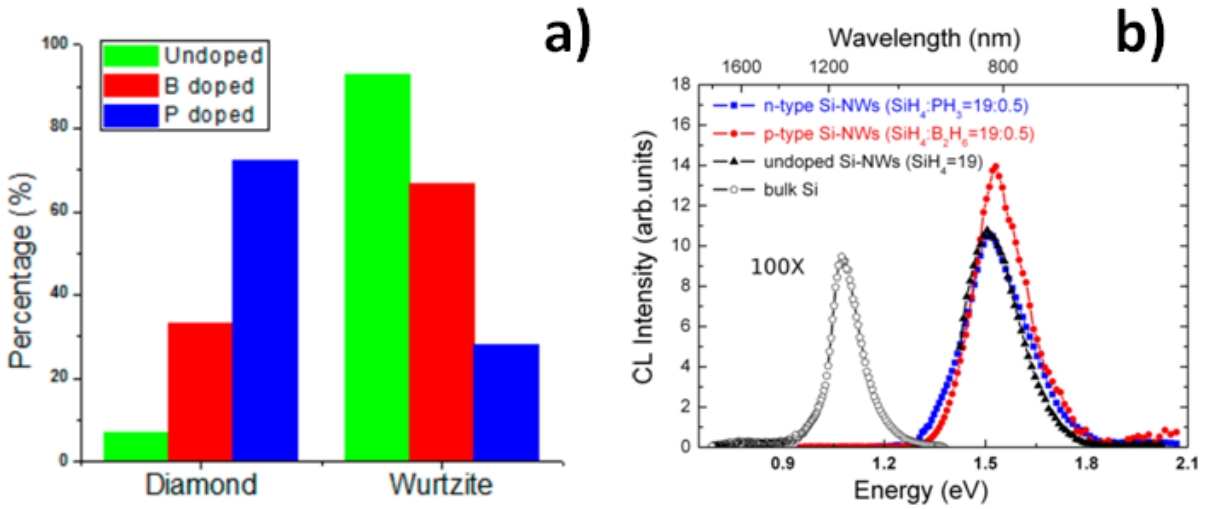

Figure 67: a) Abundance of the wurtzite and diamond Si polymorphs NW in the undoped (green), B-doped (red), and P-doped (blue) samples. **b)** Comparison among the CL spectra of undoped, B-, and P-doped Si NWs (black, red and blue symbols), and bulk Si (open symbols).

By comparing the CL integrated intensities of the 1.53 eV peak for all the NWs, the B-doped NWs intensity results stronger than those of the undoped and P-doped ones. The undoped NWs have almost the great majority of wurtzite phase but have the same CL integrated intensity of the P-doped ones; further, the NW densities we measured are 8×10^{8} and 10^{12} cm^{-2} for B doped and P-doped mats, respectively.

From these observations, it follows that the more intense CL emission of the B-doped samples can only be due to their larger diameter with respect to the undoped and P-doped NWs. Actually, as shown by the Monte Carlo simulations in Figure 29, the shape and dimension of the generation volume and the CL efficiency depend on the NW diameter. As a consequence, larger NWs allow for larger generation volume and give higher CL integrated intensity.

Finally, the intensity of the shoulder at 1.68 eV, which was ascribed to the presence of amorphous Si, is higher in the B-doped sample than in the other samples.

This is most likely due to the presence of a third kind of NWs in the B-doped sample. This third kind has been called “flawed NWs” to distinguish them from the perfect Si IV and diamond ones.

The flawed wires appear to be seriously defective but a careful inspection shows that they have a cubic Si core embedded in a thick, amorphous Si shell. The central image in Figure 68 shows one of these NWs. The blue dashed lines mark the border between the core and the amorphous shell. Across the border a definite contrast change is present.

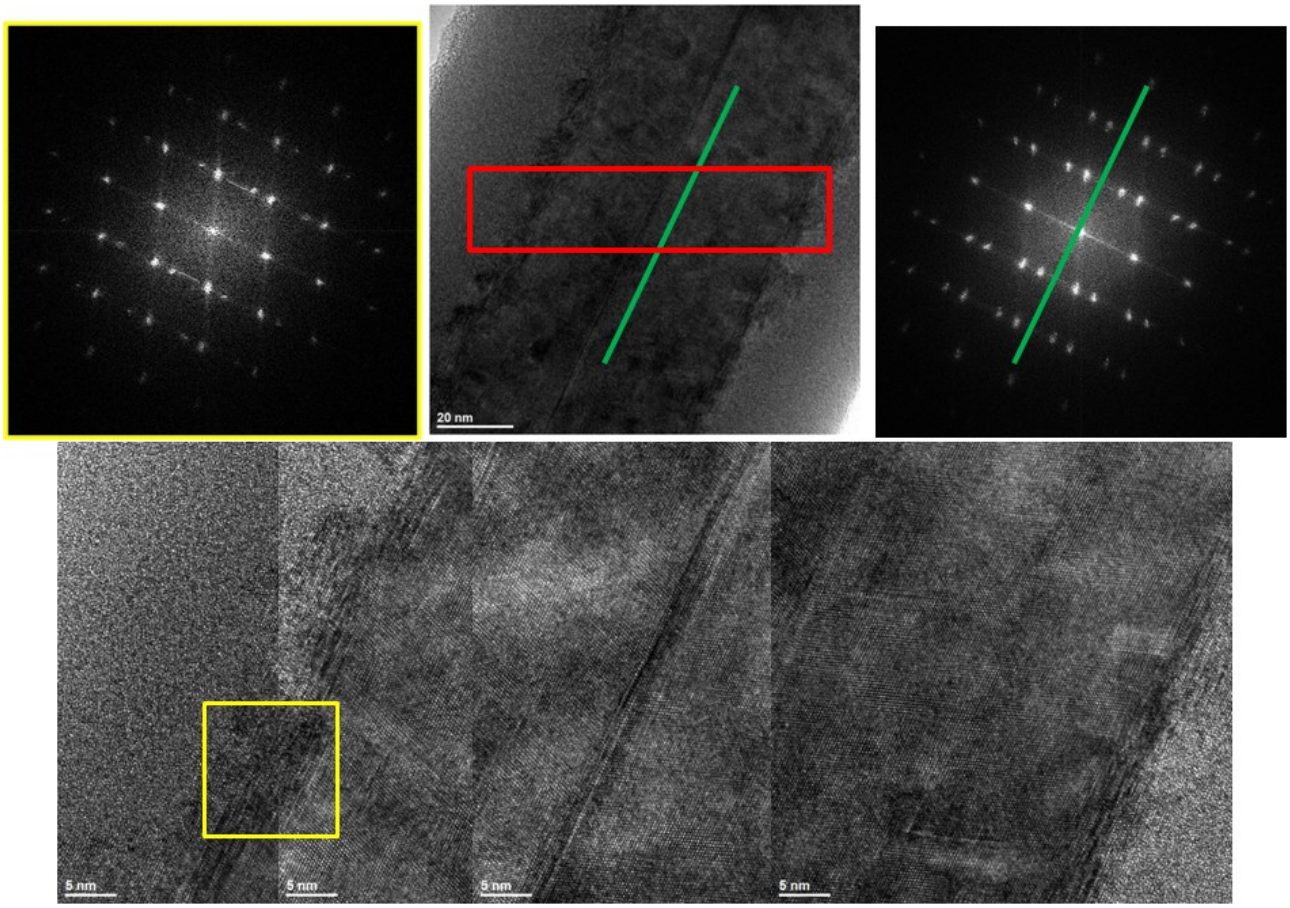

Figure 68: TEM structural study on a flawed wire.

A high resolution image of the red marked region is reported in the bottom part of the figure. It is actually composed by merging together 4 HREM images to span over the entire region.

At the interface, the cubic core fades into the amorphous shell through arrays of short stacking faults along the (111) directions. One of these arrays is marked with the yellow square. The FFT of the squared region is reported in the top left corner of the image and is used to define the crystallographic orientation of the defects. In the center of the wires at least one twin plane is

always present running all along the NW length. The presence of the twin defect is testified by the FFT in the top right corner image. It shows the same pattern observed in the first FFT but all the spot contained in it are doubled. Analyzing the symmetry of the FFT the mirror plane of the twin defect can be found. It is indicated by the green line. In parallel with this line, a second green line is drawn in the central image close to the twin defect that can be easily observed.
Moreover, the thickness of the amorphous Si shell increases along the wire while the diameter of the core region remains constant as demonstrated in Figure 69.

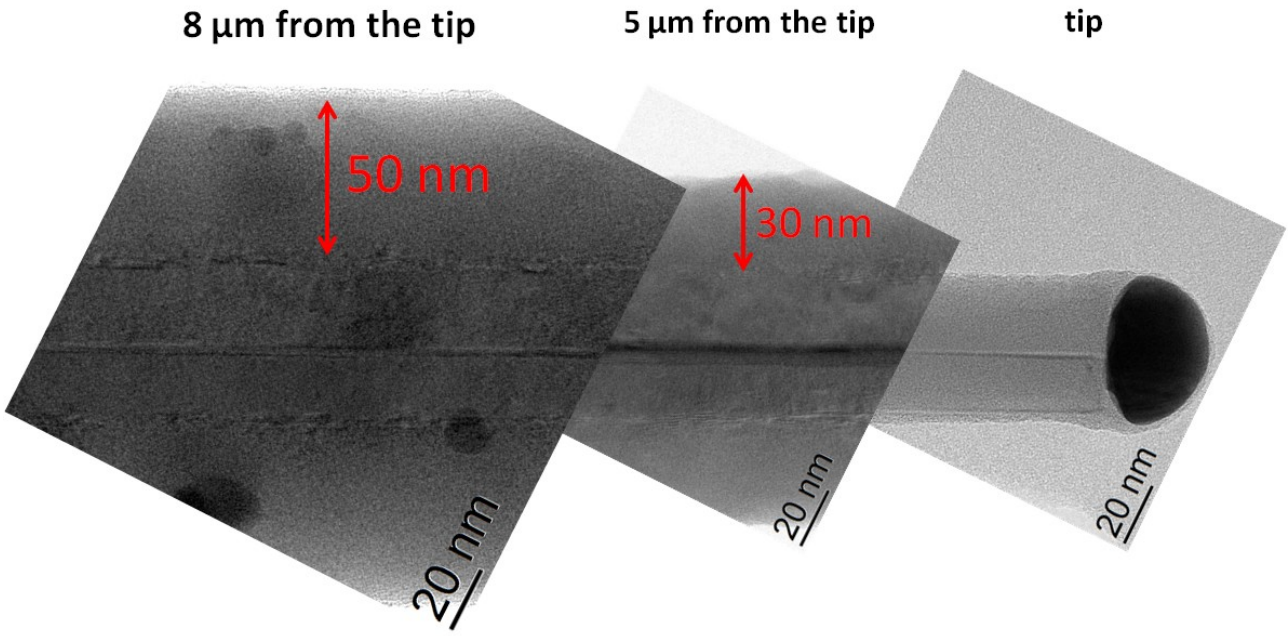

Figure 69: three TEM images are merged together to show the growth of the amorphous shell on the flawed wires.

The image is composed of three high magnification images of the same flawed wire, taken (from left to right) at 8 µm from the tip, at 5 µm from the tip and at the tip. In each image the thickness of the amorphous layer is reported. These images show that the crystalline core maintains, all along the wire, the same size it has at the tip, where no amorphous is observed. Also, the diameter of the core coincides with the size of the Au catalyst tip, the dark particle in the rightmost image. The change in diameter is caused by the lateral growth of an amorphous Si layer, that becomes thicker and thicker going closer to the wire base.
These observations are in agreement with a previous paper on the B doping of diamond Si. [93] Both the tapering and the formation of the flawed wires are related to the effect of B atoms on the Si. As a matter of fact, the interaction of the B with the free surface of Si [94] has been known

for decades: B tends to preferentially incorporate in the Si lattice sites just beneath the surface. It is reasonable to assume that it can induce the lateral growth (tapering) and, in certain circumstances not clear yet, it causes the formation of the thick amorphous shell observed in the flawed wire.

A last experiment has been performed to assess the chemical nature of the outer shell and correctly assign the 1.68eV peak observed in the CL spectra that can be attributed to the amorphous Si or to the SiO_x.

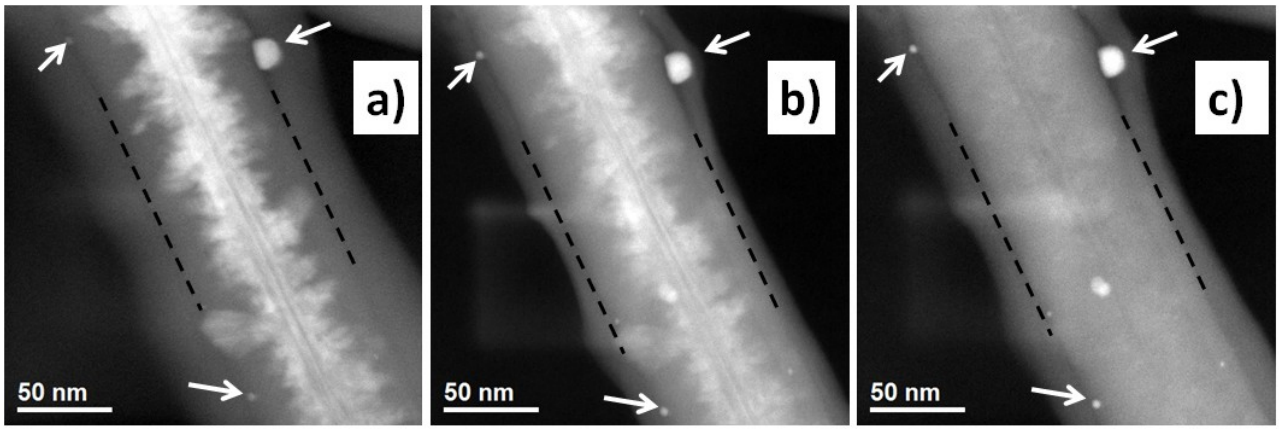

Figure 70: three STEM images recorded using different inner detection angle of the annular detector. The detection angles are: 34, 46 and 75 mrad for image **a), b)** and **c)** respectively.

In Figure 70 three STEM images are shown. The three images have been obtained with slightly different electro-optical configuration in order to change the inner detection angle of the annular detector. In the order the inner detection angle is: image a) 34 mrad, image b) 46 mrad and image c) 75 mrad.

As it has been mentioned in chapter 2.6 when the inner detection angle is too low it can collect electron that have been scattered by lattice distortions and defects. For this reason the NW core appear very bright in Figure 70 a). When the inner detection angle increases, these contributions are cut out and the core loses its brightness and eventually, when the inner angle is high enough to have a pure Z contrast image, no difference can be seen between the two regions composing the wire as in Figure 70 c). It follows that the shell and the core have the same chemical composition, therefore the shell is composed by amorphous Si and the CL peak at 1.68 eV is most likely due to the amorphous Si rather than SiO_x.

Also the population of the flawed NW has been observed to increase with the increasing diborane flow and the CL intensity of the 1.68 eV peak to increase accordingly.

The white arrows in three images indicate some Au nanoclusters residues of the growth. They act as a reference and demonstrate that the three images are obtained in the same region. The black dashed lines mark the wire sidewall. Everything is outside the lines is amorphous carbon deposited on the wire by the beam during the well known process called contamination. The contamination layer thickness increases with the exposition time to the electron beam and helps to guess the order in which the images have been taken.

CONCLUSIONS

The structural and chemical properties of Ge-Sb-Te and Si nanowires have been studied by means of Transmission Electron Microscopy techniques. A methodological research has been dedicated to the development of methods, based on the comparison of experimental images with their accurate simulations, to extract quantitative chemical information directly from the image contrast. In this respect, I gave my personal contribution to the development of the simulation program called STEM_CELL, writing the graphical interface used for the atomic models input.
The relevant results achieved during the thesis work are summarized as follows.

"***The effect of Ge-doping on the Sb_2Te_3 nanowires"*** The introduction of Ge in the Sb_2Te_3 compound changes its structural properties and turns it into the different GST compounds, characterized by specific electrical properties. Growing non stoichiometric materials, opens the way toward a fine tuning of the memory device properties.
The structural characterization allowed the optimization of the growth parameters in order to obtain pure Sb_2Te_3 and Ge doped SbTe defect free nanowires. The results also show that, changing the Ge precursor flow, the structure and the composition gradually change from pure Sb_2Te_3 NWs to stoichiometric $Ge_1Sb_2Te_4$ NWs passing through a mixed state having a disordered structure. The compositional range where the NWs can be grown without introducing major lattice defects has been defined, being a prerequisite for further studies on the electrical properties of the NWs.

"***Crystal structure assessment of Ge-Sb-Te phase change materials"*** Given the large number of atoms in the unit cell of the GST compounds, there is indetermination of the Ge and Sb atom positions, even though they have more profound effects on the optical and electronic properties. A method based on the comparison of HAADF-STEM images and proper simulations has been proposed and successfully used to determine the atomic arrangement of $Ge_1Sb_2Te_4$ and $Ge_2Sb_2Te_5$ compounds allowing, for the first time, the identification of the exact stacking sequence in GST NWs. The relevant finding is that only a structure with Ge and Sb atoms randomly sharing the same lattice sites is observed in opposition with the adverse predictions of all the theoretical models elaborated for the bulk material.

"***A new structure for Ge-doped Sb-Te nanowires*"** The Ge doped Sb_2Te_3 NWs, having diameter smaller than 40 nm, have been found to exhibit a new crystal phase never reported before in the literature. A full TEM characterization has been performed in order to refine their crystal structure using all the techniques subject of this work in a combined approach: HREM imaging, diffraction, HAADF-STEM imaging, and image simulations. Theoretical calculations confirmed that the new discovered polymorph, although unstable in bulk materials, can be grown in form of NW thanks to finite size effects.

"***Analysis of Si NWs exhibiting wurtzite crystal structure***" Cathodoluminescence studies revealed that the optical properties of our Si NWs are compatible with the presence of the wurtzite Si polymorph. Unfortunately, the existence of this phase is still a controversial topic in the literature.
A wrong identification of the wurtzite Si in TEM is ascribed to artifacts produced by defects in diamond Si. An accurate structural TEM characterization has been carried out and, thanks to image simulations, the major artifacts reported in the literature have been ruled out confirming the wurtzite character of the studied NWs.

"***Analysis of doped wurtzite Si NWs"*** Doping with selected electrically active impurities is of crucial importance to enable the control of the conductivity and the formation of p/n junctions, which are required for almost any electronic application. The study of wurtzite Si NWs is still in its infancy and until now no papers concerning the growth of doped wires have been published. A full characterization of wurtzite Si NWs doped with B and P, the two most common dopants, has been performed.

A different effect of the dopant species on the stability of the wurtzite phase has been demonstrated: B preserves the wurtzite phase, even if it causes an enhancement of the growth by-products, while P inhibits it. The by-products found on the B-doped samples have been identified as defective diamond Si NWs covered with a very thick amorphous shell.

Our results are in good agreement with optical measurements.

Appendix A: STEM_CELL

To quantitatively reproduce the contrast of the experimental images can be a very challenging task. The super cell (SC), namely the atomic coordinates set describing the specimen, must be perfectly tailored and many parameters must be accurately set in order to avoid artifacts that can lead to erroneous interpretation of the simulated images.

Also, the experimental images must be processed to directly extract physical properties (e.g. strain, composition) or to produce a clearer view of the image before matching them whit simulations, for example, by subtracting unwanted backgrounds, correcting for noise or drift, and removing artifacts.

Currently no software exists gathering all this functionalities together. STEM_CELL aims to simplify the whole process integrating a full cell-handling graphical interface and the simulation algorithm with the main analysis methods in a single tool. It also allows analyzing and graphically rendering the simulation results. In this appendix an overview on the main simulation features of the program and SC handling tools, as well as some examples, is given.

A snapshot of STEM_CELL main graphic windows is shown in Figure A1. The image shows that simulated images can be directly rendered and analyzed starting from this point. It is interesting here to appreciate the possibility to produce a full graphic rendering with tunable dynamics (even in color-scale) without spoiling the precision of the simulation.

All the simulation and analysis tools are readily accessible from the command bar.

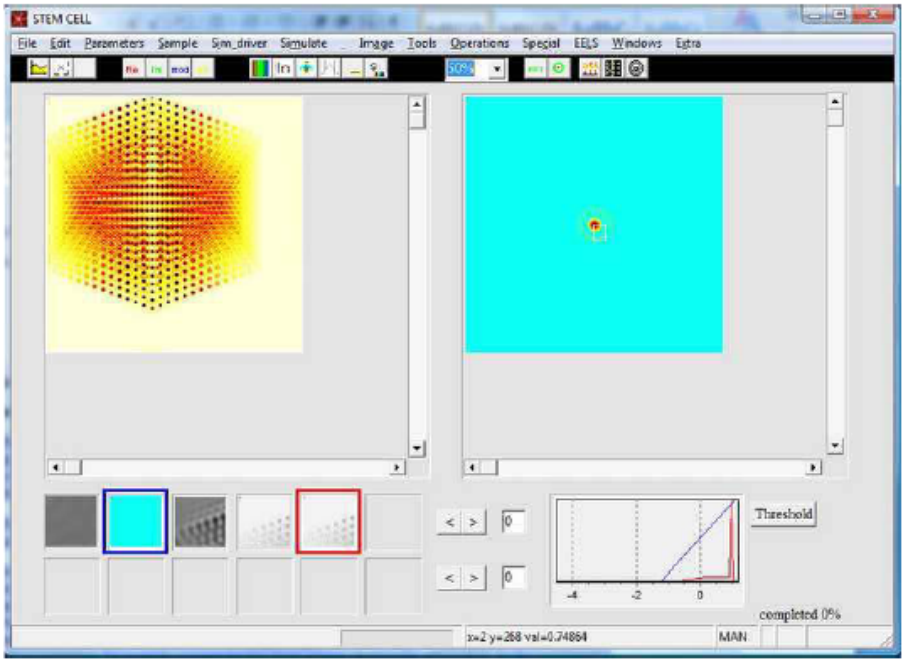

Figure A1: The main window of the STEM_CELL graphical interface.

The SCs creation and manipulation is the first step of a multislice simulation. In STEM_CELL this is accomplished by an internal class allowing for advanced operations. The native format for opening/saving SCs is the Kirkland one. A conventional extension *.krk* has been chosen for this kind of files. In addition other basic ASCII *xyz* formats are also allowed for SCs input/output operations. The program also allows direct creation of a crystal unit cell from space group and base atom coordinates in the common crystallographic format, using the devoted graphical interface shown in Figure .

Figure A2: graphical interface of the unit cell generation tool.

All the space group symmetries and most of the alternative settings can be used to create a unit cell starting from its symmetry operations. The software also speeds up the input procedure automatically setting the angle and the lattice parameters when the space group is selected. An additional internal format, with extension *.uce*, containing the crystallographic information has been introduced to store created unit cells.

A simple way to create a large SC is to replicate the input atomic positions of the unit cell according to the translation vectors of the unit cell. The coordinates are then transformed from the fractional (namely referred to unit cell dimension) coordinates to the Cartesian system through the transformation matrix m, that also define the translation vectors.

$$m = \begin{pmatrix} a & b\cdot\cos(\gamma) & c\cdot\cos(\beta) \\ 0 & b\cdot\sin(\gamma) & c\dfrac{\cos(\alpha)-\cos(\beta)\cos(\gamma)}{\sin(\gamma)} \\ 0 & 0 & c\dfrac{v}{\sin(\gamma)} \end{pmatrix} \tag{A.1}$$

Where a,b,c are the lattice parameters defining the unit cell direction and α,β,γ are the angles between the directions. The variable v is

$$v = \sqrt{1-\cos(\alpha)^2-\cos(\beta)^2-\cos(\gamma)^2+2\cos(\alpha)\cos(\beta)\cos(\gamma)} \tag{A.2}$$

Once a SC is created from the basic unit cell it is possible to modify and graphically render it in a separate window, called *slice_gen,* which is reported in Figure A3.

The graphical output is based on Kirkland's *sliceview* routine but graphical commands have been added for interactive change of visualization. The visualization commands permit changing atom radius, rotate the model, change perspective, exclude from visualization part of the atoms or select single atoms.

The modification commands, accessible from the right side of the window, allow complex cell operations like changing the slicing direction (by changing the axis orientation), operating distortions, shift, rotation or scaling operations, replicate or symmetrize the given cell, overlay different crystals (separately created) and select spherical, cylindrical or prismatic section of a unit cell. The selection can be used to remove the atoms inside or outside a region or to operate a restricted partial atom substitution.

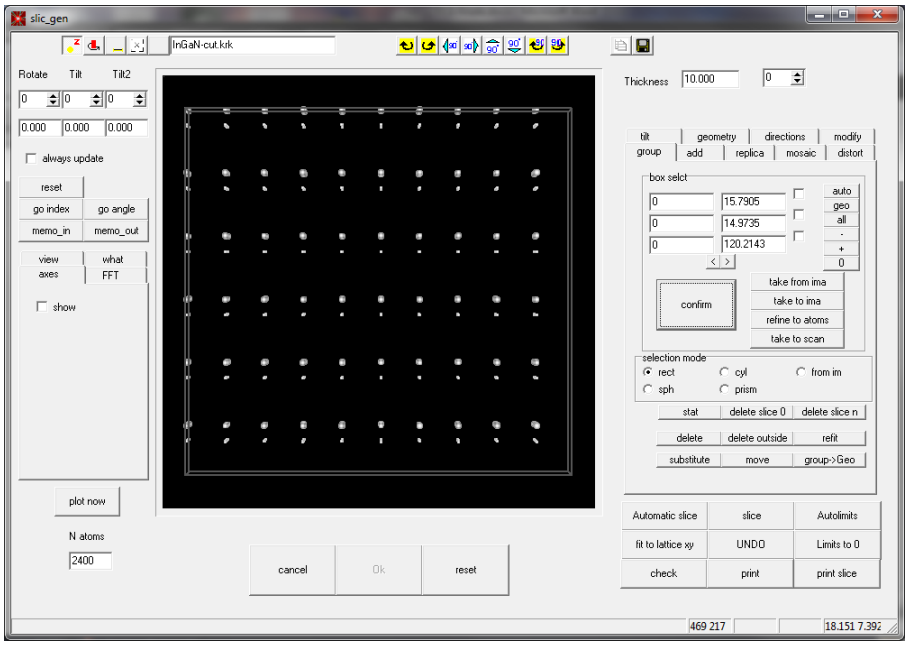

Figure A3: the *slic_gen* windows.

In principle, using the modification commands, any kind of specimen can be tailored to perfectly match the reality. A few example of complex specimen tailoring are reported in Figure a) and c) where a spherical and a multitwinned icosahedral nanopararticles, laying on an amorphous carbon film, are assembled.

When the SC is ready, the second step in the simulation chain is setting the optical parameters to match the experimental one. This procedure can be performed in the microscope condition window, see Figure A4. Here the optical parameters, like acceleration voltage, defocus, C_s, and the main aberrations can be inserted (left side of the window) to mimic the experimental conditions.

These parameters are intrinsically connected with the sampling parameters, i.e. the number of pixel in the final image. Using the wrong sampling might produce artifacts, information loss or, in the best case, a waste of memory and computation time.

One of the most important advantages of having a graphical interface for simulation is that simulation parameters can be easily set, changed and recalled for a different simulation. The set up of the optical/sampling parameters is simplified by the user interface that can be used to automatically set the typical conditions for each imaging mode.

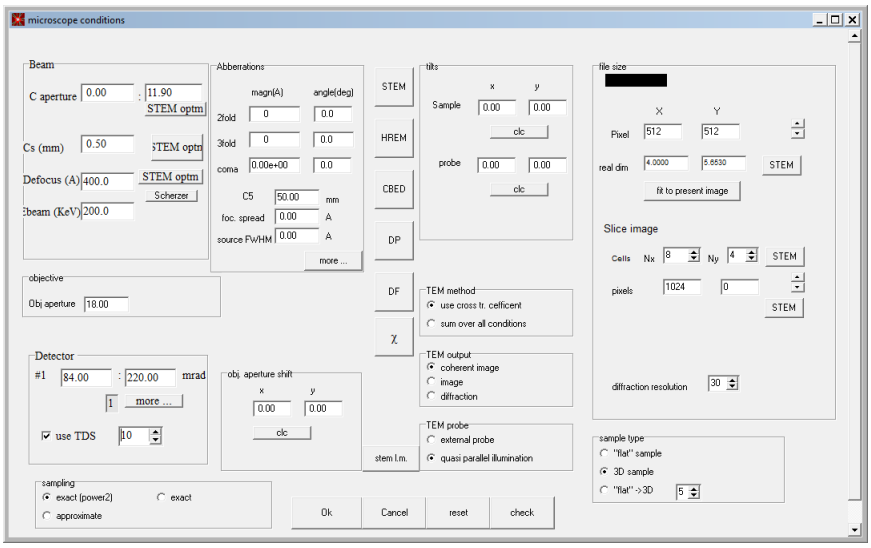

Figure A4: the microscope condition window.

The most important automatic setting regards the sampling conditions: once the SC and the optical parameters are selected the program calculates the optimal sampling for the given imaging mode. Defined modes are HRTEM, diffraction, two beam dark field, STEM, and a special mode to image the aberration function. The mode can be selected from the central colon in the panel and the calculated optimal parameters are reported in the right side.

The sampling conditions are those suggested by Kirkland who sets the minimal requirement in terms of sampling in the real and diffraction plane. In order to establish an automatic procedure ensuring a correct sampling the minimal requirements have been transformed in a closed formula for each mode.

When the SC is correctly set, the optical parameters are adjusted to match the experimental ones, and the correct sampling is imposed, the simulation can be run.

The simulations can require extremely long computing time, especially in the case of STEM calculations are performed pixel by pixel. However, it is also very easy to expand into a multiprocessor mode. The transmission of each probe position in the image can be put on a separate processor and the calculations run in parallel.

Using many physically separate computers allows a vast numbers (thousands) of processors to be coupled into one system called cluster.

In this context, a parallel code of STEM_CELL has been written using the standardized MPI message-passing system, and the specific routine is called *stemslic3_mpi.*

To conclude this appendix, Figure A5 shows some interesting simulation examples. In a) the atomic model of a Au nanoparticles deposited on an amorphous C film is reported. The simulated HRTEM

image is reported in b). The addition of noise on the simulation produces a very realistic image. The same amorphous film is used as substrate for the multiple twinned Ni nanoparticles in c) whose simulated image is reported in d). Noise has been added to the simulation in this case also.

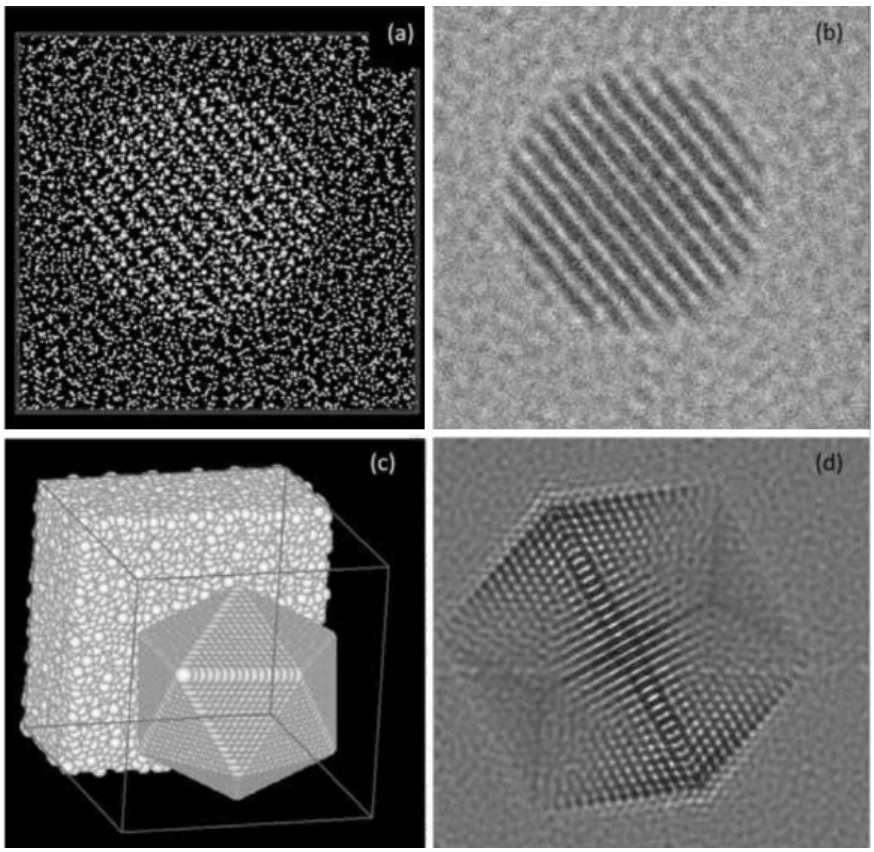

Figure A5: Simulated images of a spherical Au and an icosahedral Ni particle on amorphous carbon. **a)** and **b)** are the model and the HRTEM simulation for the Au sphere. **c)** and **d)** are the model and the HRTEM simulation for the icosahedral Ni particle.

BIBLIOGRAPHY

[1] P. Yang, "Wired for success," *Nature,* vol. 419, pp. 553-555, 2002.

[2] P. Yang, R. Yan and M. Fardy, "Semiconductor Nanowire: What's Next?," *Nanolett.,* vol. 10, pp. 1529-1536, 2010.

[3] P. Hirsch, A. Howie, R. Nicholson, D. Pashley and M. Whelan, Electron microscopy of thin crystal, Malabar, Florida: Krieger publishing company, 1977.

[4] L. Reimer, Transmission electron microscopy: physics of image formation and microanalysis, Berlin: Springer-Verlag, 1989.

[5] C. Carter and D. Williams, Transmission Electron Microscopy: a textbook, New York: Plenum Press, 1996.

[6] F. Bertein, "Un système correcteur en optique èlectronique," *C. R. Acad. Sci. Paris,* no. 225, pp. 801-803, 1947.

[7] J. Ramberg and E. Hillier, "The magnetic electron microscope objective: contour phenomena and the attainment of high resolving power.," *J. Appl. Phys,* vol. 18, pp. 48-71, 1947.

[8] O. Scherzer, "The Theoretical Resolution Limit of the Electron Microscope," *J. App. Phys.,* vol. 20, no. 1, pp. 20-29, 1948.

[9] O. Krivanek, N. Dellby and M. Murfitt, "Aberration correction in electron microscopy," in *Handbook of Charged Particle Optics*, Boca Raton, FL, CRC Press, 2008.

[10] D. V. Dyck, "High Resolution Electron Microscopy," in *International School on Electron Microscopy in Material Schience*, Mesagne, 1991.

[11] L. Lazzarini, L. Nasi and V. Grillo, "Trasmission Electron Microscopy techniques for," in *C. Lamberti: Characterization of Semiconductor Heterostructures and*, Elsevier, 2008.

[12] D. Jesson and S. Pennycook, "High-Resolution Z-contrast imaging of crystals," *Ultramicoscopy,* vol. 37, pp. 14-38, 1991.

[13] H. Bethe, "Theorie der Beugung von Elektronen an Kristallen," *Ann. Phys. Lpz.,* vol. 87, pp. 55-129, 1928.

[14] F. Fujimoto, "Periodicity of Crystal Structure Images in Electron Microscopy with Crystal Thickness," *Phys. stat. stol (a),* vol. 45, pp. 99-106, 1978.

[15] K. Kambe, "Visualization of Bloch Waves of High Energy Electrons in High Resolution Electron Microscopy," *Ultramicroscopy,* vol. 10, pp. 223-227, 1982.

[16] V. Grillo and E. Rotunno, "STEM_CELL: a software tool for electron microscopy. Part I Simulations," *Ultramicroscopy,* vol. 125, pp. 97-111, 2013.

[17] V. Grillo and F. Rossi, "STEM_CELL: A software tool for electron microscopy. Part 2 analysis of crystalline materials," *Ultramicroscopy,* vol. 125, pp. 112-129, 2013.

[18] E. Kirkland, Advanced Computing in Electron Microscopy, New York: Springer, 2010.

[19] D. Lencer, M. Salinga, B. Grabowski, T. Hickel, J. Neugebauer and M. Wutting, "A Map for Phase-Change Materials," *Nature Mater.,* vol. 7, pp. 972-978, 2008.

[20] N. Yamada, E. Ohno, N. Akahira, K. Nishiuchi, K. Nagata and M. Takao, "High Speed Overwritable Phase Change Optical Disk," *Jpn. J. Appl. Phys.,* vol. 26, no. Supplement 4, pp. 61-66, 1987.

[21] S. Ovshinsky, "Reversible Electrical Switching Phenomena in Disordered Structure," *Phys. Rev. Lett,* vol. 21, no. 20, pp. 1450-1453, 1968.

[22] X. Sun, B. Yu, G. Ng and M. Meyyappan, "One-Dimensional Phase-Change Nanostructure: Germanium Telluride Nanowire," *J. Phys. Chem. C,* vol. 111, no. 6, pp. 2421-2425, 2007.

[23] S.-H. Lee, Y. Jung and R. Agarwal, "Highly scalable non-volatile and ultra-low-power phase-change nanowire memory," *Nat. Nanotechnology,* vol. 2, pp. 626-630, 2007.

[24] R. Wagner and W. Ellis, "Vapor-Liquid-Solid Mechanism of Single Crystal," *Appl. Phys. Lett.,* vol. 4, no. 5, p. 89, 1964.

[25] M. Chen, K. Rubin and R. Barton, "Compound materials for reversible, phase-change optical data storage," *Appl. Phys. Lett.,* vol. 49, no. 9, pp. 502-504, 1986.

[26] Z. Zhang, J. Li and Q. Jiang, "Modelling for size-dependent and dimension dependent melting of nanocrystals," *J. Phys. D: Apll. Phys.,* vol. 33, no. 20, p. 2653, 2000.

[27] M. Longo, T. Stoycheva, R. Fallica, C. Wiemer, L. Lazzarini and E. Rotunno, "Au Catalyzed synthesis and characterization of phase change," *J. Cryst. Growth,* vol. 370, pp. 323-327, 2013.

[28] M. Longo, R. Fallica, C. Wiemer, O. Salicio, M. Fanciulli, E. Rotunno and L. Lazzarini, "Metal Organic Chemical Vapor Deposition of Phase Change Ge1Sb2Te4 nanowires," *Nano Lett.,* vol. 12, pp. 1509-1515, 2012.

[29] Y. J. Park, J. Y. Lee, M. S. Youm, Y. T. Kim and H. S. Lee, "Crystal structure and atomic arrangement of the metastable Ge2Sb2Te5 thin films deposited on SiO2/Si substrates by sputtering method," *J. Appl. Phys.,* vol. 97, p. 093506, 2005.

[30] T. Matsunaga, N. Yamada and Y. Kubota, "Structures of stable and metastable Ge2Sb2Te5, an intermetallic compound in GeTe±Sb2Te3 pseudo-binary system," *Acta Cryst. B,* vol. 60, pp. 685-691, 2004.

[31] E. Morales-Sanchez, E. Prokhorov, J. Gonzalez-Hernandez and A. Mendoza-Galvan, "Structural, electric and kinetic parameters of ternary alloys of GeSbTe," *Thin Solid Films,* vol. 471, pp. 243-247, 2005.

[32] T. Anderson and H. Krause, "Refinement of the Sb2Te3 and Sb2Te2Se structures and their relationship to nonstoichiometric Sb2Te3-ySey compounds," *Acta Cryst. B,* vol. 30, p. 1307, 1974.

[33] T. Matsunaga and N. Yamada, "Structural investigation of GeSb2Te4: A high-speed phase-change material," *Phys. Rev.B,* vol. 69, p. 104111, 2004.

[34] K. Agaev and A. Talybov, *Sov. Phys. Crystallogr.,* no. 11, p. 400, 1966.

[35] M. H. R. Lankhorst, "Modelling glass transition temperatures of chalcogenide glasses. Applied to phase-change optical recording materials," *J. Non-Crys. Sol.,* vol. 297, no. 2-3, pp. 210-219, 2002.

[36] Z. Wu, G. Zhang, Y. Park, S. D. Kang, H.-K. Lyeo, D. S. Jeong, J. Jeong, K. No and B. Cheong, "Controlled recrystallization for low-current RESET programming characteristics of phase-change memory with Ge-doped SbTe," *Appl. Phys. Lett.,* vol. 99, p. 143505, 2011.

[37] S. Kohara, K. Kato, S. Kimura, H. Tanaka, T. Usuki, K. Suzuya, H. Tanaka, Y. Moritomo, T. Matsunaga, N. Yamada, Y. Tanaka, H. Suematsu and M. Tanaka, "Structural basis for the fast phase change of Ge2Sb2Te5: Ring statistics analogy between the crystal and amorphous states," *Appl. Phys. Lett.,* vol. 89, p. 201910, 2006.

[38] S. Caravati, M. Bernasconi, T. Kuhne, M. Krack and M. Parrinello, "Coexistence of tetrahedral- and octahedral-like sites in amorphous phase change materials," *Appl. Phys. Lett.,* vol. 91, p. 171906, 2007.

[39] W. Welnic and M. Wuttig, "Reversible switching in phase-change materials," *Mater. Today,* vol. 11, no. 6, p. 20, 2008.

[40] M. Wuttig and N. Yamada, "Phase-change materials for rewriteable data storage," *Nat. Mater.,* vol. 6, no. 11, p. 824, 2007.

[41] G. Lee and S.-H. Jhi, "Ab initio studies of structural and electronic properties of the crystalline Ge2Sb2Te5," *Phys. Rev. B,* vol. 77, p. 153201, 2008.

[42] Z. Sun, S. Kyrsta, D. Music, R. Ahuja and J. M. Schneider, "Structure of the Ge–Sb–Te phase-change materials studied by theory and experiment," *Solid State Comm.,* vol. 143, no. 4, pp. 240-244, 2007.

[43] M. Schneider, M. Seibald and O. Oeckler, "A new series of long-range ordered metastable phases in the system M–Sb–Te (M = Ge, Ag)," *Dalton Trans.,* vol. 11, p. 2004, 2009.

[44] J. D. Silva, A. Walsh and H. Lee, "Insights into the structure of the stable and metastable (GeTe)m(Sb2Te3)n compounds," *Phys. Rev. B,* vol. 78, no. 22, p. 224111, 2006.

[45] E. Rotunno, L. Lazzarini, M. Longo and V. Grillo, "Crystal structure assessment of Ge–Sb–Te phase change nanowires," *Nanoscale,* vol. 5, p. 1557, 2013.

[46] A. Thust and K. Urban, "Quantitative high-speed matching of high-resolution electron microscopy images," *Ultramicroscopy,* vol. 45, pp. 23-42, 1992.

[47] I. Friedrich, V. Weidenhof, W. Njoroge, P. Franza and M. Wuttig, "Structural transformations of Ge2Sb2Te5 films studied by electrical resistance measurements," *J. Appl. Phys.,* vol. 87, p. 4130, 2000.

[48] I. Petrov and al., *Sov. Phys. Crystallogr.,* vol. 13, p. 339, 1968.

[49] B. Kooi and J. D. Hosson, "Electron diffraction and high-resolution transmission electron microscopy of the high temperature crystal structures of GexSb2Te3+x (x=1,2,3) phase change material," *J. Appl. Phys.,* vol. 92, no. 7, p. 3590, 2002.

[50] Z. Sun, J. Zhou and R. Ahuja, "Structure of Phase Change Materials for Data Storage," *Phys. Rev. Lett.,* vol. 96, p. 055507, 2006.

[51] G. Sosso, S. Caravati, C.Gatti, S. Assoni and M. Bernasconi, "Vibrational properties of hexagonal Ge2Sb2Te5 from first principles," *J. Phys: Condens. Matter,* vol. 21, no. 24, p. 245401, 2009.

[52] P. Caroff, J. Bolinsson and J. Johansson, *IEEE journal of selected topics in quantum electronics,* vol. 17, pp. 829-846, 2011.

[53] L. Lazzarini, G. Salviati, F. Fabbri, M. Zha, D. Calestani, A. Zappettini, T. Sekiguchi and B. Dierre, *ACS Nano,* vol. 3, pp. 3158-3164, 2009.

[54] Z. Ikonic, G. P. Srivastava and J. C. Inkson, "Electronic Properties of Twin Boundaries and Twinning Superlattices in Diamond-Type and Zinc-Blende-Type Semiconductors," *Phys. Rev. B,* vol. 48, p. 17181–17193, 1993.

[55] Z. Ikonic, G. P. Srivastava and J. C. Inkson, "Optical Properties of Twinning Superlattices in Diamond-Type and Zinc- Blende-Type Semiconductors.," *Phys. Rev. B,* vol. 52, p. 14078–14085, 1995.

[56] T. Burgess, S. Breuer, P. Caroff, J. Wong-Leung, Q. Gao, H. H. Tan and C. Jagadish, "Twinning Superlattice Formation in GaAs Nanowires," *ACS nano,* vol. 7, no. 9, p. 8105–8114, 2013.

[57] R. E. Algra, M. A. Verheijen, M. Borgstrom, L.-F. Feiner, G. Immink, W. P. v. Enckevort, E. Vlieg and E. P. A. M. Bakkers, "Twinning superlattices in indium phosphide nanowires," *Nat. Letters,* vol. 456, pp. 369 - 373, 2008.

[58] P. Caroff, K. A. Dick, J. Johansson, M. E. Messing, K. Deppert and L. Samuelson, "Controlled polytypic and twin-plane superlattices in III-V nanowires," *Nat. Nanothec.,* vol. 4, pp. 50 - 56, 2009.

[59] Q. Xiong, J. Wang and P. C. Eklund, "Coherent Twinning Phenomena: Towards Twinning Superlattices in III-V Semiconducting Nanowires," *Nano LEtt.,* vol. 6, no. 12, pp. 2736 - 2742, 2006.

[60] D.-H. Wang, D. Xu, Q. Wang, Y.-J. Hao, G.-Q. Jin, X.-Y. Guo and K. N. Tu, "Periodically twinned SiC nanowires," *Nanotechnology,* vol. 19, p. 215602, 2008.

[61] E. L. Wood and F. Sansoz, "Growth and properties of coherent twinning superlattice nanowires," *Nanoscale,* vol. 4, p. 5268, 2012.

[62] Y.-T. Zhai and X.-G. Gong, "Understanding periodically twinned structure in nano-wires," *Phys. Lett. A,* vol. 375, p. 1889–1892, 2011.

[63] P. Caroff, J. Bolinsson and J. Johansson, *IEEE J. Sel. Top. Quantum Electron.,* vol. 17, pp. 829-846, 2011.

[64] P. Giannozzi, S. Baroni, N. Bonini, M. Calandra, C. C. R. Car, D. Ceresoli, G. Chiarotti, M. Cococcioni, I. Dabo, A. D. Corso, S. d. Gironcoli, S. Fabris, G. Fratesi, R. Gebauer, U. Gerstmann, C. Gougoussis, A. Paolini, A. Pasquarello and e. al., "QUANTUM ESPRESSO: a modular and open-source software project for quantum simulations of materials," *J. Phys. Condens. Matter,* vol. 21, no. 39, p. 395502, 2009.

[65] R. Leitsmann and F. Bechstedt, "Surface influence on stability and structure of hexagon-shaped III-V semiconductor nanorods," *J. Appl. Phys.,* vol. 102, p. 063528 , 2007.

[66] T. Akiyama, K. Sano, K. Nakamura and T. Ito, "An Empirical Potential Approach to Wurtzite–Zinc-Blende Polytypism in Group III–V Semiconductor Nanowires," *Jpn. J. Appl. Phys,* vol. 45, pp. L275 - L278, 2006.

[67] G. Franzo, F. Priolo, S. Coffa, A. Polman and A. Carnera, "Room-temperature electroluminescence from Er-doped crystalline Si.," *Appl. Phys. Lett.,* vol. 64, pp. 2235-2237, 1994.

[68] V. V. Kveder, E. A. Steinman, S. A. Shevchenko and H. G. Grimmeiss, "Dislocation-related electroluminescence at room temperature in plastically deformed silicon.," *Phys. Rev. B,* vol. 51, pp. 10520-10526, 1995.

[69] D. Leong, M. Harry, K. J. Reeson and K. P. Homewood, "A silicon/iron-disilicide light-emitting diode operating at a wavelength of 1.5 um.," *Nature,* vol. 387, pp. 686-688, 1997.

[70] W. L. Wilson, P. F. Szajowski and L. E. Brus, "Quantum Confinement in Size-Selected, Surface-Oxidized Silicon Nanocrystals," *Science,* vol. 262, pp. 1242-1244, 1993.

[71] A. G. Nassiopoulos, S. Grigoropoulos and D. Papadimitriou, "Electroluminescent device based on silicon nanopillars.," *Applied Physics Letters,* vol. 69, pp. 2267-2269, 1996.

[72] A. G. Cullis and L. T. Canham, "Visible light emission due to quantum size effects in highly porous crystalline silicon.," *Nature,* vol. 353, pp. 335-338, 1991.

[73] M. M. Adachi, M. P. Anantram and K. S. Karim, "Optical Properties of Crystalline−Amorphous Core−Shell Silicon Nanowires," *Nano Lett.,* vol. 10, p. 4093−4098, 2010.

[74] M. Nolan, S. O'Callaghan, G. Fagas and J. C. Greer, "Silicon Nanowire Band Gap Modification," *Nano Lett.,* vol. 7, p. 34−38., 2007.

[75] L. Tsakalakos, J. Balch, J. Fronheiser, M.-Y. Shih, S. LeBoeuf, M. Pietrzykowski, P. J. Codella, B. A. Korevaar, O. Sulima, J. Rand, A. Davuluru and U. Rapol, "Strong broadband optical absorption in silicon nanowire films," *J. Nanophotonics,* vol. 1, p. 013552, 2007.

[76] V. Sivakov, G. Andrä, A. Gawlik, A. Berger, J. Plentz, F. Falk and S. H. Christiansen, "Silicon Nanowire-Based Solar Cells on Glass: Synthesis, Optical Properties, and Cell Parameters," *Nano Lett.,* vol. 9, p. 1549−1554, 2009.

[77] A. Fontcuberta i Morral, J. Arbiol, J. D. Prades, A. Cirera and J. R. Morante, "Synthesis of Silicon Nanowires with Wurtzite Crystalline Structure by Using Standard Chemical Vapor Deposition," *Adv. Mater.,* vol. 19, pp. 1347-1351, 2007.

[78] C. Raffy, J. Furthmüller and F. Bechstedt, "Properties of hexagonal polytypes of group-IV elements from first-principles calculations.," *Phys. Rev. B,* vol. 66, p. 075201, 2002.

[79] J. D. Joannopoulos and M. L. Cohen, "Electronic Properties of Complex Crystalline and Amorphous Phases of Ge and Si. Density of States and Band Structures.," *Phys. Rev.B,* vol. 7, pp. 2644-2657, 1973.

[80] N. Mermin and N. Ashcroft, Solid State Physics, New York: Holt, Rinehart and Winston, 1976.

[81] F. Fabbri, M. J. Smith, D. Recht, M. J. Aziz and G. Salviati, "Depth-resolved cathodoluminescence spectroscopy of silicon supersaturated with sulfur," *Appl. Phys. Lett.,* vol. 102, no. 3, p. 031909, 2013.

[82] G. C. Qin, H. Z. Song, B. R. Zhang, J. Lin, J. Duan and C. Q. Yao, "Experimental evidence for luminescence from silicon oxide layers in oxidized porous silicon," *Phys. Rev. B,* vol. 54, no. 4, pp. 2548-2555, 1996.

[83] S. Tong, X. Liu and X. Bao, "Study of photoluminescence in nanocrystalline silicon/amorphous silicon multilayers," *Appl. Phys. Lett.,* vol. 66, p. 469, 1995.

[84] H. Kohno, N. Ozaki, H. Yoshida, K. Tanaka and S. Takeda, "Misleading fringes in TEM images and diffraction patterns of Si nanocrystallites," *Cryst. Res. Technol.,* vol. 38, no. 12, pp. 1082-1087, 2003.

[85] C. Cayron, M. D. Hertog, L. L.-R. C. Mouchet, C. Secouard, J.-L. Rouviere and J.-P. Simonato, "Odd electron diffraction patterns in silicon nanowires and silicon thin films explained by microtwins and nanotwins.," *J. Appl. Cryst.,* Vols. 242-252, p. 42, 2009.

[86] B. Tian, P. Xie, T. Kempa, D. Bell and C. Lieber, "Single crystalline kinked semiconductor nanowire superstructures," *Nature Nanotechnol.,* vol. 4, pp. 824-829, 2009.

[87] B. Tian, X. Zheng, T. Kempa, Y. Fang, N. Yu, G. Y. J. Huang and C. Lieber, "Coaxial silicon nanowires as solar cells and nanoelectronic power sources," *Nature,* vol. 449, pp. 885-890, 2007.

[88] Y. Wu, Y. Cui, L. Huynh, C. Barrelet, D. Bell and C. Lieber, "Controlled Growth and Structures of Molecular-Scale Silicon Nanowires," *Nano Lett.,* vol. 4, pp. 433-436, 2004.

[89] A. Ourmazd, G. R. Anstis and P. B. Hirsch, "Dark-field electron microscopy of dissociated dislocations and surface steps in silicon using forbidden reflections," *Philos. Mag. A,* vol. 48, no. 1, pp. 139-153, 1983.

[90] J. M. Gibson, M. Y. Lanzerotti and V. Elser, "Plan-view transmission electron diffraction measurement of roughness at buried Si/SiO2 interfaces," *Appl. Phys. Lett.,* vol. 55, p. 1394, 1989.

[91] F. Fabbri, E. Rotunno, L. Lazzarini, D. Cavalcoli, A. Castaldini, N. Fukata, K. Sato, G. Salviati and A. Cavallini, "Preparing the Way for Doping Wurtzite Silicon Nanowires while Retaining the Phase," *Nano Lett.,* vol. 13, 2013.

[92] F. Fabbri, E. Rotunno, L. Lazzarini, N. Fukata and G. Salviati, "Visible and Infra-red Light Emission in Boron-Doped Wurtzite Silicon Nanowires," *Scientific reports,* 2013.

[93] L. Pan, K.-K. Lew, J. M. Redwing and E. C. Dickey, "Effect of diborane on the microstructure of bor-doped silicon nanowires," *J. Crys. Gro.,* vol. 277, pp. 428-436, 2005.

[94] P. Bedrossian, R. D. Meade, K. Mortensen, D. M. Chen, J. A. Golovchenko and D. Vanderbilt, "Surface Doping and Stabilization of Si (111) with Boron," *Phys. Rev. Lett.,* vol. 63, no. 12, pp. 1257-1263, 1989.

ACKNOWLEDGEMENTS:

The research activities on the GST NWs have been financed by:

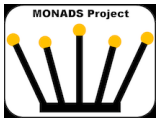

the "**MO**CVD growth and study of chalcogenide **NA**nowires for phase change **D**evice**S**" (MONADS) project, supported by Fondazione Cariplo.

and by

the "**SY**nthesis and functionality of chalcogenide **NA**nostructures for **P**ha**SE** change memories" (SYNAPSE) project, supported by the European union in the Seventh Framework Programme.

The research activities on the Si NWs have been partly supported by:
the Italian-Japanese Progetto di Grande Rilevanza "**N**anoscale ass**E**ss**M**ent of ch**E**mical and phy**S**ical propert**I**es of advanced nano**S**tructures" (NEMESIS) funded by the Italian Ministry of Foreign Affairs.

I would like to thank the **I**nstitute of **M**aterials for **E**lectronics and **M**agnetism of the National Research Council IMEM-CNR, where all my work was carried out, for hosting my PhD.

The computational activities have been partly supported by:
the Italian 2009 PRIN project "Sintesi, caratterizzazione e funzionalizzazione di nanotubi di carbonio per applicazioni fotovoltaiche" by the Italian Ministry of Education (MIUR).

Thanks are due to all the people who collaborated to the realization of this work (in order of appearance):

Dr. **Massimo Longo** (Laboratorio MDM, IMM-CNR, Italy) for growing and providing the GST NWs and for the very useful discussion on all the GST-related topics.

Dr. **Roberto Fallica** (Laboratorio MDM, IMM-CNR, Italy) for the electrical measurements on the GST NWs.

Prof. **Marco Bernasconi** and Dr. **Davide Campi** (Università Milano Bicocca, Italy) for the DFT calculation on the Sb_2Te_3 metastable phase.

Dr. **Naoki Fukata** (NIMS, Japan) for growing and providing the Si NWs.

Dr. **Filippo Fabbri** (IMEM) for the cathodoluminescence measurements on the Si NWs.

A special thank goes to Dr. **Vincenzo Grillo**, father of STEM_CELL, for introducing me to the computer simulation world and for teaching me countless tips and tricks about electron microscopy.

……e tanti tantissimi grazie a tutta la commessa SCALING-*e-dintorni* per tutto l'aiuto, i consigli, gli incoraggiamenti nei momenti difficili e le "chiacchiere da corridoio".

Un doveroso ringraziamento va ai miei genitori e a tutta la mia famiglia senza la quale al dottorato non sarei arrivato.

Grazie Filippo per esser stato un collega, un coinquilino e un amico negli ultimi tre anni, sia qui che oltreoceano.
Grazie a Nylon (non il polimero!) amico affidabile ormai da sempre.
Un grazie di cuore per avermi fatto compagnia lungo tutti questi ultimi 3 anni a Pelli, Dabram, Gino e le ragazze di Borgo Guasti, Anto, Angie, Flora e Roby, grazie ai quali, al dottorato, non sarei dovuto nemmeno arrivare!!